Motion and deformation of capsules flowing in microfluidic channels

Xu-Qu Hu

Par **Xu-Qu HU**

Mouvement et déformation de capsules circulant dans des canaux microfluidiques

Thèse présentée
pour l'obtention du grade
de Docteur de l'UTC

flow direction →

THÈSE

Présentée par

Xu-Qu HU

Pour l'obtention du grade de

Docteur de l'Université de Technologie de Compiègne
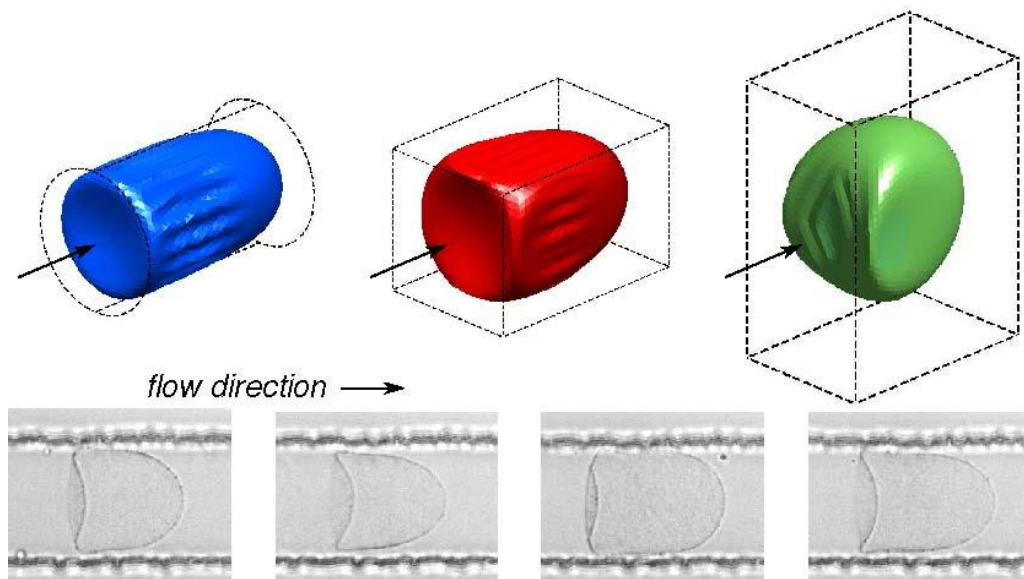
Champ disciplinaire: Bio-ingénierie, biomécanique, biomatériaux

Mouvement et déformation de capsules circulant dans des canaux microfluidiques

flow direction →
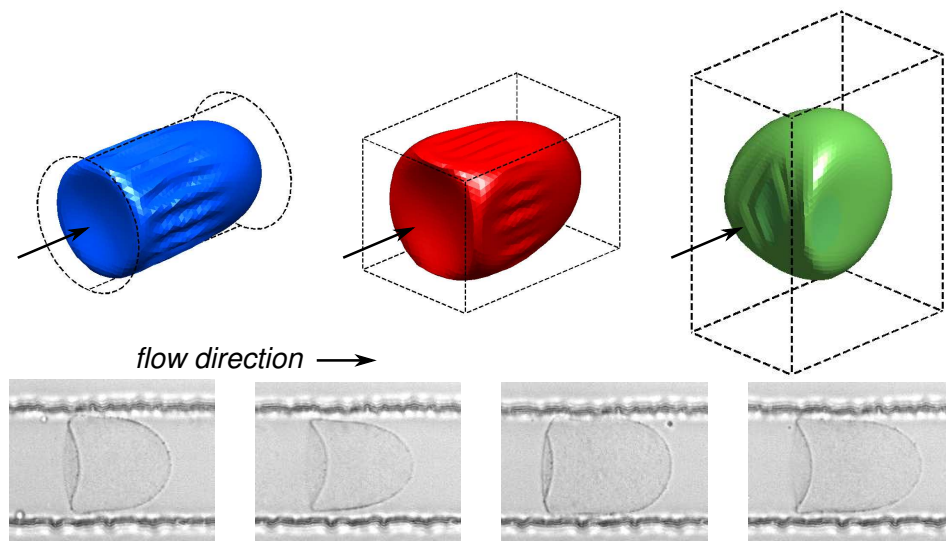
Soutenue le 29 Mars 2013

Mouvement et déformation de capsules circulant dans des canaux microfluidiques

Motion and deformation of capsules flowing in microfluidic channels

Soutenue le 29 Mars 2013 devant le jury composé de:

M.	SELLIER Antoine (président)
M.	BENLAHSEN Mohammed (rapporteur)
M.	LÉONETTI Marc (rapporteur)
Mme.	BARTHÈS-BIESEL Dominique (directrice)
Mme.	SALSAC Anne-Virginie (directrice)
M.	VILLON Pierre

Cette thèse est dédiée à
mes parents
et à toute ma famille
pour leur immense amour et soutien durant toute ma vie

谨以此文
献给我的父母
和所有亲人
感谢他们无止境的关爱和支持

This thesis is dedicated to
my parents
and to all my family
for their endless love and support throughout my life

Acknowledgements

I would never have been able to finish my dissertation without the guidance of my advisors, help from the committee members, encouragement from friends and support from my family.

I would like to firstly express my deepest gratitude to my advisors, Prof. Dominique Barthès-Biesel and Dr. Anne-Virginie Salsac, for their excellent guidance, patience, caring and support throughout my life in France. I am sure it would not have been possible without their help.

Besides my advisors, I would also like to thank the rest of my committee members, Prof. Antoine Sellier, Prof. Mohammed Benlahsen, Dr. Marc Léonetti and Prof. Pierre Villon for their encouragement, insightful comments and friendly suggestions.

I must thank all the members of our excellent laboratory, CNRS UMR 7338, including the faculties, staff members and students. My sincere thanks also goes to my friendly colleagues in our research group, Johann, Peiyuan, Cristi, Xuan, Liguo, Iolanda, Claire, Benjamin, Pierre-Yves, Fabien. The enlightening discussions, enthusiasm for research and friendship have made my stay in Compiègne enjoyable and pleasant.

A special thanks also goes to Xuan Zhang and all my friends for being with me during these memorable years in France.

In particular, I am deeply grateful to Prof. Kairong Qin for giving me the first taste of research. I would like to extend my sincerest thanks and appreciation to Prof. Yuehong Qian for his continued help and support. Gratitude is also extended to Prof. Zhiming Lu, Prof. Yulu Liu, Prof. Xiang Qiu and Dr. Yongxiang Huang for the encouragement they have always provided.

Last but not the least, I would also like to thank my parents, grandfather, uncle, aunt and lovely cousin. They are always supporting me and encouraging me with their best wishes.

Abstract

The capsule is a liquid droplet enclosed by a very thin and deformable membrane. The membrane allows the separation and protection of internal liquid medium from external environment. The membrane mechanical properties are critical for the deformation and motion of capsules in actual applications. The flow of a capsule suspension through a microfluidic channel with dimensions comparable with those of the suspended particles can be used to infer the elastic properties of the capsule membrane, however a mechanical model of the process is then essential.

We present a three-dimensional numerical model for this fluid-structure interactions problem in confined flows. We use a novel numerical model that couples a boundary integral method for the internal and external fluid flows and a finite element method for the membrane deformation. This model is proved to be stable even when the membrane is under compression and tends to buckle.

The developed model is applied to study the flow of an initially spherical capsule in channels with different cross-sections. In a cylindrical channel with a circular cross-section, we show that the confinement effect of the channel walls leads to compression of the capsule in the hoop direction. The membrane then tends to buckle and to fold as observed experimentally. The capsule deformation is three-dimensional but can be fairly well approximated by an axisymmetric model that ignores the folds. In a microfluidic channel with a square cross-section, the fully three-dimensional capsule deformation is less than the one in a cylindrical channel for the same given flow conditions. The effects of membrane constitutive laws, size ratio and flow strength on the capsule deformation are systematically studied. We provide the databases of the deformation parameters and capsule velocity as a function of flow strength, size ratio and membrane constitutive laws in a square section channel. The comparison between experimental and numerical results allows us to deduce the membrane

1

mechanical properties of a population of artificial capsules with an oval-bumin membrane. We also show that the ovalbumin membrane tends to have a strain-softening behavior.

The present work shows the possibility to measure the membrane mechanical properties by using a microfluidic channel with a square cross-section. It can be extended to unsteady capsule flows in a channel with variable cross-sections or bifurcations.

keywords: microcapsule, fluid-structure interactions, boundary integral methods, microfluidics, inverse analysis

Résumé

Une capsule est une goutte de liquide enveloppée par une membrane très fine et déformable. La membrane permet de séparer et protéger le milieu interne du milieu externe. Les propriétés mécaniques de la membrane sont essentielles pour le mouvement et la déformation de la capsule dans les applications pratiques. L'analyse de l'écoulement d'une suspension de capsules dans un canal microfluidique de dimension comparable est une technique qui peut être utilisée pour déterminer les propriétés élastiques de la membrane. Cependant, un modèle mécanique approprié de l'écoulement est essentiel.

Nous présentons un modèle numérique tridimensionnel pour ce problème d'interaction fluide-structure dans un écoulement confiné. Ce modèle couple une méthode intégrale de frontière pour les écoulements des fluides interne et externe et une méthode d'éléments finis pour la déformation de la membrane. Il s'avère être stable même lorsque la membrane est en compression et a tendance à flamber.

Le modèle proposé est utilisé pour étudier l'écoulement d'une capsule initialement sphérique dans des canaux de sections transversales différentes. Dans un canal cylindrique, on montre que l'effet de confinement des parois du canal conduit à la compression de la capsule. Cela engendre la formation de plis sur la membrane autour de l'axe de l'écoulement, phénomène

également observé expérimentalement. La déformation de la capsule est donc tridimensionnelle, mais peut être correctement approximée par un modèle axisymétrique qui ne tient pas compte des plis. Dans un canal microfluidique de section carrée, la déformation est totalement tridimensionnelle, et moins importante que dans un canal cylindrique pour des conditions d'écoulement identiques. Les effets de la loi constitutive de la membrane, du rapport de taille et du débit d'écoulement sur la déformation de la capsule sont systématiquement étudiés. Nous avons construit une base de données des paramètres de la déformation et de la vitesse de la capsule en fonction du débit d'écoulement, du rapport de taille et de la loi constitutive de la membrane dans un canal carré. La comparaison entre les résultats expérimentaux et numériques nous permet de déduire les propriétés mécaniques de la membrane en ovalbumine d'une population de capsules artificielles. Nous avons ainsi montré que la membrane en ovalbumine semble avoir un comportement adoucissant.

Ce travail prouve la faisabilité de la mesure de propriétés mécaniques d'une membrane en utilisant une technique microfluidique en canal carré. Il pourrait être étendu par l'étude d'écoulements instationnaires dans un canal de section variable ou avec une ou plusieurs bifurcations.

mots-clés: microcapsule, interaction fluide-structure, méthode des intégrales de frontière, microfluidique, analyse inverse

Contents

List of Figures

iii

Chapter 1

Introduction

1.1 Definition and applications of capsule

Capsules consisting of an internal liquid droplet enclosed by a thin elastic membrane exist in every corners of our daily lives, just as the omnipresent biological cells in nature and widespread deformable artificial particles in industry. Thanks to the presence of a thin membrane, the specific structure of capsules allows the separation and protection of an internal medium from an external liquid environment. Therefore the dispersion and degradation of the internal active substance are prevented or controlled by the membrane. Meanwhile, the motion and deformation of a capsule are usually different from that of a rigid particle, as they largely depend on the mechanical properties of membrane.
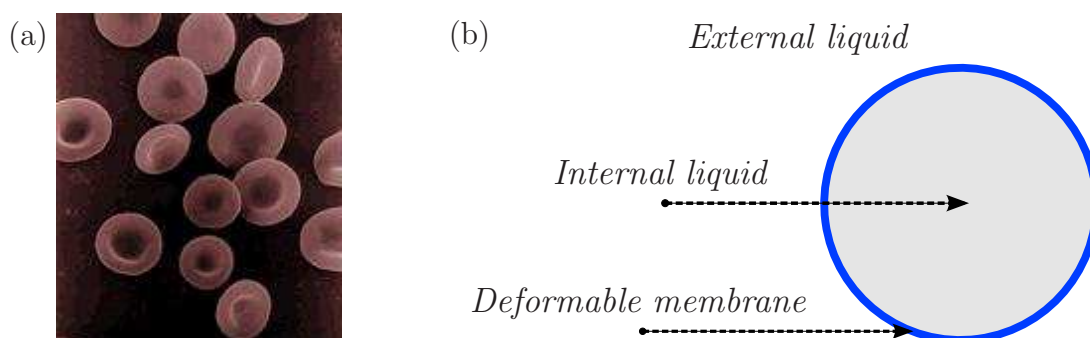
Figure 1.1: Capsule model for biological cells. (a) red blood cells (from *clinicalcenter.nih.gov*); (b) Capsule model.

A capsule is usually used as a simplified model for those biological cells ranging from red blood cells to bacteria. They differ from simple droplets, for which an extensible interface controlled by surface tension separates the drop liquid from the external liquid. Biological capsules are usually enclosed by a surface inextensible thin solid

membrane with complicated structure. For instance, the red blood cell, which can be treated as a typical passive natural capsule, is enclosed by a membrane consisting of a phospholipid bilayer containing internal membrane proteins and an underlying membrane skeleton [101]. As the red blood cells are responsible for transportation of respiratory gases to and from the tissues, large motions and deformations of red blood cells will be repeated for a large number of cycles in the circulation system during their life cycle spreading over 120 days [38]. The membrane mechanical properties permit the protection of internal hemoglobin from external plasma flow by avoiding rupture, as well as the maintenance of a relatively stable shape in the microcirculation which is beneficial for the gaseous exchanges. In addition, the high deformability of the membrane plays a key role in the microcirculation by allowing the red blood cell to flow easily through capillary vessels of diameter smaller than the cell dimension. There is no question that the membrane mechanical properties are essential for the red blood cell to realize its natural functions.
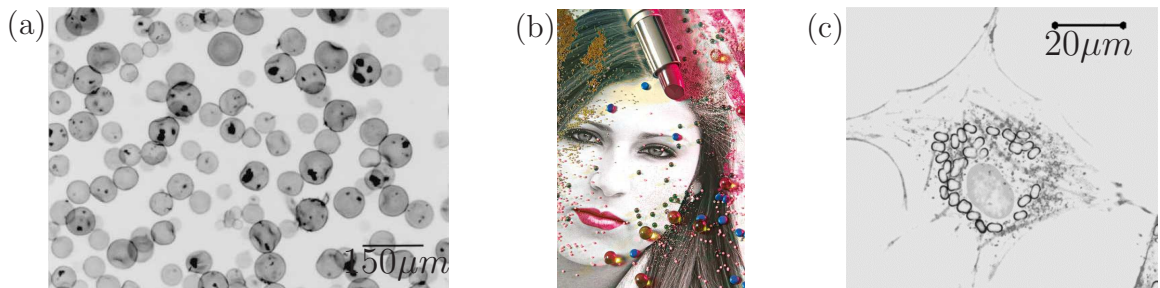
Figure 1.2: Applications of encapsulation techniques in various domains. (a) capsules for drug release in pharmaceutics [71]; (b) capsules in cosmetics (from www.swri.org); (c) cellular uptake by microcapsules in bioengineering [109].

To make artificial capsules, a controlled encapsulation technique encloses the internal substance (liquid or solid) by a thin elastic membrane. It leads to encapsulated structures which are of great importance to meet the demands of industries for many reasons. One of the primary reasons is that the isolation of the internal active substance can provide effective protection by avoiding its degradation and deactivation (like oxidation effect) by the surrounding environment. Besides, encapsulation techniques also permit the targeted transportation and/or the controlled release of the internal substance as demanded in practical applications. During the past few decades, lots of researchers have paid close attention to the studies of encapsulation techniques [110].

Artificial capsules are widely used in many industrial domains, such as in pharmaceutics, cosmetics, bio- and biomedical engineering, as shown in Fig. 1.2.

In the pharmaceutical industry, the targeted transportation of an active thera-peutic drug over an extended time is becoming more common for medical treatments, since it has lots of benefits such as the decrease of drug toxicity and the increase of use efficiency. For this purpose, encapsulation techniques are often used to develop controlled-release delivery systems, which usually involve colloidal packagings such as polymeric particles and microemulsion capsules [13]. The use of encapsulation tech-niques is also found to be able to improve the dissolution and bioavailability of some medicines. Ghirardi et al. [33] have compared the encapsulated form of the digoxin solution inside soft gelation capsules with the common commercial tablet form, the *in vitro* results showed that the digoxin capsules dissolved more readily with higher bioavailability than that in tablet forms.

Microcapsules are also used as a carrier system for active materials (such as ther-apeutic antigen and liquid reagents) in applications of drug targetting and/or slow release systems. The protection of the internal medium is allowed by encapsulation during transportation, and controlled release can be realized by the break-up of the microcapsules when they arrive at the targeted area. Such applications widely exist in the bioengineering and biomedical domains [39, 70].

In the cosmetic industry, the encapsulation technique is also widely used to meet the increasing number of demands for the better control of labile substances such as antioxidants and perfumes. The encapsulation of an active component can facilitate its fabrication, storage and release. A good example is the preservation of vitamin E in cosmetics. As is known to all, the vitamin E can be used in skin care products to protect the tissue from the effect of ultraviolet radiation. However, it is easy to degrade through exposure to air and/or heat. Encapsulation is one technique used to preserve its activity. For example, Shalaka et al. [93] developed a method based on a membrane consisting of the combination of two polymers (pectin and sodium alginate). During application, the protected vitamin E is released by rupturing the capsules. Hurteaux et al. [45] have proposed an adapted transacylation method to enclose calcium alginate gel by a human serum albumin (HSA)-alginate membrane. The obtained capsules of size around 60 μm were shown to be effective for the slow release of the internal substance. Great progress has also been done on encapsulation techniques for other cosmetic products such as essential oils and ultraviolet absorbents [66, 3, 67].

In the food industry, there is an increasing number of food products containing bioactive components with a health promoting or disease preventing effect [18]. Some live microorganisms such as probiotic bacteria and lactobacilli can be used as bioactive

food components, but they are highly sensitive to the environmental conditions (e.g. pH value, hydrodynamic force and digestive enzymes in the digestive system) [68]. An important application of the encapsulation technique is to improve the stability of those live and active ingredients in complex conditions. An emulsion method was proposed to encapsulate lactobacilli in calcium alginate gels by Shue and Marshall [95]. They showed that encapsulated lactobacilli had survival rate 40% higher than free non-entrapped cells during freezing of ice milk. Sultana et al. [100] have proposed a modified method for probiotic cells involving calcium-alginate-starch encapsulation. The encapsulated cells were shown to have a better survival rate than free cells after a storage period of 8 weeks. Many other benefits can also be introduced into food industry by the encapsulation technique, for example, to conceal unpleasant tastes of polyphenols [28] and to preserve the flavor of aromatic additives [65]. More reviews of the encapsulation technique in food industry are available in [18, 28, 68].

In this dissertation, we specifically study liquid-filled capsules enclosed by a thin elastic membrane, for which, the motion highly depends on mechanical properties of the deformable membrane. A good understanding of the membrane mechanical properties is therefore critical for lots of purposes, ranging from the design of artificial capsules to the control of rupture as demanded.

1.2 Fabrication of liquid-filled capsule

Since capsules have extensive applications in various domains, many researchers have paid close attention to their fabrication, and several encapsulation techniques have been developed. Capsules of different physical properties (e.g. the shape, size and stability) can be produced depending on fabrication parameters, membrane materials and encapsulation techniques. Tremendous research efforts have been done on different aspects of the capsule fabrication. In this section, we briefly summarize some classical techniques that are close to the purpose of this dissertation.

The traditional methods for capsule fabrication can be decomposed into two steps [16]: first, a liquid droplet of required size is fabricated. Then, capsules are formed by enveloping the droplet with a membrane made of different materials (e.g. proteins and polymers).

1.2.1 Droplet fabrication

For the fabrications of droplets, one of the most common and classical methods is to use the emulsification process which consists in agitating mechanically two immiscible
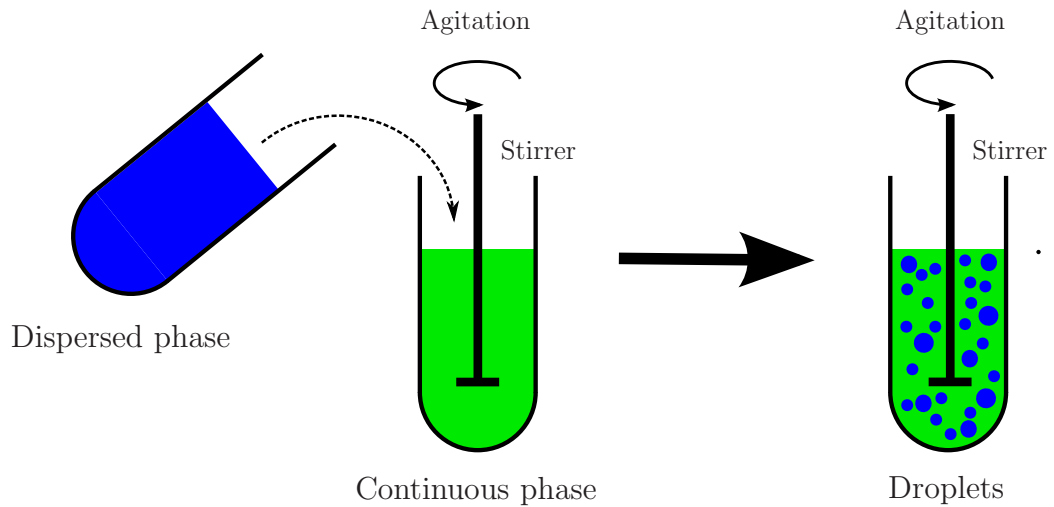
Figure 1.3: Fabrication of droplets from the emulsification process produced by the mechanical agitation.

phases, e.g. the oil and water, as shown in Fig. 1.3. Droplets are thus generated from the emulsification effect. The average size of fabricated droplets depends on several factors, including the agitation velocity, the emulsification time, the ratios of volumes and viscosities between dispersed and continuous phases, etc. The emulsification process can also be produced by some other systems such as power ultrasound. Abïsmail et al. [1, 2] have compared the oil-in-water emulsions produced by mechanical agitation or power ultrasound. They showed that the power ultrasound method leads to a smaller average drop size than mechanical agitation under the same conditions. Although a large number of droplets are produced by the emulsification processes, a limitation of this technique is the inhomogeneity of droplet sizes which can lead to a large dispersion to about 40% [16].

Another classical droplet fabrication is the extrusion method. As implied by the name, the dispersed phase (e.g. alginate solution) is extruded through an orifice or syringe needle under a controlled pressure, the droplets are thus formed one by one by the effect of surface tension [73, 50]. The size of the fabricated droplets is more homogeneous than in the emulsification process. It depends largely on the pore geometry and some other factors such as the applied pressure [73]. However, the droplets are extruded individually. This method only allows the fabrication of a limited number of droplets, which is one of the drawbacks of this technique [16].

1.2.2 Membrane formation

Liquid-filled microcapsule membranes are mainly fabricated by a chemical process, such as interfacial polycondensation and interfacial cross-linking polymerization.
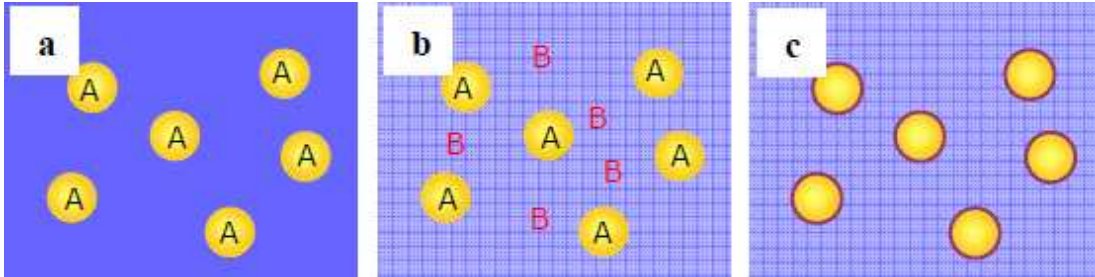
Figure 1.4: Typical process of membrane formation by the interfacial polycondensation of dispersed monomers. Image from [102].

A typical process of the membrane generation by the interfacial polycondensation of dispersed monomers is shown in Fig. 1.5. Considering two monomers (A and B) which can react with each other according to a polycondensation mechanism, it is possible to introduce monomers A in the dispersed phase and then generate the droplets containing monomers A by the emulsification process, as shown in Fig. 1.5(a). Adding the monomers B in the continuous phase, the monomers react together to induce an interfacial polycondensation, as shown in Fig. 1.5 (b). The reaction between the monomers is decreased since the initial membrane formation, as it becomes harder for the monomers to diffuse through the increasingly thicker membrane [60]. The properties of the formed membranes are normally homogenous. The size of fabricated microcapsules depends largely on the factors in the emulsification process, as presented in section 1.2.1. Several studies have been done with this technique for the formation of microcapsules using nylon [86], polyurethanes [46] or polymers [10].
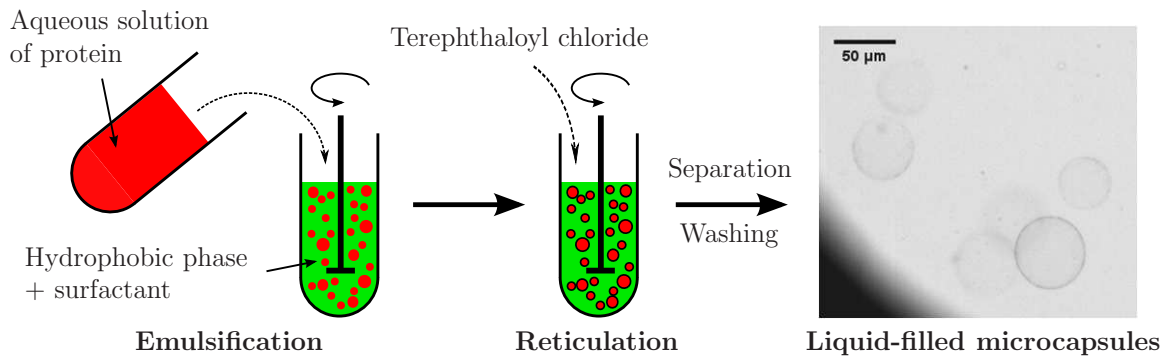
Figure 1.5: Typical process of microcapsule fabrication by the interfacial polymerization with reticulation reactions.

6

The liquid-filled microcapsules are also often fabricated by interfacial polymerization with cross-linking reactions [25, 17]. The principle process of this method is shown in Fig. 1.5. First, an aqueous solution of protein is emulsified in a hydrophobic phase to form the droplets of required size with the use of a surfactant as the stabilizer. An organic solution of the cross-linking agent (e.g. terephthaloyl chloride) is then added into the emulsified solution. Since the cross-linking agent is bifunctional, the acylating reagent creates covalent bonds and leads to the formation of bridges between protein molecules: the membrane is thus formed by reticulation at the interface of the droplet. Finally, the reaction is stopped by dilution. The fabricated microcapsules are separated from the hydrophobic phase by centrifugation and washing, and conserved in an aqueous suspension. This method can be used to produce capsules of sizes ranging from several microns to millimeters [111, 102, 16]. The properties of fabricated capsules depend on the parameters of emulsification process (e.g. the agitation velocity), and also on several other factors, such as the pH of the aqueous solution, the concentration in protein and the reticulation time. Chu et al. [17] have studied the elastic modulus of the membrane of ovalbumin microcapsules by an inverse analysis method and showed that the shear modulus increases with the pH values and reaction time.

1.3 Determination of capsule membrane mechanical properties

The determination of the membrane mechanical properties is essential both for fundamental research and for industrial applications, but it is a challenging task because of the small size of micro-capsules. This problem has attracted much attention in the past few decades, and several methods have been proposed to measure the mechanical properties of different capsules. The common idea is to generate a capsule deformation under a controlled stress and then to compare with the results of the corresponding mechanical models to infer the mechanical properties of the capsule membrane.

1.3.1 Technique of compression

A widely used method for relatively large millimeter-size capsules is to compress them between two solid parallel plates [12, 81, 84, 98]. As shown in Fig. 1.6, an initially spherical capsule with radius r_0 is placed between two parallel plates without contact at the beginning of experiment. The separation of the two plates $d(t)$ is used to measure the capsule deformation. It is recorded simultaneously with the resultant

force on the capsule $F(t)$ in the process of compression. The compression process is usually applied until the capsule bursts. A mechanical model is subsequently used to analyze the experimental results: for each intra-plate distance, the comparison of the experimental force and the numerical/theoretical one allows the deduction of the intrinsic mechanical properties of the capsule membrane.
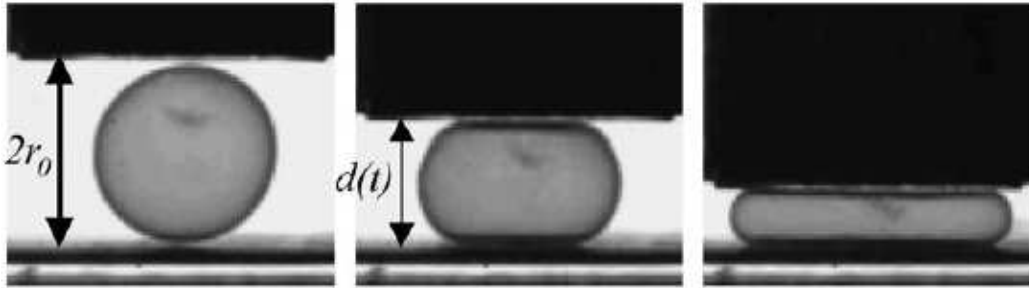
Figure 1.6: Compression of an initially spherical capsule between two parallel plates [81].

A proper mechanical model of the capsule compression is therefore critical for the successful deduction of the membrane properties from experimental results. Rachik et al. [81] have shown that a 2D model with a thin shell approximation can be used for the compression of capsules with thin membranes (less than 5% of total radius), but it is necessary to use a 3D model for thicker membranes as the shear stress distribution in the membrane thickness needs to be taken into account.

Carin et al. [12] have performed compression experiments on biocompatible capsules with HSA-Alginate membrane, and determined the values of the apparent membrane elastic modulus as the deformation increases. The compression experiments on HSA-Alginate capsules with different membrane thickness have also been presented to show the effect of membrane thickness [81]. Smith et al. [98] have applied the compression test on yeast cells to measure the wall material properties.

Although the compression technique has been implemented successfully to measure several types of capsules, it was found that it requires a high sensitivity of the experimental setup to allow precise measurement of the force for small compression [12], and its applications are limited to millimeter-size capsules.

1.3.2 Technique of atomic force microscope

Following the successful invention of the scanning tunneling microscope which can image individual surface atoms with unprecedented resolution, some new "scanning probe" microscopes relying on the mechanical scanning of a sharp tip over a sample
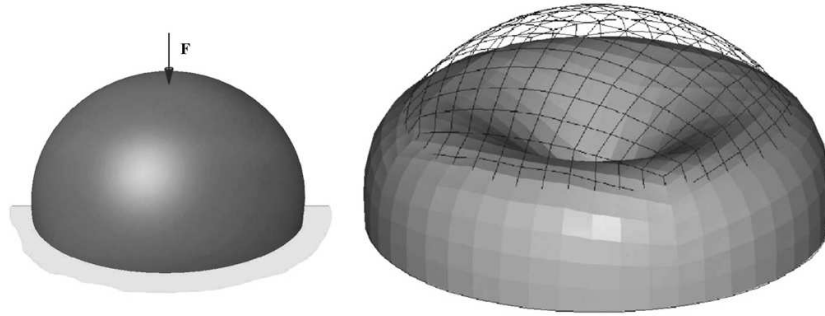
Figure 1.7: Schematic of the deformation of an initially spherical capsule exerted by the colloidal probe AFM technique. Image from [64].

surface have been developed [87]. The atomic force microscope (AFM) uses a sharp tip attached at the end of a cantilever for the measurement or application of forces.

Different from the low sensitivity of capsule compression, the development of the AFM-based apparatus has provided a possibility to measure the sub-micron deformations of microcapsules with good precision. The AFM technique can measure forces between $10^{-11}N$ and $10^{-6}N$ and detect displacements as small as $1nm$, which is suitable for microcapsule deformation studies [29]. Radmacher has used the AFM's high spatial resolution and high force sensitivity to test the stiffness of some biological material including living cells [82].

In the case of the micro-sphere AFM probe technique [11, 24], a spherical solid particle of several microns is attached to the end of AFM cantilever to replace the sharp tip. Compared with a sharp tip, using a spherical particle (e.g. colloidal or glass) probe can introduce a well-defined geometry and increase the sensitivity for small interactions by increasing the interaction area [29]. It can be adapted to perform a deformation similar to the one exerted by the compression technique by using a colloid particle of large radius of curvature [30]. Dubreuil et al. [23] were the first to apply the colloidal probe method for measurement of small deformations of polyelectrolyte multilayer capsules. They obtained quantitative information on material parameters such as the Young's modulus.

The micro-sphere AFM probe technique has also been performed on biological cells by many researchers. Ladjal et al. [56] have used the AFM system with a spherical tip to obtain deformations of the mouse embryonic stem cells (mESC) and determined the Young's modulus of mESC by comparisons of experimental results with some analytical models.

1.3.3 Micropipette technique

The micropipette technique uses a micropipette to suck and deform part of a capsule under a defined hydrostatic pressure. It has been applied with success to measure the mechanical properties of many kinds of capsules including biological ones such as red blood cells. A typical case of capsule deformation by the micropipette technique is shown in Fig. 1.8. A micropipette with an inner diameter of several microns is used for aspiration of a capsule under a controlled pressure drop. The capsule progression into the pipette is monitored by microcopy as a function of the corresponding applied pressure. With the help of mechanical models, it is then possible to determine the elastic properties of capsule membrane.
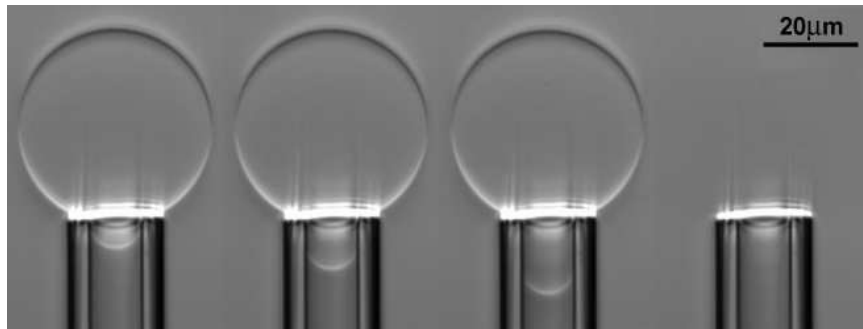
Figure 1.8: Aspiration of phospholipid vesicle by a micropipette under a linear pressure [40].

Kwok and Evans [53] have carried out the micro-mechanical test of the membrane elastic properties of bilayer vesicles with the micropipette technique. Evans and Rawicz [27] have used a sensitive micropipette method to measure the projected surface area of vesicles under tensions in a large magnitude range ($10^{-3} - 10$ dyn/cm). The mechanical behavior of living cells ranging from soft cells like red blood cells to more rigid cells like endothelial cells has been studied with micropipette [42]. An automated micropipette aspiration has been proposed recently by Heinrich and Rawicz [40], which was designed to apply fast and precise tensions to generate and record the deformations of biological and artificial capsules.

Micro-techniques including the micropipette technique and the AFM-based technique have been proved to be able to deform the membrane deformations under controlled tensions. However such techniques cannot be used to characterize large populations of capsules as they require a number of skillful manipulations.
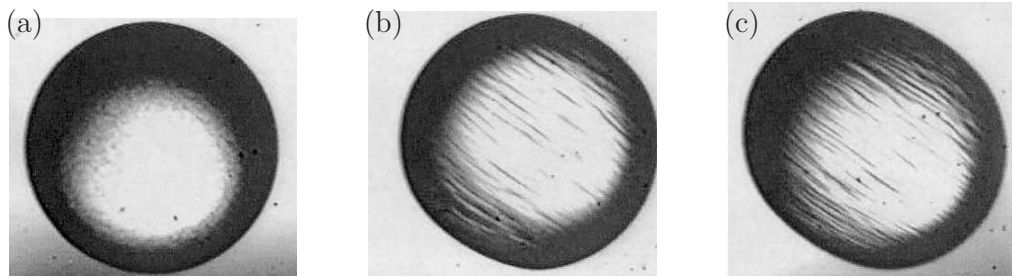
Figure 1.9: Deformation sequences of a polymerized polysiloxane microcapsule [106]. The initially spherical capsule at rest (a) is deformed with shear rates $\dot{\gamma} = 4s^{-1}$ (b) and $\dot{\gamma} = 18s^{-1}$ (c).

1.3.4 Flow in simple flow fields

Subjecting micro-capsules to simple flow fields (e.g. centrifugal flow and simple shear flow) is also a possible method to generate and measure the capsule deformations exerted by controllable viscous forces.

Chang et al. [15] have examined the shapes and orientations of a synthetic capsule with a thin nylon membrane under the simple shear flows generated by a Couette apparatus. The membrane elastic modulus and the membrane viscosity have been deduced by comparison of their experimental results with the predictions of a small-deformation theory proposed by Barthès-Biesel and Sgaier [8]. Walter et al. [106] have also implemented experiments of shear induced deformations on polyamide and polysiloxane microcapsules, as shown in Fig. 1.9. They have shown that the analyzed capsules are predominantly elastic with minor viscous contributions. Two interesting dynamic effects of shape oscillations and membrane folding have been revealed by their experiments.

Pieper et al. [79, 72] have used a classical spinning drop apparatus, which was originally designed to measure the surface tension between two liquids. The deformation of a capsule exerted by increasing rotation rates is measured in the apparatus, and then a theoretical analysis of the mechanics of an initially spherical elastic shell subjected to centrifugal forces allows the deduction of the surface elastic coefficients from the experimental measurements of capsule deformations [72]. A limitation of this technique is linked to the rather low level of mechanical stress that can be applied [59].

1.3.5 Flow in a microfluidic channel

A simple method to measure the elastic properties of membrane is to flow the capsule suspension into a micro-fluidic channel with cross dimension of the same order as the capsule size [59]. Large capsule deformations can be generated by the hydrodynamic forces and boundary confinement, as shown in Fig. 1.10. With the recorded capsule profiles and the corresponding velocities, the membrane mechanical properties can be determined by comparison of experimental and numerical results.
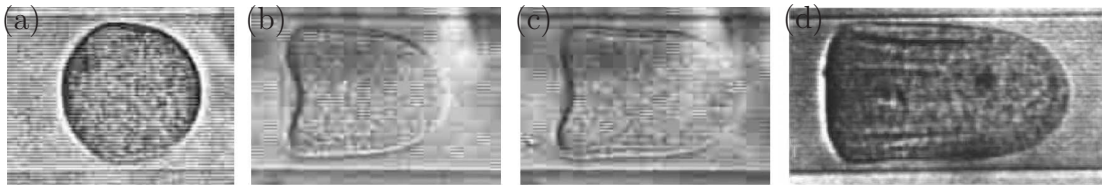
Figure 1.10: Capsule with a cross-linked ovalbumin membrane flowing in a cylindrical glass capillary tube win inner diameter 75 μm. (a)(b)(c) typical deformed capsule shapes for different size ratio [59]. (d) folds on membrane of a large capsule [59, 44].

This technique was initially proposed by Lefebvre et al. to measure the mechanical properties of the membranes of artificial microcapsules [59]. Liquid-filled microcapsules (average diameter of 67 μm) with a membrane made of crossed-linked ovalbumin were flowed into a cylindrical glass capillary tube with internal diameter 75 μm, and then an axisymmetric model was successfully applied to infer the membrane elastic modulus. Chu et al. [17] have applied this technique to characterize cross-linked ovalbumin microcapsule populations fabricated at different reaction pH values and reticulation time for the discrimination of the cross-linking degree. Their results showed that the mechanical analysis method is reliable to discriminate between various cross-linking degrees of microcapsules. The axisymmetric model [19, 59], that considers the flow of a centered spherical capsule in a cylindrical channel, is an essential part in the inverse analysis method for the comparison with experimental results. The feasibility of the axisymmetric model has been shown for millimeter size capsules [85] and for micrometer size capsules [59, 17].

However, folds on the membrane have been observed in experiments of large capsules flowing in a cylindrical pore, as shown in Fig. 1.10(d). Because of their presence, the capsule deformation is not axisymmetric. The feasibility of using the axisymmetric model has to be examined for such three-dimensional (3D) deformation in cylindrical channel.

1.4 Capsule motion and deformation in channel flow

Owing to the high deformability of the membrane, the motion of capsules is different from that of rigid particles or simple droplets. Compared with a rigid particle, large-displacement fluid-structure interactions are always involved in capsule flow. A good understanding of capsule motion and deformation is essential both for fundamental research and industrial applications. Therefore, several researchers have paid attention to the flow-induced behavior of liquid-filled capsules which evidently depends on the external flow conditions. In this section, we specifically summarize experimental and numerical studies of a single liquid-filled capsule flow in a straight channel, which is close to the purpose of this dissertation.

1.4.1 Experimental observations

Just like the circulation of red blood cells in microvessels, capsules are often forced to travel in micro channels to transport an active substance to the place where it needs to be released. The capsule motion and deformation in channels determines, to a great extent, whether the purposes of the applications can be achieved. Numerous experimental studies have been devoted to the study of capsule motion and deformation in various types of channel flow, and many features of the capsule flow in comparable dimensional channels have been revealed.

The capsules flowing through a channel of comparable cross-section usually present large deformations. As shown in Fig. 1.10 (a), the slug shape, which is characterized by a larger membrane curvature at the front than at the rear, have been widely observed in various experiments based on cylindrical tubes for initially spherical artificial capsules with size of a few large millimeters [85] to a few microns [59, 17]. Because the internal pressure at equilibrium state remains constant, the capsule longitudinal profile must take a larger curvature in the front than in the rear to adapt to the viscous pressure drop of the external flow. Thus the classical slug shape is obtained. It is of interest to notice that the slug shapes were also observed by Lefebvre et al. in a square-section microfluidic channels [59]. As shown in Fig. 1.10 (c) and (d), when the capsule deformation is increased by a higher flow strength or other factors, the capsules are frequently shown to deform with a concave membrane curvature in the rear part. These are called parachute shapes [85, 59, 17]. The parachute shapes have also been observed for red blood cells that have initially biconcave shapes both *in vivo* (microcirculation) and *in vitro* experiments [96, 105, 36, 103].

An important phenomenon for capsule flow in confined flow is the wrinkles (or folding) on the membrane (see for example [14, 31, 63]). The wrinkles were initially observed on the membrane of elastic microcapsules deformed in shear flow [106]: capsules with a polysiloxane membrane were found to present wrinkles on the membrane even at low shear rates, while steady deformed shapes were observed for other cross-linked polyamide capsules. Recently, it was shown that the wrinkles could occur on the surface of a large initially spherical capsule with cross-linked ovalbumin membrane when it flows in a cylindrical channel [59, 44], as shown in Fig. 1.10 (d).
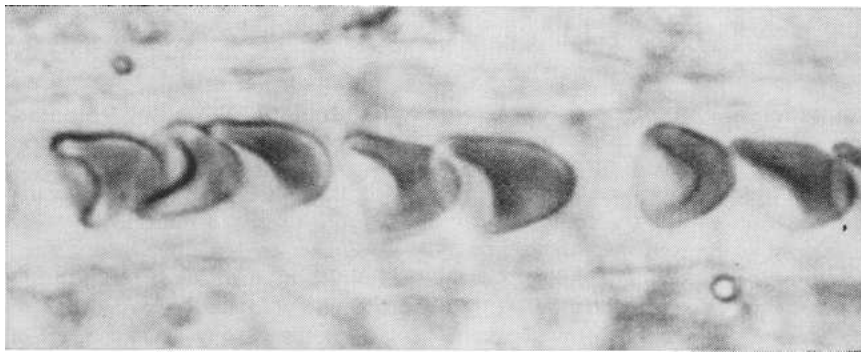
Figure 1.11: Shapes of red blood cells in a capillary vessel [96].

Another well-known problem of non-axisymmetric capsule deformation is the puzzle of slipper-like shapes of red blood cells even if they flow in axisymmetric channels. Motivated by the study of blood microcirculation, the motions and deformations of red blood cells in capillary vessels have drawn a lot of attention from researchers. In parabolic confined flow, red blood cells are found to adopt axisymmetric parachute-like shapes which are a consequence to the combined effects of hydrodynamic forces, membrane elasticity and boundary confinement [47]. But in fact, non-axisymmetric slipper-like shapes have been observed in *in vivo* experiments of red blood cells in microvessels, as shown in Fig. 1.11. Meanwhile, the slipper-like shapes have also been frequently revealed in *in vitro* experiments in straight glass cylindrical tubes which have a comparable radial dimension as that of red blood cells [32, 92, 104, 103]. Such a difference between experimental results and common assumptions continues to attract plenty of attention in the aim of explaining it.

As shown above, the capsule flow in tubes of comparable dimension exhibits specific features including large capsule deformations, wrinkles, non-axisymmetric motion, which need to be taken into account when constructing a model to described the capsule flow in channels.

1.4.2 Numerical simulations

Due to the micro-size of the capsule and its low velocity, the dynamic capsule flow occurs normally at low Reynolds number: the internal and external flows can be described by the Stokes equations. The capsule membrane is most frequently treated as an 2D impermeable hyperelastic isotropic surface. Neglecting bending resistance, the membrane deformation occurs in-plane. In this fluid-structure interaction problem, the capsule deformation depends on the membrane constitutive law. Several membrane constitutive laws have been proposed to describe the mechanics of a thin membrane. For instance, the strain-softening neo-Hookean law follows the assumption that the membrane is an infinitely thin sheet of an isotropic volume incompressible material, while the strain-hardening Skalak law was initially proposed to model the area incompressible membrane of biological cells [59]. More details about the membrane constitutive laws are available in section 2.1.3.2.

1.4.2.1 Pioneer studies

The theoretical studies of the mechanism of microcapsules under different flows were initiated by Barthès-Biesel in 1980 [5]. She examined the small deformations of a spherical capsule suspended in simple shear flow. In this research, the motions of the internal and external flows were described by the Stokes equations, while the dynamic equilibrium of the elastic membrane was expressed as the balance between viscous and elastic forces. With the assumption of small deviation from initial sphericity, a perturbation solution was sought for the deformation and orientation of microcapsule in terms of the magnitude of shear rate, the ratio of internal and external viscosities and the membrane elastic coefficient. The results obtained analytically revealed that the capsule orientation depends on the ratio of internal and external viscosities, the more viscous capsule being more titled towards the streamline. This method was later improved by Barthès-Biesel and Rallison to derive the time-dependent deformation of a microcapsule with a general two-dimensional elastic membrane under arbitrary linear shear flow [7]. However, the perturbation models are valid only for small deviations from the initial spherical shape. They are not suitable for non-spherical capsules under large deformation, such as those experienced by red blood cells under shear stress.

For the motion of a red blood cell in shear flow, Keller and Skalak [49] used equilibrium and energy considerations to predict the cell motion which depends on the ellipsoidal-axis ratios and the ratios of internal and external viscosities. In their

theoretical model, the energy dissipation in the cell membrane was neglected and the deformed cell geometry was a priori given. Two typical motions are observed depending on the values of parameters: a stationary orientation motion or an unsteady flipping motion. However, further research is needed to better simulate the motion and deformation of a red blood cell in shear flow, since the mechanical properties of the cell have not been well taken into account in this simplified model.

With the assumption of a small film between the capsule and the channel wall, the lubrication approximation was proposed by Secomb et al. for the steady axisymmetric deformation of a capsule flowing in a narrow cylindrical channel when the cell and the tube are coaxial [91]. The flow of the suspending fluid in the gap between the capsule and the channel wall was described by the lubrication theory, while the membrane was assumed to be area-incompressible with negligible shear resistance. Their results showed that the cell shape and apparent viscosity were independent of flow rate at moderate and high cell velocities ($\gtrsim 1mm/s$). But the apparent viscosity was found to increase with decreasing flow rate for lower flow velocity, since the membrane stress becomes increasingly important.

1.4.2.2 2D numerical models

The capsule motions in confined flows have also been studied by two-dimensional (2D) numerical models. The capsule membrane surface that encloses the internal medium is modeled as an elastic line, and the mass conservation of internal medium is described by the invariance of the internal surface area.

Over the years, several 2D models of capsule motion and deformation under various confined flows have been constructed with different techniques. Using the lubrication theory for the flow between the capsule and channel wall, Secomb and Skalak [90] proposed a 2D model which considers the effect of asymmetry of cell shape on capillary flow of tightly fitted red blood cells. When several red blood cells travel in group, the zipper-type arrangement has been observed in experiments: the bulging head of each cell is next to the trailing tail of another cell, as shown in [32]. Sugihara-Seki et al. [99] have applied a 2D numerical analysis (based on a finite element method) to study the effect of tank-treading motions on an idealized zipper-type flow. They found that the zipper-type arrangements of red blood cells in capillaries are stabilized by the membrane tank-treading. Thereafter, Secomb et al. [92] proposed a new 2D model for a red blood cell by adding a set of interconnected viscoelastic elements to model the membrane. The capsule motion and deformation computed using a

finite-element numerical method were showed to agree closely with experimental observations. Based on the immersed boundary method, 2D simulations of blood flow in small vessels were proposed by Bagchi [4]. He studied the motion of an individual red blood cell in suspension and the collective motion of many cells. Recently, a 2D vesicle model based on lattice-Boltzmann method has been proposed by Kaoui et al. for the investigation of the effect of confinement between two parallel walls on vesicle dynamics (e.g. the inclination angle and effective viscosity) under shear flow [48].

However, it is questionable that the simplified 2D models can provide quantitatively accurate results of the motion of a capsule which is inherently three-dimensional (3D). In fact, the issue of introducing unrealistic features was already discovered when 2D models were applied for 3D motions [92]. For example, the rates of tank-treading motion predicted by a 2D model [90] were much higher than the experimental observations. It is then necessary to construct a full 3D model of capsule flow, especially when the 3D effects need to be taken into account.

1.4.2.3   3D axisymmetric models

As observed in experiments, a microcapsule flowing in channels often presents large deformations induced by the boundary confinement and the hydrodynamic forces. It is difficult to treat these large capsule deformations by analytical models as nonlinear problems are involved. A numerical model must be developed especially for problems including the membrane shear elasticity and bending resistance [80]. If the capsule flow can be assumed to be axisymmetric, i.e. when the capsule and channel axis coincide, the problem can be solved in a meridian plane.

The first axisymmetric model of capsule flow was carried out by Li et al. for capsules suspended in an elongational flow [62]. The boundary-integral technique was applied to obtain the deformation and motion of a capsule with a Mooney-Rivlin membrane. The membrane surface that encloses the internal medium was then labeled by material points (48 collocation points) on a meridian curve. The model was reasonably accurate and stable for large deformations, even if some numerical smoothing was necessary. Diaz et al. [20] extended this work by applying the boundary element method for the spatial discretization of the capsule contour. High precision and reliability of the axisymmetric model were achieved by using cubic B-splines functions to interpolate the positions of membrane points. A similar problem was then studied and applied to a red blood cell in a straining flow by Pozrikidis [74].

As the motion and deformation are required to be axisymmetric, the models are limited to only a small number of situations. However, the capsule coaxial flow in a

cylindrical channel can be well described by an axisymmtric model. An axisymmetric model for an initial spherical capsule flowing through a constriction was developed by Leyrat-Maurin and Barthès-Biesel [61]. Their unsteady results help the understanding of capsule transient motions during filtration. As observed in experiments, the entrance or exit plugging was well predicted by their model. Subsequently, the axisymmetric motion of capsules passing through cylindrical channels with hyperbolic entrance and exit regions was also studied by Quéguiner and Barthès-Biesel [80]. The boundary integral method was applied for the solutions of internal and external Stokes flow, while the large membrane deformations were assumed to follow a neo-Hookean law. A collocation technique was used for computation and a smoothing method was also implemented to remove the oscillation in the capsule deformed profiles. Their results showed that the entrance length for a capsule to reach a steady deformation depended largely on the capsule size and membrane behavior, even if the capsule entrance was not sensitive to the downstream conditions. The effect of membrane pre-stress on the motion of capsule in a cylindrical channel was also studied by Lefebvre and Barthès-Biesel with the help of a similar axisymmetric model. The numerical results were in good agreement with experimental observations of capsule with alginate membrane [58].

Recently, axisymmetric models have been successfully applied to characterize the membrane mechanical properties of artificial capsule flowing into a cylindrical channel (more details are available in section 1.3.5) [59, 17].

1.4.2.4 3D models

A full 3D model is necessary to describe the capsule dynamic behavior in confined channel for arbitrary cross-section shapes. Over the years, great progress has been made by many researchers in constructing 3D models for such a confined capsule flow.

Hsu and Secomb [43] developed a three-dimensional theoretical analysis for the flow of asymmetric red blood cell along a cylindrical capillary tube. With a tightly-fitting assumption, the lubrication theory was used to compute velocities and pressures of the fluid surrounding the cell. They showed that the membrane tank-treading motion helps to reduce the flow resistance. A more general model was proposed by Pozrikidis to describe the three-dimensional motion of an elastic capsule enclosed by a strain-softening neo-Hookean membrane in a cylindrical tube [77]. The capsule membrane mechanics was coupled with the interior and exterior hydrodynamics by means of surface equilibrium expressed in global Cartesian coordinates, and a boundary-element method was used to simulate the flow of capsules with initially spherical,

oblate ellipsoidal and bioconcave shapes. This model was not based on the assumption of tightly-fitting capsules in channel. It is more general than the lubrication theory since the motion of a capsule with a small size compared with the channel dimension is allowed. However, the problem of numerical instability was shown to arise when negative tensions occur.

In a low-Reynolds-number Poiseuille flow between two parallel plates, the motion of a deformable droplet was firstly examined by Griggs et al. using an efficient 3D boundary-integral method [35]. Subsequently, Doddi and Bagchi [22] have presented a three-dimensional numerical simulation using front-tracking technique based on the immersed boundary method for the capsule migration in a channel flow bounded by two infinite parallel plates. The internal and external fluids were incompressible, Newtonian and with the same density; the effect of viscosity difference was considered. The front-tracking/immersed boundary method uses a single set of equations for the internal and external fluids and introduces body forces in the governing equations for the interface effect. The membrane deformations following the neo-Hookean law was treated with a finite-element method. The lateral migrations of capsules towards the centerline of the channel have been well observed. Thereafter, the flow of a large number of deformable cells confined between parallel plates was also examined by the same method [21].

The elastic capsule flow in a square-section channel was considered by Kuriakose and Dimitrakopoulos [52]. An initial spherical capsule with a strain-hardening membrane was slightly inflated and pre-stressed by a positive osmotic pressure difference between the internal and external fluids. The membrane was discretized by a spectral grid, while a collocation technique was used for the implementation of a spectral boundary integral method. The effects of capsule size and capillary number on the capsule steady states in a square-section channel were examined by this method, but the results are limited to capsules with pre-stress effect to avoid the possible numerical instabilities that could be introduced by the negative tensions on the membrane.

Recently, Walter et al. [108] have developed a coupling method which combines the Boundary Integral (BI) method for fluid flow and the Finite Element (FE) method for the capsule membrane deformation. Numerical stability and high precision have been achieved by this model even when the membrane undergoes in-plane compression, but the results were limited to unbounded flows, such as the simple shear flow and planar hyperbolic flow.

1.5 Objectives

The motion and deformation of flowing capsules depend on the mechanical properties of the membrane. The characterization of these properties is essential for fundamental and applicable research, but it is a challenging task when the capsules have a small size of order a few tens of micrometers. As presented in section 1.3.5, the microfluidic technique, which consists in flowing the capsules in a microfluidic channel with comparable dimensions, offers a practical and efficient method to generate controllable large deformations of micron-sized capsules [59, 17]. To deduce the membrane properties from experimental observations, a proper mechanical model of the capsule flow in a channel is thus necessary for the subsequent inverse analysis. It is therefore necessary to develop a 3D model of the process. We thus study the flow of a single liquid-filled microcapsule in a channel in this dissertation with the main objectives:

- the development of an adapted 3D BI+FE model for confined capsule flows and its validation;

- the comprehensive understanding of capsule flows in channels with circular, square or rectangular section;

- the characterization of membrane mechanical properties of a capsule population by flowing them into a square-section microfluidic channel;

- the effect of membrane constitutive laws on the experimental analysis.

In section 2, the configurations and assumptions of this problem are first presented. The boundary integral formulation and the membrane mechanics are summarized. Following the coupling method proposed in [108], we have developed an adapted 3D BI+FE method for confined capsule flows, and the details of numerical implementations are also included. The validations of the adapted 3D BI+FE model are then performed by comparisons with previous models [52]. It is shown that the adapted model can provide excellent results. In section 3, the capsule flows in channels with circular, square or rectangular section have been simulated using the developed model. In section 4, we propose to use the numerical results to characterize the membrane mechanical properties of capsules flowing in a square-section microfluidic channel. Successful measurements of microcapsules with a crossed-linked ovalbumin membrane are then presented. The effect of membrane constitutive laws on the experimental analysis is also discussed.

Chapter 2

Capsule flow in confined flows

In this chapter, we present a three-dimensional mechanical model for an initially spherical capsule flowing in a channel with constant cross-section. The flow configuration is similar to the axisymmetric case studied by Quéguiner and Barthès-Biesel [80], Diaz and Barthès-Biesel [19] and Lefebvre and Barthès-Biesel [58] or to the three-dimensional situation considered by Pozrikidis [77], Doddi and Bagchi [22] and Kuriakose and Dimitrakopoulos [52]. It will be firstly summarized in the section 2.1. For this fluid-structure interaction problem, a three-dimensional method for infinite capsule flows was proposed by Walter et al. [108], we have adapted it to construct the model of confined flows which integrates the Boundary Integral method (for fluid, in section 2.1.2) and the Finite Element method (for solid, in section 2.2.2). The validation of this model is presented in section 2.3.
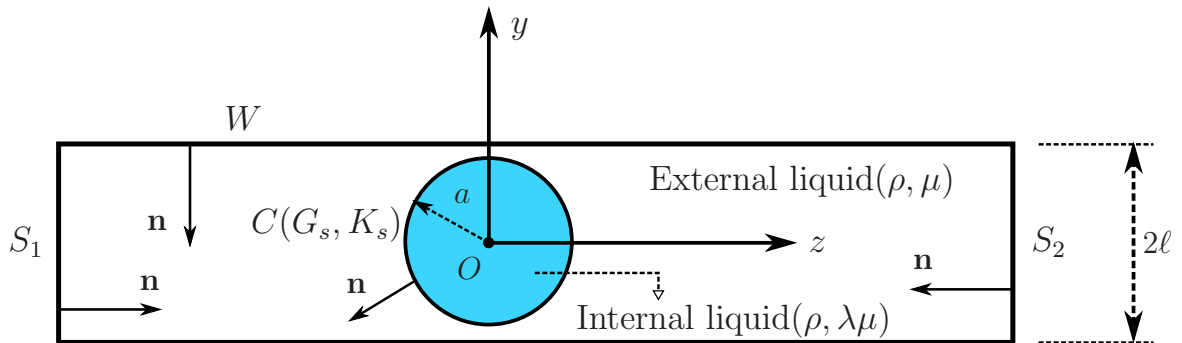
Figure 2.1: Schematic of an initial spherical capsule flowing in a channel with constant cross-section. S_1, S_2 and W denote the surfaces of inlet, outlet and channel wall respectively, C is the capsule thin membrane with shear elastic modulus G_s and surface dilation modulus K_s.

2.1 Problem description

2.1.1 General problem equations

As shown in Fig. 2.1, the capsule consists of an internal droplet of volume V_{cap} enclosed by a very thin membrane. The capsule is initially freely suspended in an external liquid. The internal and external liquids are both incompressible and Newtonian with viscosity $\lambda\mu$ and μ respectively, and equal density ρ.

Diaz and Barthès-Biesel [19] have shown that the viscosity ratio λ has an influence on the time that a capsule needs to reach its steady state in a channel flow. However, the internal viscosity value does not influence the steady capsule deformation as the membrane velocity is zero and the internal fluid is at rest. As we are mostly interested in the steady deformed state of a capsule flowing in straight channels, we take $\lambda = 1$ in this dissertation without loss of generality.

The mass conservation of the internal liquid is satisfied since the membrane is impermeable. As those artificial capsules are usually obtained through interfacial polymerization of a liquid droplet and are thus spherical, the radius of the initially spherical capsule a is defined by

$$a = \sqrt[3]{\frac{3V_{cap}}{4\pi}}. \tag{2.1}$$

It is of interest to notice that, for non-spherical capsules such as red blood cells, we can also use equation 2.1 to deduce an equivalent initial radius. The capsule is assumed to flow inside a channel consisting of a long prismatic tube with constant cross-section of characteristic dimension ℓ. More precisely, 2ℓ is the diameter of a cylindrical tube or the sectional height of a square channel. The capsule deformation and motion inside a channel evidently depend on the effect of boundary confinement, which can be measured by the size ratio a/ℓ, ratio of the capsule initial radius a and the characteristic dimension of the channel ℓ.

We assume that the channel is filled with the suspending liquid flowing with mean velocity V and flow rate Q. The velocity field in the channel in absence of capsule is denoted v^∞. Body forces and buoyancy effects are neglected. Consequently, the capsule that is initially centred on the channel axis remains centred. However, even if the capsule were not initially centred, it would migrate towards the axis [41, 77, 22]. The superscript b is used to denote either the external or the internal liquid ($b = 1$ or 2 respectively). We use $\boldsymbol{v}^{(b)}$, $\boldsymbol{\sigma}^{(b)}$ and $p^{(b)}$ to denote the velocity, stress and pressure fields in the external and internal liquids. Considering a sufficiently small Reynolds

number $Re = \rho V/\mu \ll 1$, the viscous effect is dominant while the inertial effect is insignificant, and the internal and external flows can be described by the equations of Stokes flows

$$\boldsymbol{\nabla} \cdot \boldsymbol{v}^{(b)} = 0, \qquad -\boldsymbol{\nabla} p^{(b)} + \mu^{(b)} \boldsymbol{\nabla}^2 \boldsymbol{v}^{(b)} = \boldsymbol{0} \ \text{ or } \ \boldsymbol{\nabla} \cdot \boldsymbol{\sigma}^{(b)} = 0. \qquad (2.2)$$

We solve the flow in a domain bounded by the cross-sections S_1 at the entrance and S_2 at the exit, the channel wall W and the capsule surface C. The unit normal vector $\boldsymbol{n}$ to all the boundaries points inwards the suspending liquid, as indicated in Fig. 2.1. Considering that S_1 and S_2 are both far enough from the capsule, the capsule flow disturbance vanishes at the entrance and exit. It is then reasonable to neglect the entrance and exit effects. The problem boundary conditions are:

- no flow disturbance on entrance S_1 and exit S_2 as they are far from the capsule:

$$\boldsymbol{v}^{(1)}(\boldsymbol{x}, t) \to \boldsymbol{v}^{\infty}(\boldsymbol{x}), \quad \boldsymbol{x} \in S_1 \cup S_2; \qquad (2.3)$$

- pressure values prescribed on S_1 and S_2:

$$\begin{aligned} p^{(1)}(\boldsymbol{x}, t) &= 0, & \boldsymbol{x} &\in S_1, \\ p^{(1)}(\boldsymbol{x}, t) &= \Delta P(t) + \Delta P^{\infty}, & \boldsymbol{x} &\in S_2. \end{aligned} \qquad (2.4)$$

where ΔP^{∞} is the undisturbed pressure drop between S_1 and S_2 in the absence of capsule and ΔP is the additional pressure drop due to the capsule presence;

- no slip on the channel wall W:

$$\boldsymbol{v}^{(1)}(\boldsymbol{x}, t) = \boldsymbol{0}, \quad \boldsymbol{x} \in W; \qquad (2.5)$$

- no slip on the capsule deformed surface C:

$$\boldsymbol{v}^{(1)}(\boldsymbol{x}, t) = \boldsymbol{v}^{(2)}(\boldsymbol{x}, t) = \frac{\partial}{\partial t} \boldsymbol{x}(\boldsymbol{X}, t), \quad \boldsymbol{x} \in C, \qquad (2.6)$$

where $\boldsymbol{X}$ denotes the initial position of a membrane material point located at position $\boldsymbol{x}$ at time t;

- the load $\boldsymbol{q}$ per unit area on the membrane is due to the viscous traction jump:

$$(\boldsymbol{\sigma}^{(1)} - \boldsymbol{\sigma}^{(2)}) \cdot \boldsymbol{n} = \boldsymbol{q}, \quad \boldsymbol{x} \in C. \qquad (2.7)$$

Since the thickness of a capsule membrane is very small compared with the capsule dimensions and typical radius of curvature, dimensional analysis shows that the inertia effect of a membrane is negligible at a vanishing Reynolds number [108]. We model the capsule membrane as an infinitely thin hyperelastic surface devoid of bending resistance with a shear elastic modulus G_s and an area dilatation modulus K_s. Neglecting bending resistance, the membrane deformation occurs only in-plane and thus the normal vector to the surface remains normal during its deformation.

The capillary number is another important non-dimensional parameter,

$$Ca = \frac{\mu V}{G_s}. \tag{2.8}$$

It compares the viscous forces exerted by the fluids with the elastic forces of the deformable membrane.

2.1.2 Boundary Integral formulation for the fluid problem

Due to linearity of Stokes equations, the instantaneous flow structure only depends on the present boundary configuration and conditions, and is independent of the motion history [75]. This interesting linear property is then the basis of the boundary integral method proposed by Ladyzhenskaya in 1969 [57]. As the boundary integral formulation is classical, we only summarize some basic results that are relevant to the capsule confined flow in this dissertation. More details are available in [75, 6, 77, 108, 52].

2.1.2.1 Boundary Integral formulation for simple capsule flow
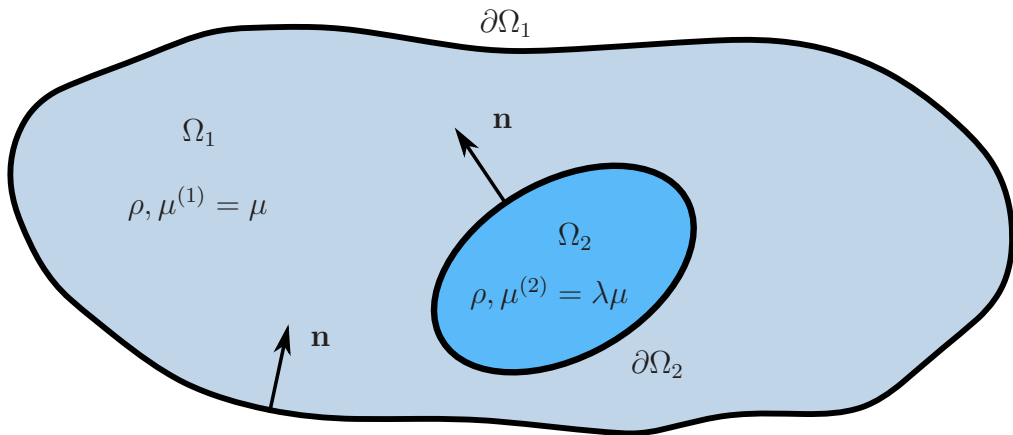
Figure 2.2: Capsule flowing in a suspending liquid.

As shown in Fig. 2.2, we consider an internal droplet Ω_2 with viscosity $\lambda\mu$ separated from an external liquid Ω_1 with viscosity μ by an interface $\partial\Omega_2$. The internal and external liquids have the same density ρ. An imaginary boundary $\partial\Omega_1$ encloses the whole flow domain, and $\boldsymbol{n}$ denotes the normal vector pointing inwards. For such a simple capsule flow, a classical boundary integral representation is available and has been widely applied [75, 77, 108, 52].

$$
\begin{aligned}
\frac{1+\lambda}{2} v_j(\boldsymbol{y}) = &-\frac{1}{8\pi\mu} \int_{\partial\Omega_2} J_{ij}(\boldsymbol{x},\boldsymbol{y})\Delta f_i(\boldsymbol{x})dS(\boldsymbol{x}) \\
&+ \frac{1-\lambda}{8\pi} \int_{\partial\Omega_2}^{PV} v_i(\boldsymbol{x})T_{ijk}(\boldsymbol{x},\boldsymbol{y})n_k(\boldsymbol{x})dS(\boldsymbol{x}) \\
&- \frac{1}{8\pi\mu} \int_{\partial\Omega_1} J_{ij}(\boldsymbol{x},\boldsymbol{y})f_i(\boldsymbol{x})dS(\boldsymbol{x}) \\
&+ \frac{1}{8\pi} \int_{\partial\Omega_1}^{PV} v_i(\boldsymbol{x})T_{ijk}(\boldsymbol{x},\boldsymbol{y})n_k(\boldsymbol{x})dS(\boldsymbol{x}), \qquad \boldsymbol{y}\in\partial\Omega_1\cup\partial\Omega_2,
\end{aligned}
\tag{2.9}
$$

where $f_i = \sigma_{ik}n_k$ is the surface force, $\Delta f_i = f_i^{(1)} - f_i^{(2)}$ denotes the viscous traction jump on interface $\partial\Omega_2$, and the normal vector $\boldsymbol{n}$ points into the external flow domain. PV means that the integral calculation is defined by Cauchy principal value. With $\boldsymbol{r} = \boldsymbol{x} - \boldsymbol{y}$, the Green's function is defined as

$$
J_{ij}(\boldsymbol{x},\boldsymbol{y}) = \frac{\delta_{ij}}{|\boldsymbol{r}|} + \frac{r_i r_j}{|\boldsymbol{r}|^3},
\tag{2.10}
$$

where δ_{ij} is the Kronecker symbol. The free-space Green's function $\boldsymbol{J}(\boldsymbol{x},\boldsymbol{y})$ is also called the Stokeslet [75]. The associated stress tensor T_{ijk} is

$$
T_{ijk}(\boldsymbol{x},\boldsymbol{y}) = -6\frac{r_i r_j r_k}{|\boldsymbol{r}|^5}.
\tag{2.11}
$$

2.1.2.2 Boundary Integral formulation for confined capsule flow

The Stokes equations are recast in boundary integral form for the three-dimensional motion of the internal and external fluids. In view of the linearity of the system, it is reasonable to consider the confined capsule flow to be composed of two parts [77]: the undisturbed channel flow in the absence of capsule and the disturbed channel flow with the presence of capsule. We specifically consider the case of a capsule in a tube and for $\lambda = 1$, the velocity $\boldsymbol{v}(\boldsymbol{x})$ of any point $\boldsymbol{x}$ in the fluid domain of a confined capsule flow is given by Pozrikidis [77]:

$$\boldsymbol{v}(\boldsymbol{x}) = \boldsymbol{v}^\infty(\boldsymbol{x}) - \frac{1}{8\pi\mu}\left[\int_C \boldsymbol{J}(\boldsymbol{r})\cdot\boldsymbol{q}\,dS(\boldsymbol{y}) + \int_W \boldsymbol{J}(\boldsymbol{r})\cdot\boldsymbol{f}\,dS(\boldsymbol{y}) - \Delta P\int_{S_2}\boldsymbol{J}(\boldsymbol{r})\cdot\boldsymbol{n}\,dS(\boldsymbol{y})\right]$$
$$(2.12)$$

where $\boldsymbol{f}$ is the disturbance wall friction due to the capsule presence, and $\boldsymbol{v}^\infty$ denotes the undisturbed flow in the absence of capsule. We can obtain the velocity field $\boldsymbol{v}^\infty$ driven by a pressure drop ΔP^∞ between S_1 and S_2. In the case of a cylindrical channel, it is the Poiseuille flow,

$$\boldsymbol{v}^\infty = 2V[1 - (x^2 + y^2)/\ell^2]\boldsymbol{e}_z, \tag{2.13}$$

where V denotes the mean velocity. For the flow in a rectangular-section channel, the uniform axial velocity distribution $\boldsymbol{v}^\infty = v^\infty(x,y)\boldsymbol{e}_z$ has also been given by a number of textbooks (e.g. [76]),

$$v^\infty(x,y) = \frac{\pi V \sum\left[\frac{1}{n^3} - \frac{\cosh n\pi x/h}{n^3\cosh n\pi W/2h}\right]\sin n\pi(y/h+1/2)}{2\left[\frac{\pi^4}{96} - \sum\frac{\tanh n\pi W/2h}{n^5\pi W/2h}\right]} \quad n = 1,3,\dots \tag{2.14}$$

where W and h denote the width and height of the channel cross-section, respectively. Equation (2.14) is particularized for a square-section channel if $W = h$.

Applying the reciprocal theorem to the flow without capsule $(\boldsymbol{v}^\infty, \boldsymbol{\sigma}^\infty)$ and to the flow with the capsule $(\boldsymbol{v}^{(1)}, \boldsymbol{\sigma}^{(1)})$ in the external flow domain bounded by $S_1 \cup S_2 \cup W \cup C$, we find

$$\int_C[\boldsymbol{\sigma}^{(1)}\cdot\boldsymbol{n}]\cdot\boldsymbol{v}^\infty dS - (\Delta P + \Delta P^\infty)Q = \int_C[\boldsymbol{\sigma}^\infty\cdot\boldsymbol{n}]\cdot\boldsymbol{v}^{(1)}dS - \Delta P^\infty Q, \tag{2.15}$$

where we have used the facts that the flow rate Q is the same with and without the capsule, and that the velocity is zero on W. Now, we apply the reciprocal theorem to $(\boldsymbol{v}^\infty, \boldsymbol{\sigma}^\infty)$ and to $(\boldsymbol{v}^{(2)}, \boldsymbol{\sigma}^{(2)})$ in the internal flow domain bounded by C

$$\int_C[\boldsymbol{\sigma}^{(2)}\cdot\boldsymbol{n}]\cdot\boldsymbol{v}^\infty dS = \int_C[\boldsymbol{\sigma}^\infty\cdot\boldsymbol{n}]\cdot\boldsymbol{v}^{(2)}dS. \tag{2.16}$$

We subtract (2.15) and (2.16), assuming no slip condition on the capsule membrane surface and the membrane load to be caused by traction jump, as indicated by conditions 2.6 and 2.7. We find that the additional pressure drop caused by the capsule is simply given by

$$\Delta P = \frac{1}{Q}\int_C \boldsymbol{v}^\infty(\boldsymbol{x})\cdot\boldsymbol{q}\,dS(\boldsymbol{y}). \tag{2.17}$$

Once the value of the pressure disturbance ΔP is known, the application of equation (2.12) to $\boldsymbol{x} \in W$

$$0 = \int_C \boldsymbol{J}(\boldsymbol{r}) \cdot \boldsymbol{q} \, dS(\boldsymbol{y}) + \int_W \boldsymbol{J}(\boldsymbol{r}) \cdot \boldsymbol{f} \, dS(\boldsymbol{y}) - \Delta P \int_{S_2} \boldsymbol{J}(\boldsymbol{r}) \cdot \boldsymbol{n} \, dS(\boldsymbol{y}) \qquad (2.18)$$

yields an implicit equation for $\boldsymbol{f}$ which is solved numerically.

2.1.3 Solid problem: Membrane mechanics

The capsule motion is a complicated fluid-structure interaction problem, especially as large capsule deformations are often involved in channel flows. Capsule membrane mechanics is thus important. Only some fundamental concepts such as the description of membrane deformation, the constitutive laws and membrane equilibrium, are summarized in this section. Further details are available in previous publications [34, 9, 107].

2.1.3.1 Membrane deformation
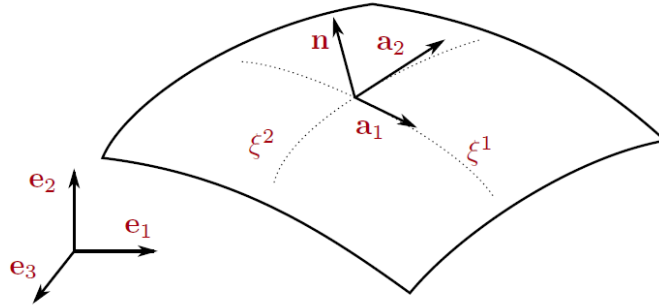
Figure 2.3: The coordinate systems for description of membrane deformation: a local covariant base ($\boldsymbol{a}_1$, $\boldsymbol{a}_2$, $\boldsymbol{n}$) following the surface deformation and a fixed Cartesian base ($\boldsymbol{e}_1, \boldsymbol{e}_2, \boldsymbol{e}_3$) [9]

.

The infinitely thin membrane of the capsule is an impermeable hyperelastic isotropic surface with surface shear elastic modulus G_s and area dilatation modulus K_s. As indicated in Fig. 2.3, the position of a membrane point can be determined by surface curvilinear coordinates (ξ^1, ξ^2). The membrane deformation is thus described by the local covariant ($\boldsymbol{a}_1, \boldsymbol{a}_2, \boldsymbol{n}$) and contravariant ($\boldsymbol{a}^1, \boldsymbol{a}^2, \boldsymbol{n}$) bases constructed from the surface curvilinear coordinates [34, 107]. We consider the undeformed membrane shape as a reference state. The corresponding covariant and contravariant bases are denoted by ($\boldsymbol{A}_1, \boldsymbol{A}_2, \boldsymbol{n}$) and ($\boldsymbol{A}^1, \boldsymbol{A}^2, \boldsymbol{n}$).

(a)

(b)
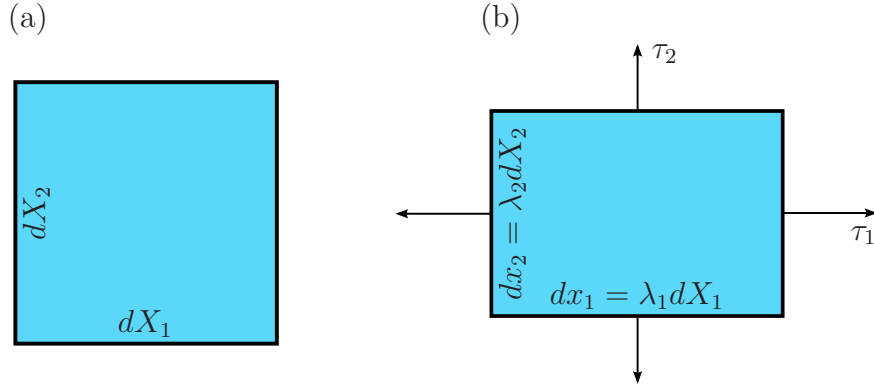
Figure 2.4: In-plane deformation of a membrane element along the principal axes [9]. (a) Reference state; (b) Deformed state with dilation ratios λ_1 and λ_2 under principal tractions τ_1 and τ_2.

We assume that a membrane material point, identified by its position $\boldsymbol{X}$ in the reference state, is displaced to the position $\boldsymbol{x}(\boldsymbol{X}, t)$ in the deformed state. The transformation gradient is defined as $\boldsymbol{F} = \partial \boldsymbol{x}/\partial \boldsymbol{X}$, and the local deformation of the membrane surface is measured by the Green-Lagrange strain tensor

$$e = \frac{1}{2}(\boldsymbol{F}^T \cdot \boldsymbol{F} - \boldsymbol{I}), \tag{2.19}$$

where $\boldsymbol{I}$ is the identity tensor. The membrane deformation can be quantified by the principal dilatation ratios λ_1 and λ_2 in its plane which correspond to two eigenvalues of $\boldsymbol{e}$, as shown in Fig. 2.4. The invariants of the transformation are defined as:

$$I_1 = \lambda_1^2 + \lambda_2^2 - 2, \qquad I_2 = (\lambda_1 \lambda_2)^2 - 1 = J_s^2 - 1, \tag{2.20}$$

where the Jacobian $J_s = det(\boldsymbol{F}) = \lambda_1 \lambda_2$ measures the ratio of deformed membrane area to the reference area.

2.1.3.2 Membrane constitutive laws

Since the membrane is infinitely thin, elastic stress in the membrane are replaced by the Cauchy tension tensor $\boldsymbol{\tau}$ corresponding to forces per unit arc length measured in the plane of the membrane, as shown in Fig. 2.4. When the capsule membrane consists of a sheet of a two-dimensional isotropic material, the Cauchy tension $\boldsymbol{\tau}$ is related to a strain energy function $w_s(I_1, I_2)$ per unit deformed surface area [34, 107, 108],

$$\boldsymbol{\tau} = \frac{1}{J_s}\boldsymbol{F} \cdot \frac{\partial w_s}{\partial \boldsymbol{e}} \cdot \boldsymbol{F}^T. \tag{2.21}$$

28

Using the chain rule, the contravariant representation of $\boldsymbol{\tau}$ can be expressed as [34],

$$\tau^{\alpha\beta} = \frac{2}{J_s}\frac{\partial w_s}{\partial I_1}A^{\alpha\beta} + 2J_s\frac{\partial \omega_s}{\partial I_2}a^{\alpha\beta}. \tag{2.22}$$

where $A^{\alpha\beta}$ and $a^{\alpha\beta}$ represent the contravariant representations of the metric tensors at the reference and deformed states. They are defined respectively as

$$A^{\alpha\beta} = A^\alpha \cdot A^\beta, \;\; a^{\alpha\beta} = a^\alpha \cdot a^\beta \;\; (\alpha, \beta = 1, 2). \tag{2.23}$$

The membrane constitutive law is described by equation (2.22) which gives the relationship between the membrane stresses $\boldsymbol{\tau}$ and the corresponding elastic deformations as functions of the strain energy functions w_s.

A number of constitutive laws are available to model thin hyperelastic membranes [6]. Different material behaviors can be described for large deformation, including the strain-softening behavior of gelled membranes exhibiting rubber-like elasticity or the strain-hardening behavior of membranes made of a polymerized network with strong covalent links. For conciseness, only some widely applied laws with constant material coefficients are summarized in this dissertation.

- The Hooke's law (H) provides a simple linear dependence of tension on the membrane deformation under the assumption of small deformation. The principal tensions are given by

$$\tau_1^H = \frac{G_s}{1 - \nu_s}[\lambda_1^2 - 1 + \nu_s(\lambda_2^2 - 1)] \quad \text{(likewise for } \tau_2\text{)}, \tag{2.24}$$

  where ν_s denotes the surface Poisson ratio describing the relationship between the area dilation modulus K_s and the shear elastic modulus G_s, as $K_s = G_s(1 + \nu_s)/(1 - \nu_s)$ and $\nu_s \neq 1$.

- The neo-Hookean law (NH) describes the behavior of an infinitely thin sheet of a three-dimensional isotropic and incompressible material. It is expressed as

$$\tau_1^{NH} = \frac{G_s}{\lambda_1\lambda_2}\left[\lambda_1^2 - \frac{1}{(\lambda_1\lambda_2)^2}\right] \quad \text{(likewise for } \tau_2\text{)}. \tag{2.25}$$

  It has been found to be the appropriate law to model the behavior of protein-reticulated membranes [12, 59, 17]. The hypothesis of volume incompressibility implies that area dilatation is balanced by membrane thinning, and correspondingly the area dilatation modulus is $K_s = 3G_s$ [6].

- The Mooney-Rivlin law (MR) describes the membrane as a thin sheet of isotropic volume incompressible rubber-like material with a uniform thickness,

$$\tau_1^{MR} = \frac{G_s}{\lambda_1 \lambda_2} \left[\lambda_1^2 - \frac{1}{(\lambda_1 \lambda_2)^2} \right] [\psi + \lambda_2^2(1 - \psi)] \quad \text{(likewise for } \tau_2\text{),} \qquad (2.26)$$

where ψ is a scalar coefficient. For $\psi = 1$, the MR law becomes the NH law.

- The Skalak law (SK) was originally derived to model the large deformations of biological membranes such as red blood cells [97],

$$\tau_1^{SK} = \frac{G_s}{\lambda_1 \lambda_2} \left[\lambda_1^2(\lambda_1^2 - 1) + C(\lambda_1^2 \lambda_2^2)(\lambda_1^2 \lambda_2^2 - 1) \right] \quad \text{(likewise for } \tau_2\text{),} \qquad (2.27)$$

where the first and second terms account for the membrane shear deformation and area dilation respectively. The parameter C measures the ratio of area dilation modulus K_s to shear modulus G_s as $K_s = (1 + 2C)G_s$. A value $C \gg 1$ corresponds to an area incompressible membrane of biological cells. Still the SK law is very general and can model membranes for which K_s and G_s are of the same order of magnitude [12]. It is of interest to notice that, the values K_s/G_s of SK law are the same as those of NH law when $C = 1$. The two laws predict the same tension-strain behavior under small deformations. However, large differences occur under large deformations. It has been shown that the SK law is strain-hardening whereas the NH law is strain-softening under uniaxial stretching ($\tau_1 \neq 0$ and $\tau_2 = 0$) [6].

2.1.3.3 Membrane equilibrium

The membrane motion is governed by the local equilibrium equation

$$\boldsymbol{\nabla}_s \cdot \boldsymbol{\tau} + \boldsymbol{q} = \boldsymbol{0}, \qquad (2.28)$$

where $\boldsymbol{q}$ is the external load exerted by the fluids as given by (2.7) and $\boldsymbol{\nabla}_s\cdot$ is the surface divergence operator in the deformed configuration.

Since the bending modulus of the membrane has been neglected, the capsule wall buckles locally in the regions where the elastic tensions are compressive (as indicated in section 1.4.1). In order to study the post-buckling behavior of the capsule, bending moments and transverse shear forces must be added to equation (2.28) and a constitutive equation must be postulated to relate bending moments and local deformations. It follows that the bending behavior of a capsule is a complicated

problem of shell mechanics that is not completely resolved yet. In this dissertation, we neglect the bending effect.

According to the principal of virtual work, the virtual work of external and internal forces balances for any virtual displacement field $\hat{\boldsymbol{u}}$. For an arbitrary $\hat{\boldsymbol{u}}$, a weak form of equation (2.28) can be deduced by forming the scalar product with $\hat{\boldsymbol{u}}$ on both sides of (2.28) and integrating on the membrane surface C [107],

$$\int_C \hat{\boldsymbol{u}} \cdot \boldsymbol{q} dS + \int_C \hat{\epsilon}(\hat{\boldsymbol{u}}) : \boldsymbol{\tau} dS = 0 \tag{2.29}$$

where $\hat{\epsilon}(\hat{\boldsymbol{u}}) = \frac{1}{2}(\boldsymbol{\nabla}_s \hat{\boldsymbol{u}} + \boldsymbol{\nabla}_s \hat{\boldsymbol{u}}^T)$ denotes the virtual deformation tensor. The first term corresponds to the virtual work of the external fluid forces, while the second side corresponds to the virtual work of the membrane elastic forces.

2.1.3.4 Pre-stress effect on membrane

We assume that a positive pressure difference p may exist between the internal and external liquids of capsule. This situation is often encountered for artificial capsules enclosed by semipermeable membranes which are permeable to small molecules as water but impermeable to large molecules [51, 9]. During the storage of capsules, partial dissolution of membrane material into the internal liquid can lead to an increase in the internal liquid concentration, because large molecules are trapped inside the capsule by the semipermeable membrane [94, 58]. The presence of a concentration jump between the internal and external liquids introduces a positive osmotic pressure difference p, and the initial spherical capsule of radius a is thus pre-stressed and inflated to a new radius a_p.

We introduce preinflation parameter α to account for the relationship of inflated radius a_p and initial radius a, as $a_p/a = 1 + \alpha$. Since the capsule is spherical, the membrane deformation is isotropic and can be measured by the principal dilatation ratios $\lambda_1 = \lambda_2 = \lambda_p = 1 + \alpha$, while the corresponding isotropic membrane tensions are given by the Laplace law [9]

$$\tau_1 = \tau_2 = \tau_p = \frac{1}{2}pa_p. \tag{2.30}$$

The pre-stress effect has a significant effect on the capsule deformations. For example, Lac and Barthès-Biesel showed that the deformation of a capsule flowing in unbounded simple shear flow was lowered by the pre-stress effect for a given shear rate [54]. They have also shown that the pre-stress effect can help reduce the membrane buckling instability observed at low flow strength [55]. Recently, the pre-stress

effect was also employed by Kuriakose and Dimitrakopoulos to reduce the membrane buckling instability of capsule flowing in a square channel [52].

2.2 Adapted BI+FE method for bounded capsule flow

The fluid-structure interaction problem can be solved by an adapted model based on the coupling method proposed by Walter et al. [107, 108], which was developed for unbounded capsule flows by the coupling of a Finite Element (FE) method (for the capsule wall mechanics) and a Boundary Integral (BI) method (for the internal and external flows).

In this section, we first introduce the mesh generations for discretizing the surfaces of the capsule membrane C, the channel boundary W and outlet S_2 into unstructured triangles. We simply summarize the FE formulation for the membrane equilibrium [107, 108, 9], and subsequently construct the adapted coupling BI+FE numerical procedure for capsules in confined flow. A pre-deformation treatment for large capsules $a/\ell \geq 1$ is also proposed.

2.2.1 Capsule and channel meshes generation

All the surfaces (C, W and S_2) are discretized by triangular elements using isoparametric interpolation. This means that all the unknowns (e.g., point position $\boldsymbol{y}$, velocity $\boldsymbol{v}$ and load on membrane $\boldsymbol{q}$) are interpolated with the same shape functions.
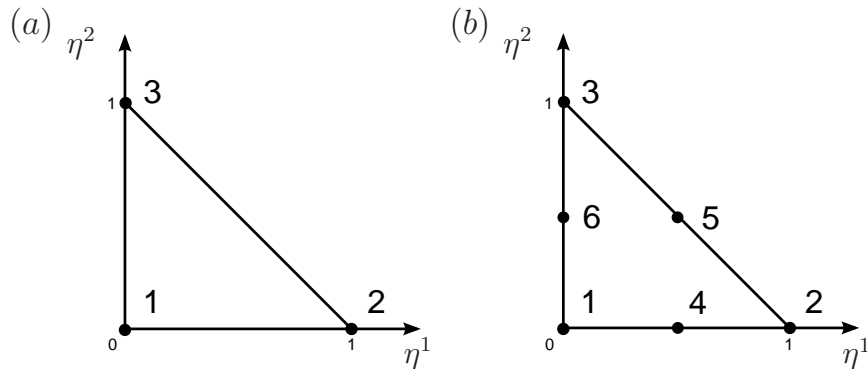
Figure 2.5: Illustrations of reference coordinate system and node numbering. (a) P_1 element; (b) P_2 element.

As shown in Fig. 2.5, we use two types of elements in surface discretizations:

- the flat P_1 element defined by 3 nodes at each vertex of a triangle. Linear interpolation is then used.

- the curved P_2 element defined with 6 nodes respectively at each vertex or the middle of each side. Quadratic interpolation is then used.

The positions of points on an element are determined by the intrinsic coordinates (η^1, η^2), defined such that η^1, η^2 and $1 - \eta^1 - \eta^2$ lie in the interval $[0, 1]$ [9]. The value of an interpolated quantity at a point, for example a vectorial quantity $\boldsymbol{f}$, can be calculated from nodal values of this quantity. If we suppose $f_{X_j}^p$ is the jth Cartesian component of $\boldsymbol{f}$ at node p, and $p \in 1, ..., nn$ where nn is the number of nodes of the element, we have an interpolated formulation for $\boldsymbol{f}$ as

$$\boldsymbol{f}(\eta^1, \eta^1) = \sum_{p=1}^{nn} f_{X_j}^p N^{(p)}(\eta^1, \eta^1)\boldsymbol{e}_j, \tag{2.31}$$

where the shape function $N^{(p)}(\eta^1, \eta^1)$ depends on the element type. For P_1 elements, we have:

$$
\begin{aligned}
N^{(1)}(\eta^1, \eta^2) &= 1 - \eta^1 - \eta^2, \\
N^{(2)}(\eta^1, \eta^2) &= \eta^1, \\
N^{(3)}(\eta^1, \eta^2) &= \eta^2.
\end{aligned}
\tag{2.32}
$$

For P_2 elements, the expressions are:

$$
\begin{aligned}
N^{(1)}(\eta^1, \eta^2) &= (1 - \eta^1 - \eta^2)(1 - 2\eta^1 - 2\eta^2), \\
N^{(2)}(\eta^1, \eta^2) &= \eta^1(2\eta^1 - 1), \\
N^{(3)}(\eta^1, \eta^2) &= \eta^2(2\eta^2 - 1), \\
N^{(4)}(\eta^1, \eta^2) &= 4\eta^1(1 - \eta^1 - \eta^2), \\
N^{(5)}(\eta^1, \eta^2) &= 4\eta^1\eta^2, \\
N^{(6)}(\eta^1, \eta^2) &= 4\eta^2(1 - \eta^1 - \eta^2).
\end{aligned}
\tag{2.33}
$$

The mesh of the initial spherical capsule is obtained by firstly inscribing an icosahedron (regular polyhedron with 20 triangular faces) in the sphere [83, 108]. Each triangular face is divided into 4 triangular sub-elements by placing a new node in the middle of each side. The new nodes are then projected radially onto the sphere, and we repeat the procedure until the desired number of P_1 elements is reached. We use $N_e^{(c)}$ and $N_n^{(C)}$ to denote the total number of elements and nodes on the capsule surface C. A typical capsule surface meshed by P_1 elements at different precision is presented in figure 2.6. The P_2 elements are obtained by cutting each edge in half in the last step and then projecting the new nodes onto the sphere. Walter et al. [108] have studied the effects of P_1 and P_2 elements on unbounded flows, including

(a) (b)
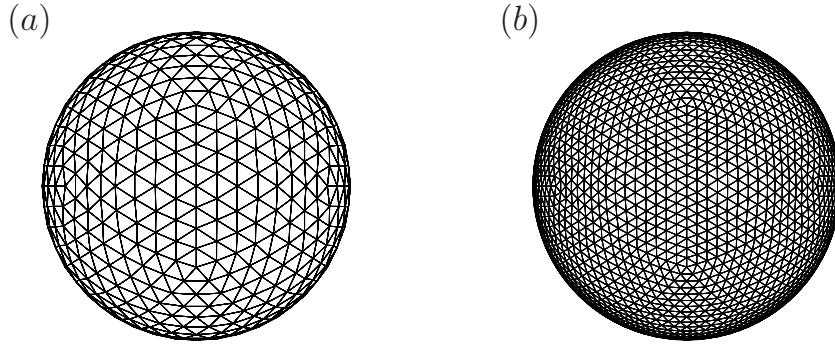
Figure 2.6: Typical capsule membrane surface meshed with flat triangles (P_1 elements) (a) $N_N = 642$, $N_E = 1280$; (b) $N_N = 2562$, $N_E = 5120$.

pre-stressed isotropic deformations and capsule flowing in simple shear flow, they found that both element types behaved well and that the results converged toward a common solution. Following their work, P_2 elements are employed for capsule mesh generations in present study. For all of the following 3D computations, we use a capsule mesh with $N_e^{(c)} = 1280$ elements and $N_n^{(c)} = 2562$ nodes. Assuming all the elements are perfect triangles, we can find the characteristic size of this capsule mesh $\Delta h_C = O(0.1a)$. Validation of this capsule mesh is done by comparison with a finer mesh, as presented in section 2.3.1.

(a) (b)
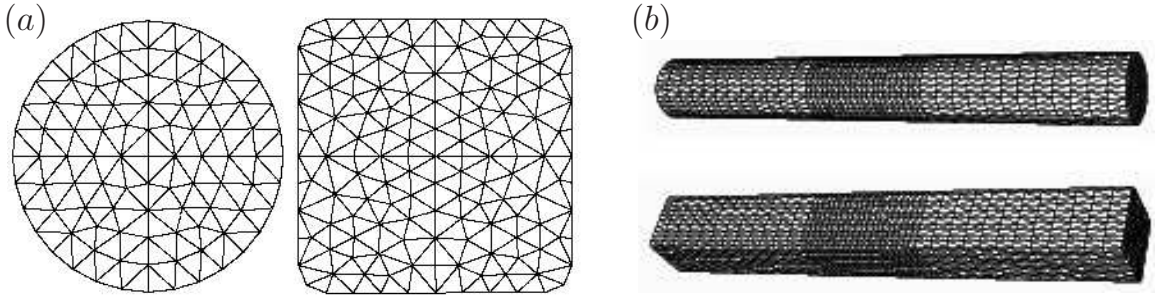
Figure 2.7: (a) Meshes of the circular and square cross-sections; (b) Meshes of the prismatic tubes.

The channel mesh is generated with P_1 elements using Modulef (INRIA Rocquencourt, France). We first generate the two-dimensional geometry of the tube cross-section with the desired shape by unstructured triangular elements having a mesh size $\Delta h_S = O(0.14\ell)$, as indicated in Fig. 2.7(a). The corners of the rectangular cross-section have been rounded with a circle (radius Δh_S) in order to avoid corner effects when solving for the flow. Since the boundary integral method only requires the surface to be meshed, the mesh of the tube external surface is extracted from the

volume mesh. The nodes and elements contained on the inlet surface S_1 are removed, as no boundary condition is numerically applied on them. The resulting open surface mesh on the boundary wall W and outlet surface S_2 is the final channel mesh used for our simulations. The total numbers of elements and nodes on the boundary wall W and the exit surface S_2 are denoted by $N_e^{(w)}$ and $N_n^{(w)}$, $N_e^{(o)}$ and $N_n^{(o)}$ respectively. As shown in Fig. 2.7(b), we employ a refined mesh with characteristic length $\Delta h_W = O(0.14\ell)$ in the central section of the tube with length $L_c = 4\ell$, while the inlet and outlet sections, each of length $L_{io} = 6\ell$, are with $\Delta h_W = O(0.22\ell)$.

We will discuss the effects of channel mesh in section 2.3.1, including the mesh size and the channel lengths.

2.2.2 FE formulation for membrane equilibrium

Considering a deformed capsule shape, equation (2.29) deduced from the virtual work principal is solved to determine the unknown membrane load $\boldsymbol{q}$ from a virtual displacement $\hat{\boldsymbol{u}}$. Based on the capsule mesh presented in section 2.2.1, we discretize the domain into a finite element space ϑ_h using isoparametric interpolations [107, 108, 9]. The objective of this problem is to express (2.29) as a linear system of algebraic equations at the membrane nodes. As the integral over the membrane surface C can be decomposed into a sum over all individual elements, the first term of (2.29) is expressed as

$$
\begin{aligned}
\int_C \hat{\boldsymbol{u}} \cdot \boldsymbol{q} \, dS &= \sum_{el} \hat{u}_{X_j}^{(p)} [\int_0^1 \int_0^{1-\eta^2} N^{(p)} N^{(q)} \sqrt{|a_{\alpha\beta}|} d\eta^1 d\eta^2] q_{X_j}^{(q)} \\
&= \sum_{el} \{\hat{u}_{el}\}^T [M_{el}] \{q_{el}\},
\end{aligned}
\tag{2.34}
$$

where el denotes the number of elements, $\sqrt{|a_{\alpha\beta}|} d\eta^1 d\eta^2$ is the local differential surface element. The vectors $\{q_{el}\}$ and $\{\hat{u}_{el}\}$ of size $3nn$ are respectively the Cartesian components of the discrete load and the virtual displacement at element nodes,

$$
\begin{aligned}
\{q_{el}\} &= q_1^{(1)}, q_2^{(1)}, q_3^{(1)}, \; ..., \; q_1^{(nn)}, q_2^{(nn)}, q_3^{(nn)}, \\
\{\hat{u}_{el}\} &= \hat{u}_1^{(1)}, \hat{u}_2^{(1)}, \hat{u}_3^{(1)}, \; ..., \; \hat{u}_1^{(nn)}, \hat{u}_2^{(nn)}, \hat{u}_3^{(nn)}.
\end{aligned}
\tag{2.35}
$$

Because the capsule deforms, the differential surface element $\sqrt{|a_{\alpha\beta}|} d\eta^1 d\eta^2$ on a deformed membrane is not fixed, thus the matrix $[M_{el}]$ involving $\sqrt{|a_{\alpha\beta}|} d\eta^1 d\eta^2$ needs to be recalculated at each time step.

Since the capsule surface C is discretized with $N_n^{(c)}$ nodes, we assemble the vectors $\{q_{el}\}$ and $\{\hat{u}_{el}\}$ into their global counterparts $\{q\}$ and $\{\hat{u}\}$ of size $3N_n^{(c)}$, and do the same for matrix $[M_{el}]$ into $[M]$ of size $3N_n^{(c)} \times 3N_n^{(c)}$. Equation (2.34) becomes

$$\int_C \hat{\boldsymbol{u}} \cdot \boldsymbol{q} dS = \{\hat{u}\}^T [M]\{q\} \tag{2.36}$$

The second term of (2.29) can be decomposed as

$$\int_C \hat{\epsilon}(\hat{\boldsymbol{u}}) : \boldsymbol{\tau} dS = \sum_{el} [\int_0^1 \int_0^{1-\eta^2} \hat{\epsilon}_{\alpha\beta} \tau^{\alpha\beta} \sqrt{|a_{\alpha\beta}|} d\eta^1 d\eta^2], \tag{2.37}$$

where the contravariant representation of tension $\tau^{\alpha\beta}$ can be computed by equation (2.22) and is highly dependent on the membrane constitutive laws that we choose. The virtual strain tensor $\hat{\epsilon}_{\alpha\beta}$ depends on the virtual displacement $\hat{\boldsymbol{u}}$:

$$\hat{\epsilon}_{\alpha\beta} = \frac{1}{2}[\hat{u}_{\alpha,\beta} + \hat{u}_{\alpha,\beta} - 2\Gamma^i_{\alpha\beta}\hat{u}_i], \quad \alpha, \beta = 1, 2, \text{ and } i, j = 1, 2, 3, \tag{2.38}$$

where $\Gamma^i_{\alpha\beta} = \boldsymbol{a}_{\alpha,\beta} \cdot \boldsymbol{a}^i$ denotes the Christoffel symbol, $\hat{u}_i = a_i^{X_j} \hat{u}_{X_j} = N^{(p)} a_i^{X_j} \hat{u}_{X_j}^{(p)}$ is the covariant representation of $\hat{\boldsymbol{u}}$ where $a_i^{X_j}$ is the Cartesian component of local covariant base $\boldsymbol{a}_i$. Following the work of Walter et al. [107], the virtual strain can be written as

$$\hat{\epsilon}_{\alpha\beta} = \hat{u}_{X_j}^{(p)} \chi_{\alpha\beta}^{(p)j}, \tag{2.39}$$

where $\chi_{\alpha\beta}^{(p)j}$ has a form

$$\chi_{\alpha\beta}^{(p)j} = \frac{1}{2} N_{,\beta}^{(p)} a_\alpha^{X_j} + \frac{1}{2} N_{,\alpha}^{(p)} a_\beta^{X_j} + N^{(p)} a_{\alpha,\beta}^{X_j} + \Gamma^i_{\alpha\beta} N^{(p)} a_i^{X_j}. \tag{2.40}$$

Factoring the virtual displacement $\hat{u}_{X_j}^{(p)}$ out of the integral, we assemble the vectors $\{\hat{u}_{el}\}^T$ and $\{R_{el}\}$ into their global counterparts and obtain

$$\begin{aligned} \int_C \hat{\epsilon}(\hat{\boldsymbol{u}}) : \boldsymbol{\tau} dS &= \sum_{el} \hat{u}_{X_j}^{(p)} [\int_0^1 \int_0^{1-\eta^2} \chi_{\alpha\beta}^{(p)j} \tau^{\alpha\beta} \sqrt{|a_{\alpha\beta}|} d\eta^1 d\eta^2] \\ &= \sum_{el} \{\hat{u}_{el}\}^T \{R_{el}\} \\ &= \{\hat{u}\}^T \{R\}. \end{aligned} \tag{2.41}$$

Like the matrix $[M]$, the vector $\{R\}$ of size $3N_n^{(c)}$ also depends on $\sqrt{|a_{\alpha\beta}|} d\eta^1 d\eta^2$, and thus needs to recomputed at each time step. Assembling the two equations (2.36) and (2.41), we finally obtain the finite element formulation for membrane equilibrium

$$\{\hat{u}\}^T[M]\{q\} = -\{\hat{u}\}^T\{R\}. \tag{2.42}$$

As it is verified for any virtual displacement $\{\hat{u}\}^T \in \vartheta_h$, we can simplify it to

$$[M]\{q\} = \{R\}. \tag{2.43}$$

2.2.3 Coupling BI+FE numerical procedure

Walter et al. have proposed a coupling BI+FE method for unbounded capsule flows [107, 108]. Following their method, we have constructed an adapted coupling BI+FE numerical procedure for the capsule confined flows as follows:

1. **Initialization** Given an initial capsule shape, we discretize the capsule membrane surface C by $N_n^{(c)}$ nodes and $N_e^{(c)}$ elements. All the membrane points at reference state are identified and recorded in the position vector $\boldsymbol{X}$. The position vector of the capsule mass center at reference state $\boldsymbol{X}_O$ is also provided. As mentioned in section 2.2.1, the fixed channel is also discretized.

2. **Membrane load** At any time t, the positions of the membrane material points are denoted by $\boldsymbol{x}(\boldsymbol{X}, t)$. We solve equation (2.43) and determine the membrane load vector $\{q\}$.

3. **Pressure drop** Knowing the membrane load $\{q\}$, we can discretize the boundary condition (2.17) into a linear system of algebraic equations for the additional pressure drop ΔP caused by the capsule presence, as

$$\Delta P = \frac{1}{Q}\{v^\infty\}^T[M]\{q\}, \tag{2.44}$$

where $\{v^\infty\}$ is the undisturbed velocity vector of membrane points, which is obtained by assembling the Cartesian components of global undisturbed velocity vectors. The undisturbed velocity in a channel with circular or rectangular(square) section is given by equations (2.13) and (2.14). Since the integral of equation (2.17) is on the capsule surface C, the vector $\{v^\infty\}$ arranged into the global counterpart is of size $3N_n^{(c)}$, as

$$\{v^\infty\} = \{v^{\infty(1)}_{X_1}, v^{\infty(1)}_{X_2}, v^{\infty(1)}_{X_3} \quad \cdots \quad v^{\infty(N_n^{(c)})}_{X_1}, v^{\infty(N_n^{(c)})}_{X_2}, v^{\infty(N_n^{(c)})}_{X_3}\}. \tag{2.45}$$

The matrix $[M]$ and the vectors $\{q\}$ are given by equation (2.43). Equation (2.44) is computed to determine the value of ΔP.

4. **Wall friction** The other boundary condition, equation (2.18), can be also discretized into the set of algebraic equations,

$$0 = [J_{wc}][M]\{q\} - \Delta P[J_{wo}][M_o]\{n_o\} + [J_{ww}][M_w]\{f\}, \tag{2.46}$$

where $[J_{wc}]$, $[J_{wo}]$ and $[J_{ww}]$ denote the matrices of the Green's functions for the integrals on surfaces C, S_2 and W, that are, respectively of size $3N_n^{(w)} \times 3N_n^{(c)}$, $3N_n^{(w)} \times 3N_n^{(o)}$ and $3N_n^{(w)} \times 3N_n^{(w)}$. The vector $\{n_o\}$ of size $3N_n^{(o)}$ denotes the normal vectors on the channel outlet S_2. In the same way as the matrix $[M]$ is the integral of the shape functions over the capsule surface C in equation (2.34), the matrices $[M_o]$ and $[M_w]$ are the equivalent integrals on surfaces of S_2 and W. As the channel boundary surfaces are fixed, it is of interest to note that the matrices $[M_o]$ and $[M_w]$ need to be calculated only once at the beginning of the procedure, while the matrix $[M]$ on the deformable capsule surface needs to be computed at each time step.

Incorporating ΔP and $\{q\}$ into equation (2.46), we can obtain the friction vector on the wall $\{f\}$ by solving the linear system.

5. **Membrane velocity** The velocity vector of the membrane points $\boldsymbol{v}$, provided by the BI formulation (2.12), can be expressed as

$$\{v\} = \{v^\infty\} - \frac{1}{8\pi\mu}[J_{cc}][M]\{q\} + \frac{\Delta P}{8\pi\mu}[J_{co}][M_o]\{n_o\} - \frac{1}{8\pi\mu}[J_{cw}][M_w]\{f\}, \tag{2.47}$$

where the matrices of the Green's functions $[J_{cc}]$, $[J_{co}]$ and $[J_{cw}]$ are respectively of size $3N_n^{(c)} \times 3N_n^{(c)}$, $3N_n^{(c)} \times 3N_n^{(o)}$ and $3N_n^{(c)} \times 3N_n^{(w)}$. Since the capsule membrane load $\{q\}$, channel wall friction $\{f\}$ and pressure drop ΔP are already determined, the velocity vector $\{v\}$ can be obtained by solving the linear system (2.47).

6. **Membrane displacement** Using an explicit second-order Runge-Kutta method, the new position of the membrane points $\boldsymbol{x}$ is calculated by time-integration of the kinematic equation (2.6):

$$\boldsymbol{v}(\boldsymbol{x}, t) = \frac{\partial}{\partial t}\boldsymbol{x}(\boldsymbol{X}, t), \quad \boldsymbol{x} \in C. \tag{2.48}$$

7. **Centroid velocity** From the new position $\boldsymbol{x}(\boldsymbol{X}, t)$ of the membrane points, we deduce the new position of the capsule mass center $\boldsymbol{x}_O = (x_o, \ y_o, \ z_o)$. The velocity of the capsule mass center $\boldsymbol{v}(O, t)$ is thus determined from the values of $\boldsymbol{x}_O$ at two successive time points,

$$\boldsymbol{v}(O, t) = \frac{\boldsymbol{x}_O(t) - \boldsymbol{x}_O(t - \Delta t)}{\Delta t}, \tag{2.49}$$

where Δt is the time step. It is of interest to notice that the position of the capsule mass center $\boldsymbol{x}_O$ is computed after the displacement of the membrane points at each time step. We finally translate the capsule points by $-z_o \boldsymbol{e}_z$ to ensure that the flowing capsule is always placed in the central section of the channel.

8. **Steady results** The procedure from step 2 to step 6 is repeated until a steady state is reached, which occurs when the surface of the capsule varies by less than $5 \times 10^{-4} \times (4\pi a^2)$ over a non-dimensional time $Vt/\ell = 1$.

In numerical implementation, we apply 6 Hammer points on each element for the surface integrations involved in the calculation of matrices $[M]$, $[M_w]$, $[M_o]$ and vector $\{R\}$ [37, 108]. The linear systems are solved using the sparse solver Pardiso [88, 89, 108]. We find that the numerical method is conditionally stable when the time step Δt satisfies a condition similar to the one found for the unbounded case [108]:

$$\frac{V}{\ell} \Delta t < O(\frac{\Delta h_C}{\ell} Ca), \tag{2.50}$$

All the results shown hereafter have been obtained with a time step $V\Delta t/\ell = 5 \times 10^{-5}$.

2.2.4   Pre-deformation for large capsules $a/\ell \geq 1$

When the capsule initial size is larger than the channel cross dimension, we pre-deform the capsule into an spheroid that fits inside the channel. Correspondingly, a point initially located at (X, Y, Z) on the capsule surface is displaced to (x, y, z), such that

$$z = k_1 Z, \quad y = k_2 Y, \quad x = k_2 X, \tag{2.51}$$

with $k_2^2 k_1 = 1$, in view of the volume conservation requirement. We choose k_2 such that $y/\ell = 0.9$, in order to leave a reasonably thick liquid film between the membrane and the channel wall. The resulting elastic tensions in the membrane and the load

q exerted on the fluid are computed by means of the finite element method. The capsule deformation is then followed in time as explained above.

(a) channel wall (b) channel wall

Sphere $a/\ell \geq 1.0$ Pre-deformation
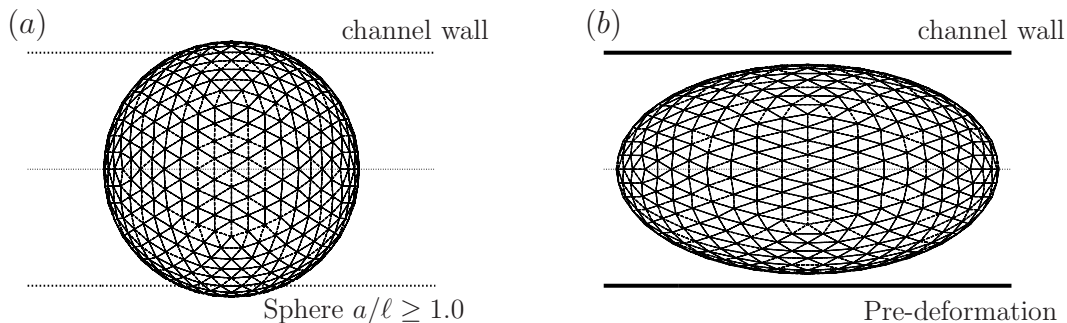
Figure 2.8: Schematic of pre-deformation for large capsules. (a) Large capsule of size ratio $a/\ell \geq 1.0$; (b) A large spherical capsule is pre-deformed into a spheroid to fit inside the channel.

2.3 Validations

The validations of the BI+FE model adapted for confined flows are presented in this section. We first compare the results with different capsule mesh sizes to show that the mesh we use is adapted to the problem. We then study the effects of pre-deformation and of the channel length. Finally, the validations of our adapted BI+FE model are carried out by comparisons with the results of a published model in [52] that considered a pre-stressed capsule flowing in a square-sectional channel, as presented in 2.3.4.

2.3.1 Mesh size

In the previous work of Walter et al. [108], the effects of the capsule mesh size have been studied in the case of unbounded capsule flows. They found that the error on the capsule shape is mainly determined by the capsule mesh size and the time step. With a capsule mesh discretized by $N_e^{(c)} = 1280$ P_2 elements, it is conditionally stable and the error is of order $O(\Delta h_C^4)$ as shown in [108]. Since the capsule typically presents wrinkles in a channel flow, we specifically study the effects of mesh size on wrinkles and deformed capsule shapes in this section.

The capsule of size ratio $a/\ell = 0.9$ is assumed to flow inside a cylindrical channel at a moderate capillary number $Ca = 0.05$. The capsule membrane mechanics is
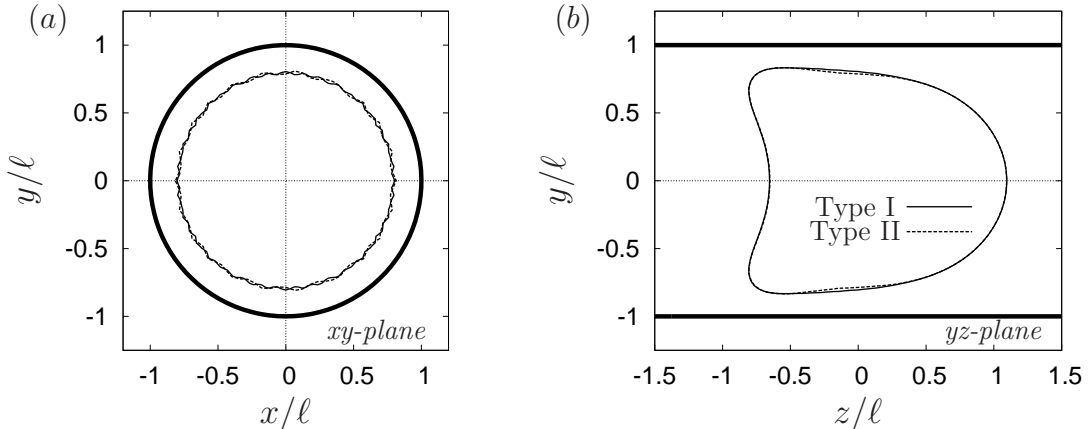
Figure 2.9: Comparisons of steady capsule profiles of different mesh sizes. (a) Cross-sectional profiles on *xy-plane*; (b) Longitudinal profiles on *yz-plane*. $Ca = 0.05$, $a/\ell = 0.9$, NH membrane, cylindrical channel.

described by the neo-Hookean law. We perform the discretization of the capsule surface with two different mesh sizes: a very fine mesh (Type I) that is discretized by $N_e^{(c)} = 5120$ P_2 elements with characteristic mesh size about $\Delta h_C = O(0.05a)$; a moderate mesh (Type II) that is discretized by $N_e^{(c)} = 1280$ P_2 elements with $\Delta h_C = O(0.1a)$. The cylindrical tube of total length $L = 16$ is discretized with the method mentioned in section 2.2.1. We employ a refined mesh with $\Delta h_w = O(0.07\ell)$ in the central section of length $L_c = 4$ for the fine capsule mesh (Type I), and $\Delta h_w = O(0.14\ell)$ for the moderate capsule mesh (Type II).

The deformed capsule shapes at equilibrium states are obtained by 3D computations. We determine the deformed capsule intersections on the *xy-*, *xz-* and *yz-*planes for $z_o = 0$. As the membrane is undergoing compression, it tends to buckle. There is no bending resistance in our 3D model to regulate the process, so that the wrinkles are controlled by the mesh (Fig. 2.9(a)). the wavelength of the oscillations is decreased when the mesh size decreases by a factor in the case of the fine mesh (Type I). However, the longitudinal and cross-profiles obtained by both mesh sizes are perfectly superimposed, as shown in Fig. 2.9. It implies that the moderate capsule mesh (Type II) is appropriate for our simulations.

2.3.2 Pre-deformation

Considering a typical spherical capsule of $a/\ell = 0.9$ enclosed by a neo-Hookean membrane and flowing in a cylindrical channel at $Ca = 0.5$, we have checked the effect of
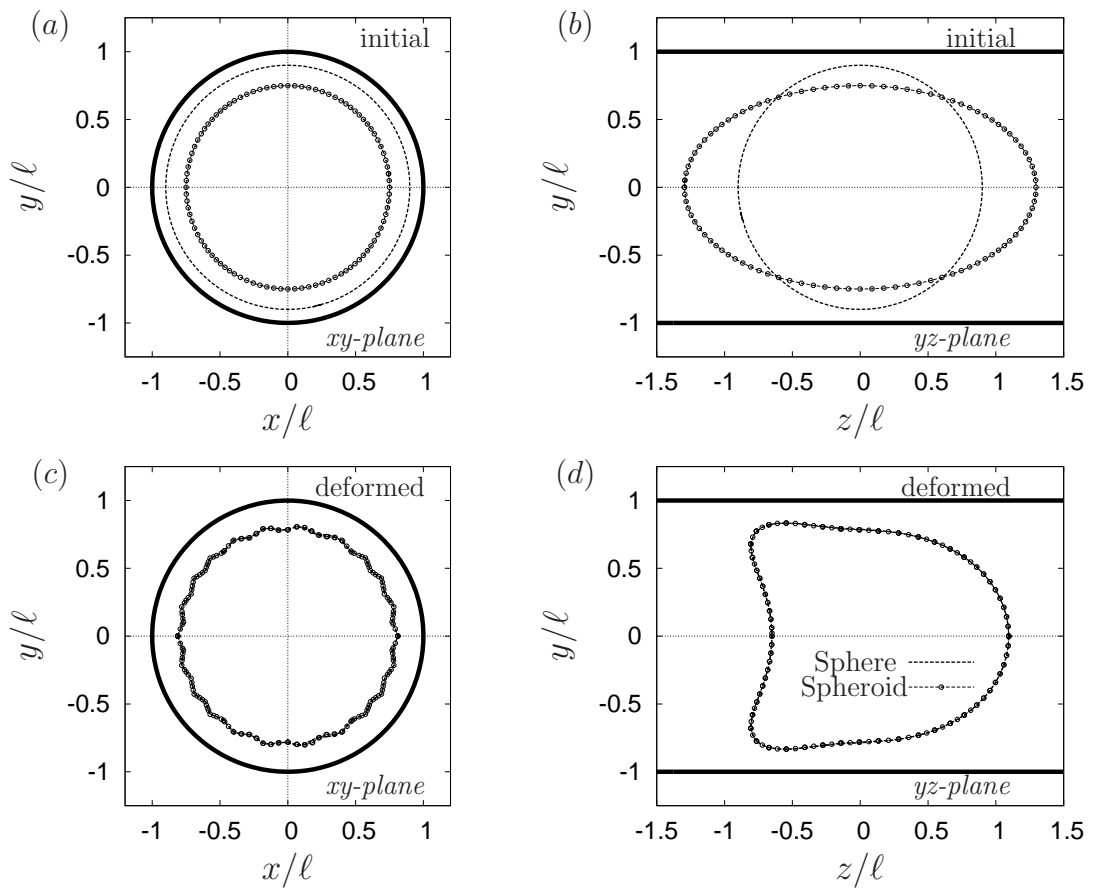
Figure 2.10: Comparisons of capsule profiles with and without pre-deformation treatment. $Ca = 0.05$, $a/\ell = 0.9$, NH membrane, cylindrical channel.

pre-deformation on the final results by comparison of the results with and without pre-deformation.

At time $t = 0$, we deform the spherical capsule to a spheroid having short axes $x/\ell = y/\ell = 0.7$ by following the method presented in section 2.2.4 (Fig. 2.10 (a) and (b)). Both the initial sphere and the pre-deformed spheroid are then deformed by the same flow strength and reach the equilibrium state. We can find that, the deformed profiles of the two cases are perfectly superimposed, as shown in Fig. 2.10 (c) and (d). It implies that the pre-deformation does not affect the final results.

2.3.3 Channel length
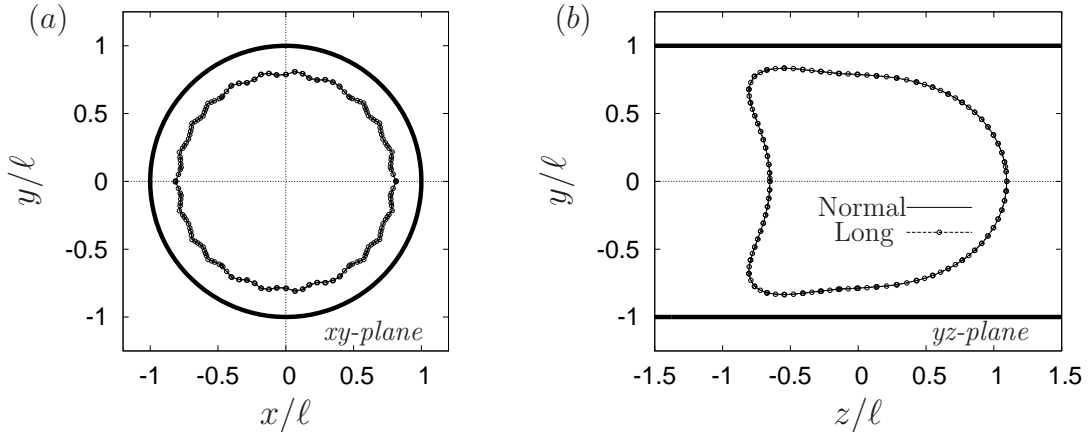
Figure 2.11: Comparisons of deformed profiles of capsules flowing inside cylindrical channels of different lengths. The "normal" channel has a total length $L = 16\ell$, while $L = 24\ell$ is for the "long" channel. $Ca = 0.05$, $a/\ell = 0.9$, NH membrane.

Since we have assumed that the capsule flow disturbance vanishes at the channel entrance and exit, it is necessary to verify that the total length of the channel mesh is long enough. We consider an initially spherical capsule with $a/\ell = 0.9$ and a NH membrane flowing inside a cylindrical channel. The capsule is discretized by a moderate mesh, which has $N_e^{(c)} = 1280$ P_2 elements and $\Delta h_C = O(0.1a)$. The cylindrical channel is discretized into three parts: the central section with a refined mesh size $\Delta h_W = O(0.14\ell)$ inside which the capsule is centered and the inlet and outlet sections with $\Delta h_W = O(0.22\ell)$, as presented in section 2.2.1. Two different channel lengths are considered:

- "Normal" channel with total length $L = 16\ell$, which has a central section with $L_c = 4\ell$ and $L_{io} = 6\ell$ for the inlet and outlet sections.

- "Long" channel with total length $L = 24\ell$, which has a central section with $L_c = 4\ell$ and $L_{io} = 10\ell$ for the inlet and outlet sections.

The deformed capsule profiles at equilibrium states are as shown in Fig. 2.11. We find that the capsule profile in the channel with "normal" length is perfectly superimposed with that in a "long" channel. It implies that the total length $L = 16\ell$ is long enough for our simulations, and it is reasonable to apply a "normal" length in the following content.

2.3.4   Capsule flow in square-section channel

The capsule flow in a square-section channel was recently considered by Kuriakose and Dimitrakopoulos [52]. The effects of a/ℓ and Ca on the capsule steady states have been studied in their work, for a pre-stressed capsule flowing in square-sectional channel. As a validation, we study the motions of a pre-stressed capsule ($\alpha_p = 0.05$) by the adapted 3D BI+FE model for comparisons with previous results in [52].

The capsule with a SK membrane ($C = 1$) flows inside a square-section channel at $Ca = 0.1$, and for size ratios $a/\ell = 0.8$, 0.9, 1.1. With the discretizations of surfaces as presented in 2.2.1, we can obtain the capsule profiles at equilibrium. These results are compared with the equivalent ones in [52], as shown in Fig. 2.12. We can find that, all the capsule profiles with different a/ℓ obtained by our model coincide well with those in [52], both on the longitudinal *yz-plane* and the cross-sectional *xy-plane*.
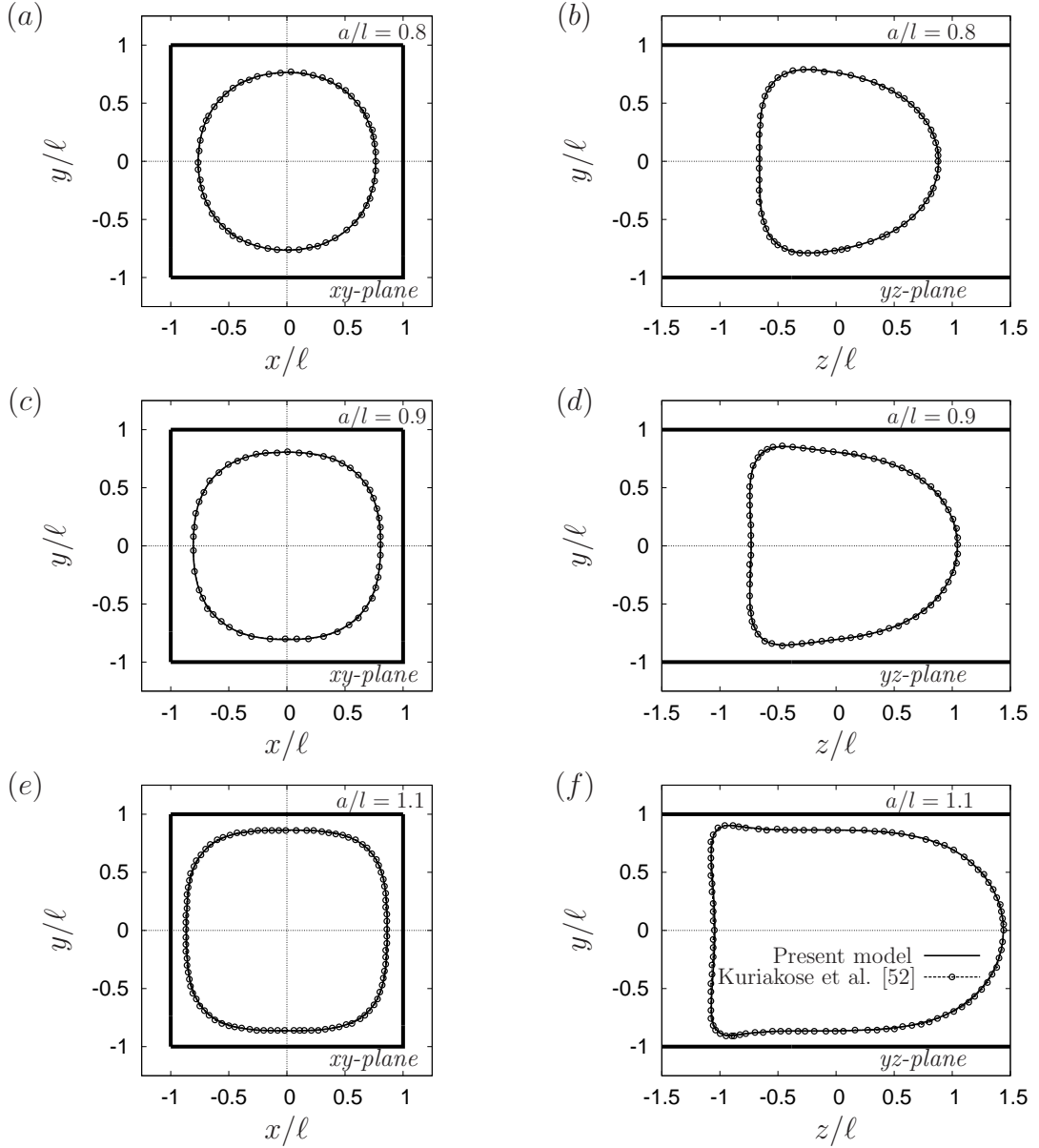
Figure 2.12: Comparisons of capsule steady profiles of our adapted BI+FE model with those of Kuriakose and Dimitrakopoulos [52]. The pre-stressed capsule ($\alpha_p = 0.05$) with SK membrane ($C = 1$) flows at $Ca = 0.1$ in a square-section channel. The size ratio a/ℓ varies from 0.8, 0.9 to 1.1, as indicated in (a), (b) and (c) for profiles in the cross-sectional *xy-plane*, while (d), (e) and (f) are profiles in the longitudinal *yz-plane*.

Chapter 3

Capsule flowing in different bounded flows

In this section, we use the adapted 3D BI+FE model to consider the motions of an initially spherical liquid-filled capsule in channels with different cross-sections, as shown in Fig. 3.1. The capsule flow in channel with circular or square cross-section has been studied in our paper published in *Journal of Fluid Mechanics*, which is included in section 3.1. The additional results of capsule flows in square or rectangular channel are then presented in section 3.2.
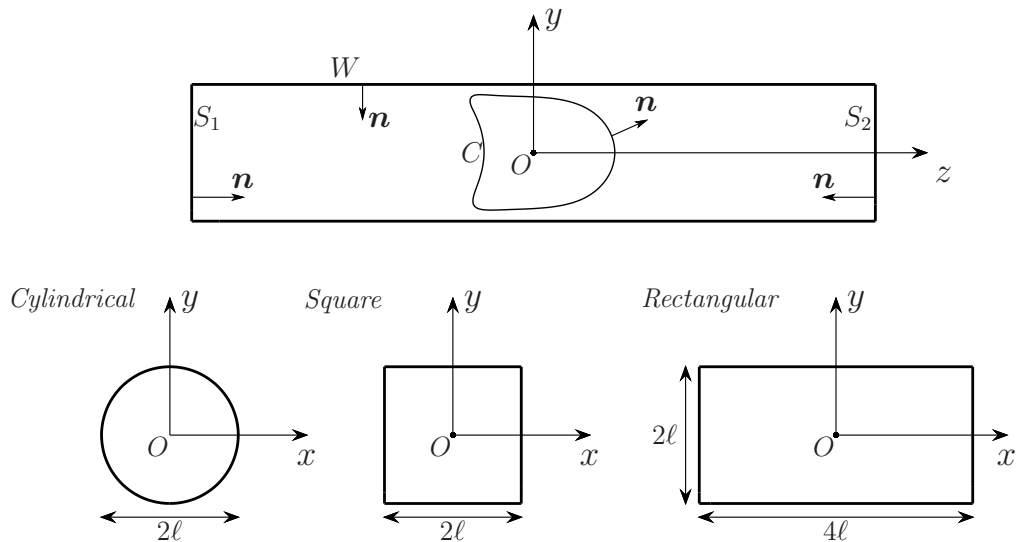
Figure 3.1: Prismatic channel with axis Oz. The cross-section is circular (radius 2ℓ), square (side width 2ℓ) or rectangular (width 4ℓ and height 2ℓ).

3.1 Capsule flow in a channel with circular or square cross-section

Flow of a spherical capsule in a pore with circular or square cross-section

X.-Q. Hu, A.-V. Salsac and D. Barthès-Biesel

Link to this article: http://journals.cambridge.org/abstract_S0022112011004629

How to cite this article:
X.-Q. Hu, A.-V. Salsac and D. Barthès-Biesel (2012). Flow of a spherical capsule in a pore with circular or square cross-section. Journal of Fluid Mechanics, 705, pp 176-194 doi:10.1017/jfm.2011.462

Request Permissions : Click here

Flow of a spherical capsule in a pore with circular or square cross-section

X.-Q. Hu, A.-V. Salsac and D. Barthès-Biesel†

Laboratoire Biomécanique et Bioingénierie (UMR CNRS 6600),
Université de Technologie de Compiègne, BP 20529, 60205 Compiègne, France

The motion and deformation of a spherical elastic capsule freely flowing in a pore of comparable dimension is studied. The thin capsule membrane has a neo-Hookean shear softening constitutive law. The three-dimensional fluid–structure interactions are modelled by coupling a boundary integral method (for the internal and external fluid motion) with a finite element method (for the membrane deformation). In a cylindrical tube with a circular cross-section, the confinement effect of the channel walls leads to compression of the capsule in the hoop direction. The membrane then tends to buckle and to fold as observed experimentally. The capsule deformation is three-dimensional but can be fairly well approximated by an axisymmetric model that ignores the folds. In a microfluidic pore with a square cross-section, the capsule deformation is fully three-dimensional. For the same size ratio and flow rate, a capsule is more deformed in a circular than in a square cross-section pore. We provide new graphs of the deformation parameters and capsule velocity as a function of flow strength and size ratio in a square section pore. We show how these graphs can be used to analyse experimental data on the deformation of artificial capsules in such channels.

Key words: biological fluid dynamics, boundary integral methods, capsule/cell dynamics

---

1. Introduction

Suspensions of microparticles are common in nature and industry. The particles may be passive with a motion and deformation governed by hydrodynamic forces or they may be self-propelled like bacteria or squirmers (Pedley & Kessler 1992; Pedley 2010). In both cases, the motion of the particle depends strongly on the interfacial mechanics and kinematics.

In the present paper, we consider a special class of passive deformable particles, capsules, that consist of a liquid drop enclosed by a deformable membrane. Capsules are common in nature (red blood cells, phospholipid vesicles) and in different applications, such as pharmacology (Cole, Cad & Benameur 2008), cosmetics (Miyazawa *et al.* 2000), the food industry (Gibbs *et al.* 1999) and biomedical engineering (Rabanel *et al.* 2009). A fine control of the membrane properties is necessary to control the capsule deformation or possible breakup (to be induced or prevented depending on the application). However, measuring the mechanical properties of the capsule membrane is difficult because the particles are small (from

† Email address for correspondence: dbb@utc.frc
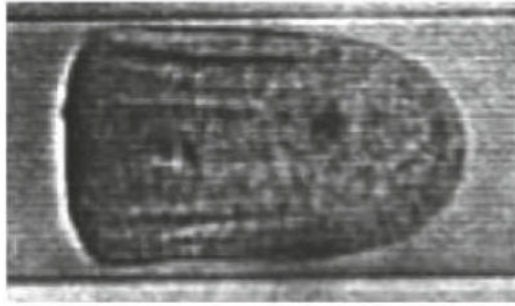
FIGURE 1. Large initially spherical capsule with a cross-linked ovalbumin membrane, flowing in a cylindrical pore (diameter 75 μm). Folds appear on the side of the capsule where the membrane is under compression. Image obtained with the experimental method of Lefebvre *et al.* (2008).

a few micrometres to a few millimetres) and fragile. Large capsules with dimensions of a few millimetres can be squeezed between two parallel plates (Carin *et al.* 2003; Risso & Carin 2004). The squeezing force and the overall capsule deformation are measured simultaneously. The interpretation of the results in terms of the membrane mechanical properties necessitates a good mechanical model of the process, as it can involve large deformations of the capsule with reversible reduction of diameter as large as 70 %. For very small capsules with dimensions of a few micrometres, it is possible to use the same measurement principle with atomic force microscopy (Fery & Weinkamer 2007). However, the method is difficult to use and must be applied to a number of capsules to get an average value for a population.

A simple way to test a population of capsules is to flow a capsule suspension in a small pore which has transversal dimensions comparable with those of the suspended capsules (Lefebvre *et al.* 2008; Chu *et al.* 2010). The hydrodynamic stresses and the constraints due to the channel walls cause large deformations of the capsules that depend on the flow strength and on the particle intrinsic physical properties such as relative size compared with the channel section and membrane constitutive behaviour. The capsule deformation, volume and velocity can be measured simultaneously by means of image analysis. A sophisticated model of the flow of a capsule in a small pore then allows us to infer the membrane mechanical properties from the experimental results. The feasibility of the method has been demonstrated for millimetre size capsules (Risso, Collé-Paillot & Zagzoule 2006; Lefebvre & Barthès-Biesel 2007) and for micrometre size capsules (Lefebvre *et al.* 2008; Chu *et al.* 2010). In both cases, the capsules were initially spherical with a membrane made of alginate cross-linked with either human serum albumin (HSA) or ovalbumin for the millimetre or micrometre size particles, respectively. The model used to analyse the experiments considered the flow of a centred spherical capsule in a cylindrical channel. The situation is thus fully axisymmetric. This allows integration of the different quantities (stress, deformation, etc.) in the azimuthal direction, so that the problem equations need only to be solved in a meridian plane. The simplification is significant.

However, observations of large capsules flowing in a cylindrical pore indicate that folds occur on the membrane as shown in figure 1. The presence of such folds means that the deformation of the membrane is not axisymmetric but three-dimensional (3D). Then the question which arises is how accurate (or inaccurate) is the axisymmetric

model used to analyse the deformation of a spherical capsule in a cylindrical pore. In order to answer this question a 3D model of this flow must be devised.

A related problem is the flow of a capsule in a microfluidic pore. When such pores are created by means of soft lithography techniques, they have a rectangular or square cross-section. The flow of an initially spherical capsule in a pore with a square or rectangular cross-section is obviously 3D. A new model is thus necessary to analyse the deformation of the capsule in terms of the membrane properties. This situation is quite interesting to study as there is an increasing interest for designing micro-encapsulation systems inside microfluidic devices (Zhang *et al.* 2006; Huang *et al.* 2007; Yeh *et al.* 2009). Creating a characterization system that can be mounted on-line on the capsule fabrication device would be very useful to test and sort the particles.

In this paper, we study the 3D flow of an initially spherical simple capsule consisting of a liquid drop enclosed by a very thin hyperelastic membrane. We assume that the flow Reynolds number is small and we adapt the numerical method of Walter *et al.* (2010) to model the fluid–structure interaction and the confining effect of the solid boundaries: the fluid motion is solved by means of the boundary integral (BI) method, while the membrane mechanics is solved by means of a finite element (FE) method. The coupling of the two methods has been shown to be very precise and to remain numerically stable even when the membrane is subjected to compressive forces causing buckling.

The method used to simulate the fluid–structure interactions occurring when a spherical capsule flows in a pore of various cross-sections is detailed in § 2. We then study the 3D evolution and deformation of a capsule in a cylindrical pore and compare the results with the ones obtained with the largely used axisymmetric numerical model in § 3. In § 4, we model the flow of a spherical capsule in a square-section pore, give new results on the effect of size ratio and flow strength and show how these can be used to analyse experimental measurements of initially spherical capsules flowing in such pores. We conclude with a critical analysis and comparison of the two set-ups.

2. Problem statement and numerical method

The flow configuration is similar to the axisymmetric case studied by Quéguiner & Barthès-Biesel (1997), Diaz & Barthès-Biesel (2002) and Lefebvre & Barthès-Biesel (2007) or to the 3D situation considered by Pozrikidis (2005), Doddi & Bagchi (2008) and Kuriakose & Dimitrakopoulos (2011); it will be only summarized in the following.

2.1. *Problem description*

The channel consists of a long prismatic tube with constant cross-section with characteristic dimension ℓ. Entrance and exit effects are neglected. As indicated in figure 2, we consider either a cylindrical tube with a circular section of radius R ($\ell = R$) or a microfluidic channel with a square section of side h ($\ell = h/2$). The channel is filled with an incompressible Newtonian liquid of viscosity μ flowing with mean velocity V and flow rate Q. The velocity field in the channel in absence of particle is denoted $\boldsymbol{v}^\infty$.

The capsule is initially spherical with radius a. It is filled with a Newtonian incompressible liquid with viscosity $\lambda\mu$ and enclosed by an infinitely thin impermeable hyperelastic membrane with surface shear elastic modulus G_s and area dilatation modulus K_s. Buoyancy forces are neglected and consequently, when the capsule is centred on Oz, it remains centred. However, if the capsule were not
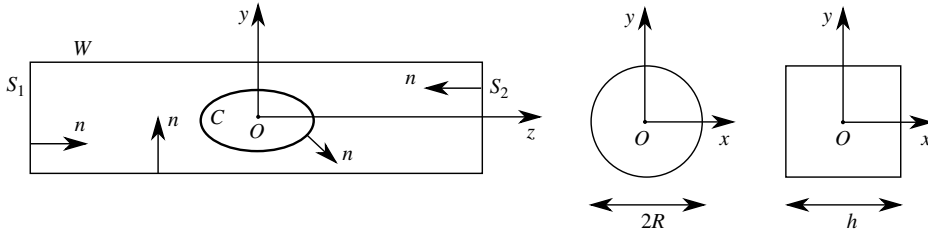
FIGURE 2. Prismatic channel with axis Oz. The cross-section is either circular with radius R or square with side h.

centred on the tube axis, it would migrate towards it (Helmy & Barthès-Biesel 1982; Pozrikidis 2005; Doddi & Bagchi 2008). We use a reference frame $Oxyz$, centred at time t on the capsule centre of mass O, Oz being along the tube axis (figure 2). We are interested in the steady deformed state of the capsule in the tube. The membrane velocity is then zero (because of the flow symmetry) and the internal fluid at rest. Consequently the internal viscosity value does not influence the steady deformation and we can take $\lambda = 1$ without loss of generality. Of course, λ has an influence on the time it takes to reach the steady state (Diaz & Barthès-Biesel 2002).

The flow Reynolds number is assumed to be very small so that the internal and external liquid motion satisfies the Stokes equations. We solve these in a domain bounded by the cross-sections S_1 at the entrance and S_2 at the exit, that are both located far enough from O for the capsule flow perturbation to vanish. The other domain boundaries are the channel wall W and the capsule surface C. The unit normal vector $\boldsymbol{n}$ to all of the boundaries points inwards the suspending liquid. We use $\boldsymbol{v}^{(\beta)}$, $\boldsymbol{\sigma}^{(\beta)}$ and $p^{(\beta)}$ to denote the velocity, stress and pressure fields in the suspending ($\beta = 1$) and internal ($\beta = 2$) liquids.

The problem boundary conditions are:

(a) no flow disturbance on S_1 and S_2 as they are far from the capsule:

$$\boldsymbol{v}^{(1)}(\boldsymbol{x}, t) \to \boldsymbol{v}^{\infty}(\boldsymbol{x}), \quad \boldsymbol{x} \in S_1 \cup S_2; \tag{2.1}$$

(b) pressure values prescribed on S_1 and S_2:

$$p^{(1)}(\boldsymbol{x}, t) = 0, \quad \boldsymbol{x} \in S_1, \tag{2.2}$$

$$p^{(1)}(\boldsymbol{x}, t) = \Delta P(t) + \Delta P^{\infty}, \quad \boldsymbol{x} \in S_2, \tag{2.3}$$

where ΔP^{∞} is the undisturbed pressure drop between S_1 and S_2 in the absence of capsule and ΔP is the additional pressure drop due to the capsule;

(c) no slip on the channel wall W:

$$\boldsymbol{v}^{(1)}(\boldsymbol{x}, t) = \boldsymbol{0}, \quad \boldsymbol{x} \in W; \tag{2.4}$$

(d) no slip on the capsule deformed surface C:

$$\boldsymbol{v}^{(1)}(\boldsymbol{x}, t) = \boldsymbol{v}^{(2)}(\boldsymbol{x}, t) = \frac{\partial}{\partial t} \boldsymbol{x}(\boldsymbol{X}, t), \quad \boldsymbol{x} \in C, \tag{2.5}$$

where $\boldsymbol{X}$ denotes the initial position of a membrane material point located at position $\boldsymbol{x}$ at time t;

(e) the load $\boldsymbol{q}$ on the membrane is due to the viscous traction jump:

$$(\boldsymbol{\sigma}^{(1)} - \boldsymbol{\sigma}^{(2)}) \cdot \boldsymbol{n} = \boldsymbol{q}, \quad \boldsymbol{x} \in C. \tag{2.6}$$

2.2. *Capsule membrane mechanics*

When the thickness of a capsule membrane is small compared with the capsule dimensions and typical radius of curvature, the membrane can be modelled as a hyperelastic surface devoid of bending resistance. A membrane material point, identified by its position X in the reference state, is displaced to the position $x(X, t)$ in the deformed state. Because the bending stiffness is neglected, the normal vector to the surface remains normal during deformation. The local deformation of the surface is measured by the Green–Lagrange strain tensor

$$e = \tfrac{1}{2}(F^{T} \cdot F - I), \tag{2.7}$$

where $F = \partial x / \partial X$. The membrane deformation can also be quantified by the principal dilatation ratios λ_1 and λ_2 in its plane which correspond to eigenvalues of e. Since the membrane is infinitely thin, elastic stresses are replaced by a Cauchy tension tensor τ corresponding to forces per unit arclength measured in the plane of the membrane.

A number of constitutive laws are available to model thin hyperelastic membranes (Barthès-Biesel, Diaz & Dhenin 2002). Different material behaviours can be described for large deformation, including the strain-softening behaviour of gelled membranes exhibiting rubber-like elasticity or the strain-hardening behaviour of membranes made of a polymerized network with strong covalent links. For conciseness, we will restrict the study to the widely used neo-Hookean (NH) law, which has been found to be the appropriate law to model the behaviour of protein-reticulated membranes (Carin *et al.* 2003; Lefebvre *et al.* 2008; Chu *et al.* 2010). The NH law describes the behaviour of an infinitely thin sheet of a 3D isotropic and incompressible material. The principal tensions are given by

$$\tau_1 = \frac{G_s}{\lambda_1 \lambda_2} \left[\lambda_1^2 - \frac{1}{(\lambda_1 \lambda_2)^2} \right] \quad \text{(likewise for } \tau_2\text{)}. \tag{2.8}$$

The hypothesis of volume incompressibility implies that area dilatation is balanced by membrane thinning and correspondingly the area dilatation modulus is $K_s = 3G_s$.

Owing to the negligible inertia of a membrane with small thickness, the membrane motion is governed by the local equilibrium equation

$$\nabla_s \cdot \tau + q = 0, \tag{2.9}$$

where q is the external load exerted by the fluids as given by (2.6) and $\nabla_s \cdot$ is the surface divergence operator in the deformed configuration.

Since the bending modulus of the membrane has been neglected, the capsule wall buckles locally in the regions where the elastic tensions are compressive (see, for example, Cerda & Mahadevan 2003, Luo & Pozrikidis 2007 and Finken & Seifert 2006). In order to study the post-buckling behaviour of the capsule, bending moments and transverse shear forces must be added to (2.9) and a constitutive equation must be postulated to relate bending moments and local deformations. It follows that the bending behaviour of a capsule is a complicated problem of shell mechanics that is not completely resolved yet.

The simplified membrane model that we use here will be appropriate to model capsules with a very low bending resistance. It will detect zones where tensions are compressive but cannot compute the post-buckling behaviour of the capsule.

2.3. *Numerical procedure*

We use the method developed by Walter *et al.* (2010) which is based on the coupling of a membrane FE method (for the capsule wall mechanics) and a boundary integral method (for the internal and external flows). We position the capsule on the channel axis and then follow the position of the material points of the membrane after the start of flow at time $t = 0$. At each time step, the deformation of the capsule may be computed from the position of the membrane material points. The elastic tension tensor $\boldsymbol{\tau}$ is then obtained from the values of the in-plane stretch ratios λ_1 and λ_2. The FE method used to solve the equilibrium of the membrane provides the load $\boldsymbol{q}$.

The Stokes equations are recast in boundary integral form for the 3D motion of the internal and external fluids. In the case of a capsule in a tube and for $\lambda = 1$, the velocity $\boldsymbol{v}(\boldsymbol{x})$ of any point $\boldsymbol{x}$ in the fluid domain is given by Pozrikidis (2005)

$$\boldsymbol{v}(\boldsymbol{x}) = \boldsymbol{v}^\infty(\boldsymbol{x}) - \frac{1}{8\pi\mu} \left[\int_C \boldsymbol{J}(\boldsymbol{r}) \cdot \boldsymbol{q} \, \mathrm{d}S(\boldsymbol{y}) + \int_W \boldsymbol{J}(\boldsymbol{r}) \cdot \boldsymbol{f} \, \mathrm{d}S(\boldsymbol{y}) \right. $$
$$\left. - \Delta P \int_{S_2} \boldsymbol{J}(\boldsymbol{r}) \cdot \boldsymbol{n} \, \mathrm{d}S(\boldsymbol{y}) \right], \tag{2.10}$$

where $\boldsymbol{f}$ is the disturbance wall friction due to the capsule and $\boldsymbol{r} = \boldsymbol{y} - \boldsymbol{x}$. The Green kernel is defined by

$$\boldsymbol{J}(\boldsymbol{r}) = \frac{1}{r}\boldsymbol{I} + \frac{\boldsymbol{r} \otimes \boldsymbol{r}}{r^3}, \tag{2.11}$$

where $r = \|\boldsymbol{r}\|$ and $\boldsymbol{I}$ is the identity tensor.

Applying the reciprocal theorem to the flow without capsule $(\boldsymbol{v}^\infty, \boldsymbol{\sigma}^\infty)$ and to the flow with the capsule $(\boldsymbol{v}^{(1)}, \boldsymbol{\sigma}^{(1)})$ in the domain bounded by $S_1 \cup S_2 \cup W \cup C$, we find

$$\int_C [\boldsymbol{\sigma}^{(1)} \cdot \boldsymbol{n}] \cdot \boldsymbol{v}^\infty \, \mathrm{d}S - (\Delta P + \Delta P^\infty)Q = \int_C [\boldsymbol{\sigma}^\infty \cdot \boldsymbol{n}] \cdot \boldsymbol{v}^{(1)} \, \mathrm{d}S - \Delta P^\infty Q, \tag{2.12}$$

where we have used the facts that the flow rate Q is the same with and without the capsule and that the velocity is zero on W. Now, we apply the reciprocal theorem to $(\boldsymbol{v}^\infty, \boldsymbol{\sigma}^\infty)$ and to $(\boldsymbol{v}^{(2)}, \boldsymbol{\sigma}^{(2)})$ in the domain bounded by C

$$\int_C [\boldsymbol{\sigma}^{(2)} \cdot \boldsymbol{n}] \cdot \boldsymbol{v}^\infty \, \mathrm{d}S = \int_C [\boldsymbol{\sigma}^\infty \cdot \boldsymbol{n}] \cdot \boldsymbol{v}^{(2)} \, \mathrm{d}S. \tag{2.13}$$

We subtract (2.12) and (2.13) and use (2.5) and (2.6) to find that the additional pressure drop is simply given by

$$\Delta P = \frac{1}{Q} \int_C \boldsymbol{v}^\infty(\boldsymbol{x}) \cdot \boldsymbol{q} \, \mathrm{d}S(\boldsymbol{y}). \tag{2.14}$$

Once the value of the pressure disturbance ΔP is known, the application of (2.10) to $\boldsymbol{x} \in W$

$$0 = \int_C \boldsymbol{J}(\boldsymbol{r}) \cdot \boldsymbol{q} \, \mathrm{d}S(\boldsymbol{y}) + \int_W \boldsymbol{J}(\boldsymbol{r}) \cdot \boldsymbol{f} \, \mathrm{d}S(\boldsymbol{y}) - \Delta P \int_{S_2} \boldsymbol{J}(\boldsymbol{r}) \cdot \boldsymbol{n} \, \mathrm{d}S(\boldsymbol{y}) \tag{2.15}$$

yields an implicit equation for $\boldsymbol{f}$ which is solved numerically. Applying then (2.10) to $\boldsymbol{x} \in C$, we obtain the new velocity $\boldsymbol{v}(\boldsymbol{x}, t)$ of the membrane points from which we deduce the velocity $\boldsymbol{v}(O, t)$ of the centre of mass. The no-slip equation (2.5) is first
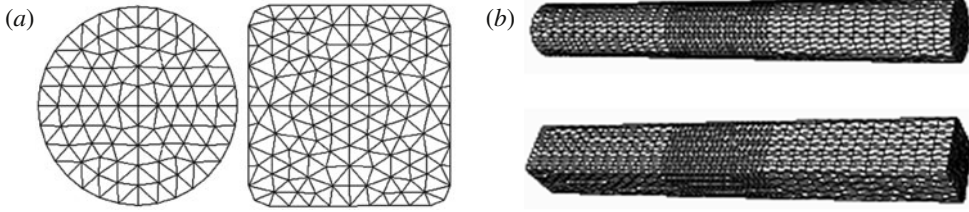
FIGURE 3. (*a*) Meshes of the circular and square cross-sections; (*b*) meshes of the prismatic tubes.

modified to keep the centre of mass fixed at point O

$$\boldsymbol{v}^{(1)}(\boldsymbol{x}, t) - \boldsymbol{v}(O, t) = \frac{\partial}{\partial t}\boldsymbol{x}(X, t), \quad \boldsymbol{x} \in C. \tag{2.16}$$

Equation (2.16) is then time-integrated to provide the new position of the membrane points. The procedure is repeated until a steady state is reached (typically when the surface of the capsule varies by less than $5 \times 10^{-4} \times (4\pi a^2)$ over a non-dimensional time $Vt/\ell = 1$).

2.4. *Discretization*

The surface of the capsule is discretized using triangular curved P_2 elements, which have six nodes (one at each vertex and at the middle of each side) and are associated with quadratic shape functions. The mesh of the initial spherical capsule is obtained by first inscribing an icosahedron (regular polyhedron with 20 triangular faces) in the sphere and subdividing the elements sequentially until the desired number of elements is reached (Ramanujan & Pozrikidis 1998; Walter *et al.* 2010). For all of the 3D computations, we use a capsule mesh with 1280 elements and 2562 nodes, which correspond to a characteristic mesh size $\Delta h_C = O(0.1a)$.

The tube mesh is generated using Modulef (INRIA Rocquencourt, France). We first generate the two-dimensional geometry of the tube cross-section with the desired shape (circular or square in the present case). The circular or square cross-sections are meshed with unstructured triangular elements having a mesh size $\Delta h_S = O(0.14\ell)$. The corners of the rectangular cross-section have been rounded with an arccircle (radius Δh_S) in order to avoid corner effects when solving for the flow (figure 3*a*). As shown in figure 3(*b*), the central section of the tube (of length 4ℓ) has a more refined mesh ($\Delta h_W = O(0.14\ell)$) than the inlet and outlet tube sections ($\Delta h_W = O(0.22\ell)$), each of length 6ℓ. Altogether, the mesh comprises 1505 nodes and 2976 elements for the cylindrical tube and 1905 nodes and 3768 elements for the rectangular tube.

The numerical method is conditionally stable if the time step satisfies a similar condition to that found for the unbounded case (Walter *et al.* 2010)

$$\frac{V}{\ell}\Delta t < O\left(\frac{\Delta h_C}{\ell}Ca\right), \tag{2.17}$$

where Δt is the time step. All of the results shown hereafter have been obtained with a time step $V\Delta t/\ell = 5 \times 10^{-5}$. We have checked the influence of the wall and exit mesh size using a mesh size twice as small as that described above and have not found any significant influence on the capsule deformed profile. This confirms that the error on the capsule shape is mainly determined by the capsule mesh size and is then $O(\Delta h_C^4)$ as shown by Walter *et al.* (2010).

2.5. *Case $a/\ell > 1$*

When the capsule initial size is larger than the channel cross-dimension, we pre-deform the capsule into an spheroid that fits inside the pore. Correspondingly, a point initially located at X, Y, Z on the capsule surface is displaced to x, y, z, such that

$$z = k_1 Z, \quad y = k_2 Y, \quad x = k_2 X, \qquad (2.18)$$

with $k_2^2 k_1 = 1$, in view of the volume conservation requirement. We choose k_2 such that $y/\ell = 0.9$, in order to leave a reasonably thick liquid film between the membrane and the channel wall. The resulting elastic tensions in the membrane and the load q exerted on the fluid are computed by means of the FE method. The capsule deformation is then followed in time as explained above. We have verified that the amount of pre-deformation does not influence the results: exactly the same results have been obtained with another value of k_2 such that the capsule is pre-deformed to $y/\ell = 0.8$.

2.6. *Presentation of the results*

The model parameters are the capillary number $Ca = \mu V / G_s$ which measures the ratio between the viscous and elastic forces and the size ratio a/ℓ. The deformed profile intersections with the yz- or xz-planes are determined. These correspond to what is typically observed experimentally for a capsule flowing in a pore. The principal tensions along the profile are also computed in order to detect the presence of compression zones. The position of a point M on the profile is determined by the angle $\theta = (e_z, \mathbf{OM})$.

3. Flow of a capsule in a cylindrical pore

We now consider a pore with a circular cross-section of radius R. The undisturbed velocity is

$$v^\infty = 2V[1 - (x^2 + y^2)/R^2]e_z. \qquad (3.1)$$

If we assume the capsule profile to remain axisymmetric, the flow is also axisymmetric and it is possible to integrate (2.9), (2.10), (2.14) and (2.15) analytically in the azimuthal direction. The surface integrals on C and W then become line integrals along the meridian curves of the corresponding surfaces, while the integral on S_2 is taken along a radius of the section (Pozrikidis 1992; Quéguiner & Barthès-Biesel 1997; Diaz & Barthès-Biesel 2002; Lefebvre & Barthès-Biesel 2007). With this procedure, a negative azimuthal tension may compress part of the capsule membrane without creating any numerical instability. However, it must be recognized that the solution thus obtained is mechanically unstable: the membrane should actually buckle in these regions as observed experimentally (figure 1).

In the axisymmetric model we use, the tube entrance is shaped as an hyperboloid (Quéguiner & Barthès-Biesel 1997; Diaz & Barthès-Biesel 2002; Lefebvre & Barthès-Biesel 2007). An undeformed capsule is positioned in the entrance section, far enough from the cylindrical part of the pore to fit in, and we follow the entrance process into the cylindrical pore until a steady state is reached. Charts of the capsule deformation parameters as functions of the size ratio, capillary number and osmotic pre-swelling may be found in Lefebvre & Barthès-Biesel (2007), Lefebvre *et al.* (2008) and Chu *et al.* (2010).

3.1. *Three-dimensional effects on capsule deformation*

We compare the results obtained with the 3D computation, where no specific assumption on the problem symmetry is made *a priori*, with those provided by the
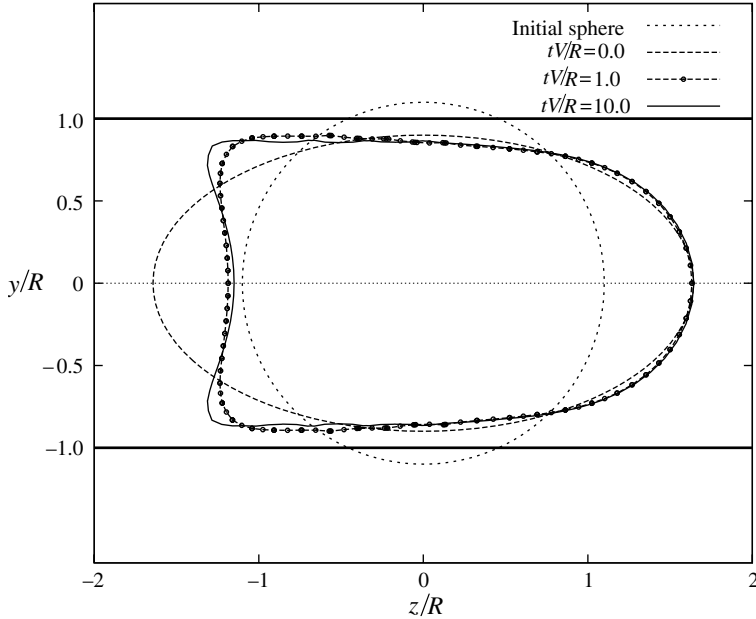
FIGURE 4. Successive profiles of a capsule of aspect ratio $a/R = 1.1$, subjected to a capillary number $Ca = 0.05$. The initially spherical capsule being larger than the pore is deformed into an ellipsoid at dimensionless time $tV/R = 0$. The capsule is then left free to adapt its shape to the flow. It has a steady parachute shape at $tV/R = 10$.

axisymmetric model. For the 3D computation, we first stretch the capsule as explained in §2.5 and then let it reach an equilibrium, if any. Results are presented for a typical case where $a/R = 1.1$ and $Ca = 0.05$. It is a deliberate choice to show results for a large capsule aspect ratio, as the larger the aspect ratio the larger the capsule deformation for a given capillary number. The successive capsule profiles are shown in figure 4. We note that the largest shape change occurs at the rear where the curvature evolves from a positive to a negative value. At steady state, the internal liquid being at rest, the internal pressure is constant. In order to adapt to the viscous pressure drop occurring in the external liquid, the membrane curvature must be larger at the front than at the rear, thus leading to slug or parachute shapes of the capsule.

As shown in figure 5(a), the meridional axisymmetric and 3D profiles are almost superimposed in plane Oyz. The cross-profiles in plane $z = 0$ are also superimposed notwithstanding small oscillations of the 3D profile about the mean circular profile predicted by the axisymmetric model (figure 5b).

The axisymmetric computation shows that the principal tension τ_2 in the azimuthal direction is negative, and thus compressive, on part of the membrane (for $\theta/\pi \in \pm[0.35; 0.8]$ or $z \in [-1.16; 0.43]$) as shown in figure 6. This means that in the grey area of figure 5(a), the membrane is undergoing compression and will tend to buckle. In this area where the membrane is undergoing compression and where there is no bending resistance to regulate the process, the 3D model leads to values of τ_2 which oscillate about zero with a wavelength of the order of twice the grid spacing. The membrane undergoes a numerical buckling which mimics the actual one qualitatively only. We have checked that the wavelength of the oscillation decreases by a factor two when the number of elements is doubled.
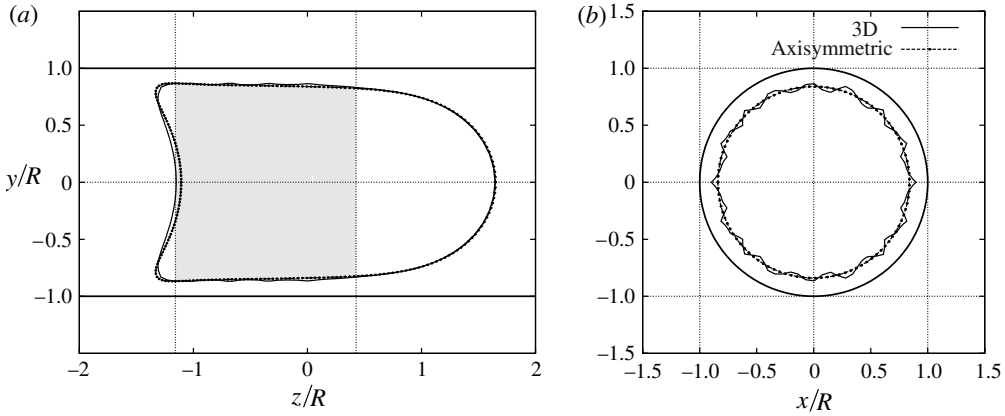
FIGURE 5. Comparison of the capsule profiles at steady state obtained with the axisymmetric and 3D computations for $a/R = 1.1$ and $Ca = 0.05$. (*a*) Profiles in the *yz*-plane: the zone where compression occurs is shaded in grey; (*b*) cross-profiles in the *xy*-plane for which $z = 0$: the oscillation of the 3D profile indicate a tendency towards folding.
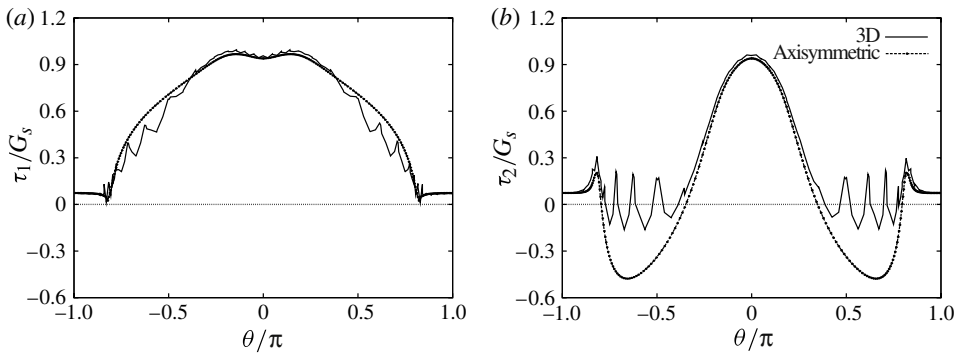
FIGURE 6. Comparison of the principal tensions in the *yz*-plane at steady state obtained with the axisymmetric and 3D computations for $a/R = 1.1$ and $Ca = 0.05$. The principal tensions are plotted as a function of position θ/π along the profile. Tension τ_1 is directed along the profile, while τ_2 is perpendicular to the plane and thus in the hoop direction.

As a consequence of the compression, the 3D cross-profile in plane $z = 0$ undergoes small oscillations about the mean circular profile predicted by the axisymmetric model (figure 5*b*). These oscillations correspond qualitatively to the folds that are observed experimentally and whose wavelength is obviously regulated by the membrane thickness and bending stiffness. The values of the principal tension τ_1 along a 'meridian' curve in the Oyz plane also oscillate about the axisymmetric value.

Finally we note that on the part of the membrane where no compression occurs (i.e. about the front of the capsule), the tensions values are superimposed. In particular, the maxima of τ_1 are identical with the two computations. This indicates that the axisymmetric and 3D model would both lead to the same mechanical failure criterion.

In conclusion, we find that, for large capsule aspect ratios, there is significant lateral compression on the capsule membrane leading to folds similar to those observed experimentally and shown in figure 1. For smaller values of the size ratio a/R, we

obtain the same qualitative results, namely that the axisymmetric and 3D profiles are almost identical. The fit is optimal for small aspect ratios and capillary numbers, as the capsule is then devoid of compression zones around its surface at steady state.

The axisymmetric model predicts that for a given size ratio, there exists a higher bound on the capillary number Ca_{max} for which it is possible to reach a steady equilibrium state (Chu *et al.* 2010). For flow rates such that $Ca > Ca_{max}$ the capsule undergoes continuous extension. This phenomenon is similar to that which occurs in elongational flow for NH membranes and which is due to the strain-softening behaviour of the NH law (Barthès-Biesel 2011). The 3D computation also finds an upper bound on the values of Ca for which it is not possible to obtain a steady state. The values of Ca_{max} are about 10 % larger with the 3D model than with the axisymmetric model. This difference may be attributed to the numerical technique and to the discretization of the membrane. As a consequence, the exact 3D value of Ca_{max} is immaterial, and the upper bounds given by Chu *et al.* (2010) can be used for practical purposes.

3.2. *Conclusion for the capsule flow in a cylindrical pore*

The axisymmetric model has been used by Lefebvre *et al.* (2008) and Chu *et al.* (2010) to analyse experiments on microcapsules flowing in a cylindrical pore of known radius R. The procedure is based on the contour extraction of the deformed profile from which the capsule volume and size ratio a/R are computed. A database of computed deformed profiles obtained for different values of a/R and Ca is then searched to find the same deformation characteristics as the experimentally observed profile. This leads to a set of values of Ca from which G_s is inferred (for details, see Lefebvre *et al.* 2008 and Chu *et al.* 2010).

We have shown that although the capsule membrane tends to fold, the axisymmetric profiles represent a very good approximation of the actual 3D profiles. It follows that the characterization procedure based on the axisymmetric model is sound. As regards the elastic tensions though, the axisymmetric model can only be used to evaluate their maximum values and determine the zones where buckling will occur. This is an important result, as it is much easier and faster to use an axisymmetric representation than a full 3D representation. For example, for $Ca = 0.05$ and $a/l = 0.9$, the computation of a time interval $tV/\ell = 1$ takes 1 h for the axisymmetric case using one core of a 128-core cluster and 5.7 h for the 3D case using 8 cores (of course, those times are given for a usual mesh size, but increase with the mesh refinement).

4. Flow in a square cross-section pore

The uniform axial velocity distribution $\boldsymbol{v}^\infty = v^\infty(x, y)\boldsymbol{e}_z$ in a duct with a square cross-section is given in a number of textbooks (e.g. Pozrikidis 1997)

$$v^\infty(x, y) = \frac{\pi V \sum \left[\dfrac{1}{n^3} - \dfrac{\cosh n\pi x/h}{n^3 \cosh n\pi/2}\right] \sin n\pi(y/h + 1/2)}{2\left[\dfrac{\pi^4}{96} - \sum \dfrac{\tanh n\pi/2}{n^5\pi/2}\right]} \quad n = 1, 3, \ldots \quad (4.1)$$

where the sums are taken over odd values of n. When applying the no-slip condition (2.15), we set to zero the velocity of the node point located in the middle of the rounded corner (figure 3), where its actual value is $0.05V$ or $0.02V$ for the standard or refined boundary mesh, respectively. As the change in wall mesh size has a negligible influence on the capsule profile, we consider that this corner rounding leads to a
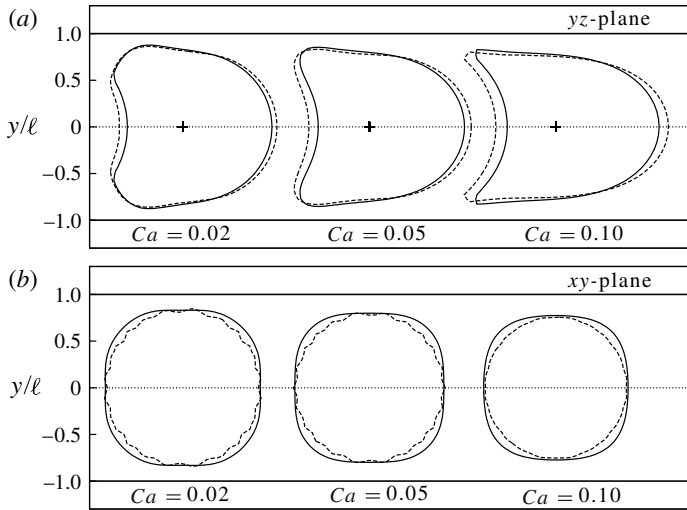
FIGURE 7. Steady capsule profiles in a square channel (full line) and in a cylindrical tube (dashed line) for $a/\ell = 0.9$. (*a*) Profiles in the *yz*-plane, with the cross on the axis indicating the position of the centre of mass $z = 0$; (*b*) cross-profiles in the *xy*-plane for which $z = 0$.

negligible error. In the following, we analyse the influence of the confinement induced by a square tube as compared to a cylindrical tube. For brevity, we use the notation 'circular capsule' or 'square capsule' for the capsule in the circular or square section pore, respectively. The results shown for the circular capsule are obtained with the three-dimensional model.

4.1. *Case $a/\ell < 1$*

We first consider the case $2a/h = 0.9$ where the capsule is only slightly smaller than the channel. The longitudinal and cross-profiles are shown in figure 7 and compared with the three-dimensional profiles obtained in a cylindrical tube for the same values of *Ca* and a/R. We note that for small capillary numbers (e.g. $Ca = 0.02$) the deformation is small and the deformed profiles in the two channels are almost superimposed. When *Ca* increases, the circular capsule having less room to deform is more elongated than the square capsule, which can expand in the corners of the channel as shown in figure 7(*b*). As a consequence, the deformed profile of a square capsule is not axisymmetric. Another consequence is that the tension τ_1 along the profile is larger for the circular than for the square capsule as shown in figure 8(*a*). Furthermore, the cross-section of the square capsule is not under compression (τ_2 is positive everywhere), whereas the circular capsule is compressed and tends to buckle as discussed in the previous section (figure 8*b*). For $Ca = 0.1$, one could be under the wrong impression that the circular capsule does not buckle: actually, it buckles for negative values of *z*.

4.2. *Case $a/\ell \geqslant 1$*

We now turn to large capsules that must be pre-deformed. The longitudinal and cross-profiles are shown in figure 9 for the case $a/\ell = 1.1$. First we note that for low flow strength ($Ca \leqslant 0.05$), the square capsule membrane is compressed near the wall but is extended in the corners. By contrast, the circular capsule is compressed all around as evidenced by the cross-profiles (figure 9*b*) and by the corresponding oscillations
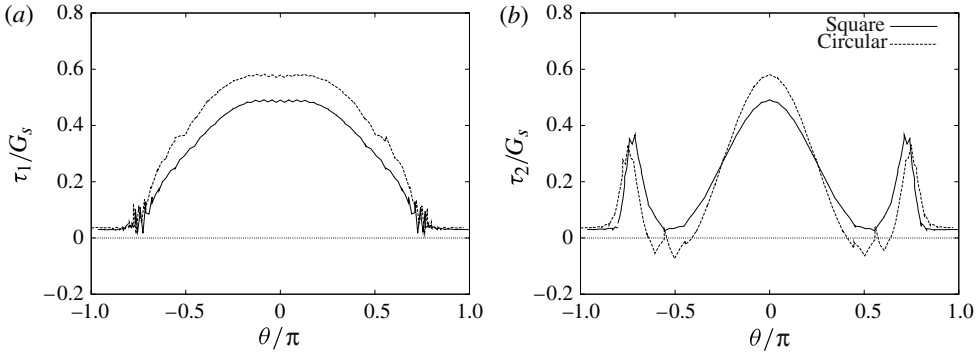
FIGURE 8. Principal tensions in the yz-plane at steady state for a capsule ($a/\ell = 0.9$) flowing in a cylindrical or square channel at $Ca = 0.05$. The principal tensions are plotted as a function of position θ/π on the profile.
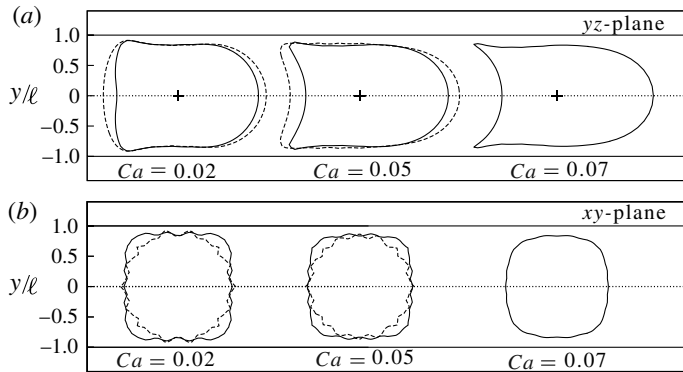

FIGURE 9. Steady capsule profiles in a square channel (full line) and in a cylindrical tube (dashed line) for $a/\ell = 1.1$. (*a*) Profiles in the yz-plane, with the cross on the axis indicating the position of the centre of mass $z = 0$; (*b*) cross-profiles in the xy-plane for which $z = 0$.

of tension τ_2 (figure 10*b*). As the flow strength increases, the capsule is stretched along the pore axis, the surface area increases and the negative tensions disappear. The circular capsule being more deformed than the square one, the tension level in the membrane is higher as shown in figure 10.

For $a/\ell = 1.1$ and high flow strength ($Ca = 0.08$–0.09), the capsule also undergoes continuous elongation and no steady equilibrium state can be reached. We note again that the value of Ca_{max} for which this phenomenon occurs is larger in the square section pore than in the circular section pore. Indeed, in the cylindrical pore, a flow strength $Ca = 0.07$ exceeds Ca_{max}, which is the reason why no circular capsule profile is shown in figure 9 for $Ca = 0.07$.

4.3. *Effect of Ca and a/l*

From an experimental point of view, it is convenient to characterize the capsule deformation with the maximum profile length L and the axial length L_a along the Oz axis. These two parameters are equal for slug shapes, whereas $L_a < L$ for parachute shapes. The lengths L and L_a are plotted as a function of Ca in figure 11(*a*) for the circular and square pores. We find that, to obtain the same elongation L in the
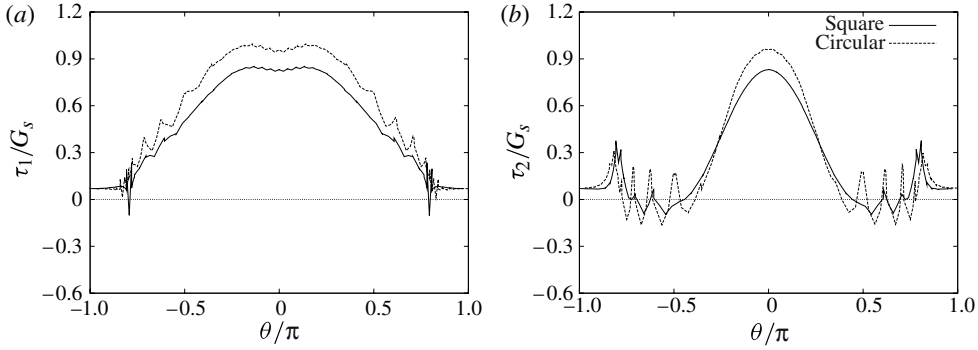
FIGURE 10. Principal tensions in the *yz*-plane at steady state for a capsule ($a/\ell = 1.1$) flowing in a cylindrical or square channel at $Ca = 0.05$.
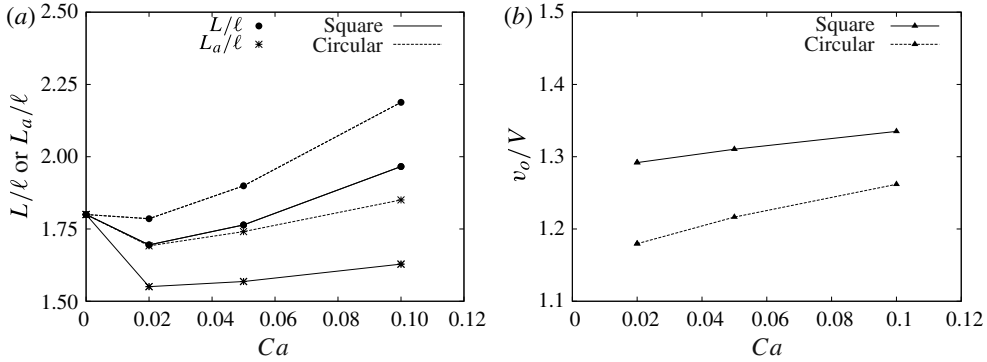
FIGURE 11. Capsule maximum length L, axial length L_a and centre of mass velocity v_O for a capsule ($a/\ell = 0.9$) at steady state flowing in a cylindrical or square channel. For the same value of Ca, the capsule is more deformed in the cylindrical than in the square pore and travels at a slower speed.

two pores, the value of Ca in the square pore must be about 60 % higher than that in the circular pore. The values of $L - L_a$ are the same for the two types of pores, as can also be observed from figure 7. The steady velocity of the capsule centre of mass v_O is plotted in figure 11(*b*). It is 10 % higher in the square than in the circular pore. The explanation for this larger velocity is outlined by Lefebvre *et al.* (2008) and summarized here in the limiting case where the film is thin. When a capsule has the same deformed axial profile in a circular or square channel, it is subjected to the same pressure drop ΔP_c along its length L (because the front and back curvatures are the same). This pressure drop is related to the viscous loss in the lubrication film. For example for the circular tube, a force balance yields

$$\Delta P_c \pi \ell^2 = 2\pi \ell L \mu v_{Ocyl} / \overline{h}_{cyl} \qquad (4.2)$$

where $\overline{h}_{cyl}$ is the mean film thickness. The same expression is found for the mean film thickness $\overline{h}_{sq}$ in terms of the capsule velocity v_{Osq} in the square channel. It follows that

$$\frac{v_{Osq}}{v_{Ocyl}} = \frac{\overline{h}_{sq}}{\overline{h}_{cyl}}. \qquad (4.3)$$
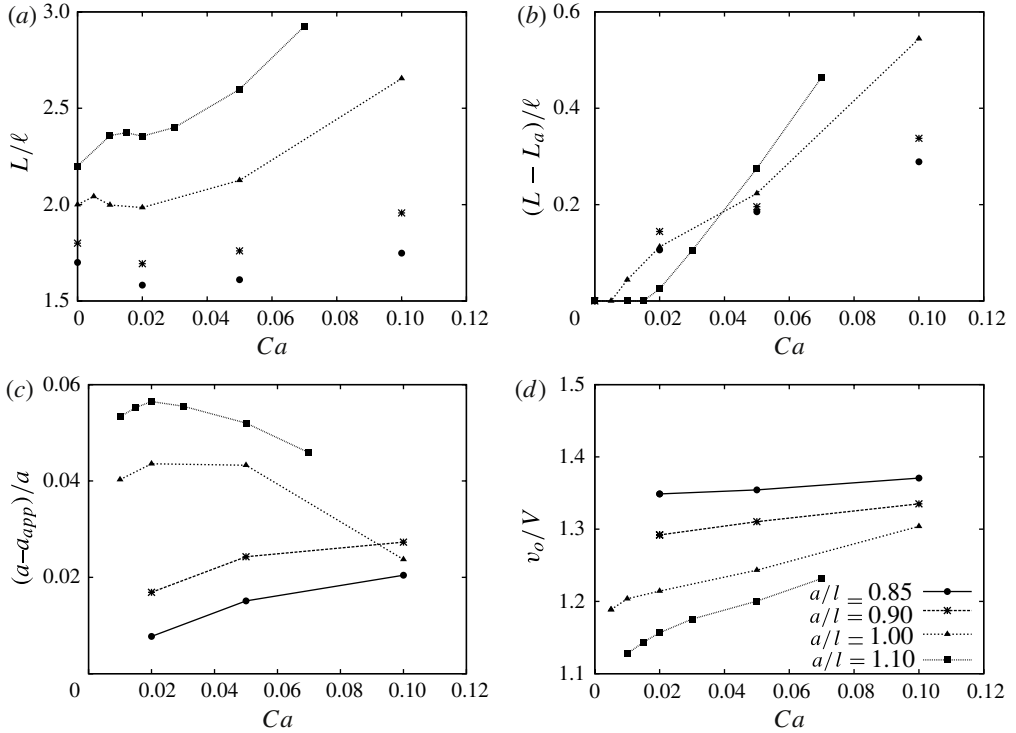
FIGURE 12. Plots of the values of the capsule total length L, parachute depth $L - L_a$, difference between axisymmetric and actual capsule radius and centre of mass velocity v_O. These graphs are useful to analyse experimental data on capsules flowing in square section pores.

There are two limiting shapes of the capsule cross-section in a square channel that correspond to a given axial profile. If the cross-section of the capsule is square, the mean thickness is constant $\bar{h}_{sq} = \bar{h}_{cyl}$. If it is circular with radius $\ell - \bar{h}_{cyl}$, $\bar{h}_{sq} > \bar{h}_{cyl}$ due to the contribution of the corners. From (4.3), the velocity v_{Osq} is then equal or larger than v_{Ocyl}. The numerical model finds that the capsule cross-section is square with rounded corners (figures 7b and 9b), which indicates that v_{Osq} must be larger than v_{Ocyl}.

In conclusion, larger flow rates must be used in the square pore than in the cylindrical pore to get the same deformation. This may cause some experimental difficulties as the capsule will move faster and its detection will be more difficult.

The combined effects of flow strength and aspect ratio are summarized in figure 12. We note that for aspect ratios less than unity, the capsule is first compressed in the axial direction when the capillary number is small (e.g. $Ca \leqslant 0.02$) as can be surmised from the initial decrease of L. Then the stretching effect of the viscous forces elongates the capsule. When $a/\ell \leqslant 0.95$–0.97 the capsule takes a parachute shape for all values of Ca. For larger aspect ratios (e.g. $a/\ell \geqslant 1$), the parachute appears only when Ca exceeds a critical value Ca_c. When $Ca < Ca_c$, the capsule has a slug shape and $(L - L_a)/\ell = 0$. The capsule moves faster than the average fluid velocity as it is centred on the channel. All of these phenomena are qualitatively similar to those observed for the flow of capsules in cylindrical tubes (Lefebvre & Barthès-Biesel 2007; Lefebvre *et al.* 2008) irrespective of the membrane constitutive law.
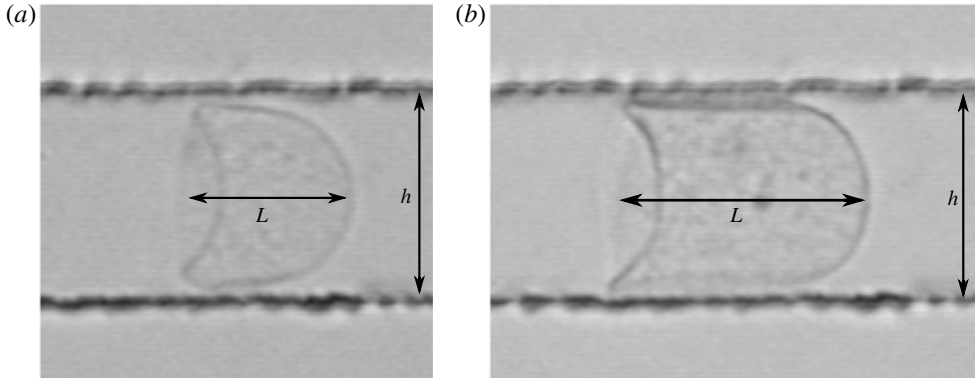
FIGURE 13. Flow of initially spherical capsules with a cross-linked ovalbumin membrane in a 50 μm × 50 μm microfluidic channel; (*a*) $a_{app}/\ell = 0.85$, $v_O = 6.6$ mm s^{-1}; (*b*) $a_{app}/\ell = 1.05$, $v_O = 4.5$ mm s^{-1}.

These plots are necessary to analyse the flow of capsules in a square section pore and to infer a value for the membrane elastic modulus from the capsule deformation and velocity. In a typical microfluidic device, only the capsule deformed profile in one plane (e.g. the *yz*-plane) can be observed. It is thus difficult to evaluate the volume (or the initial radius) of the capsule. A way to do it is to rotate the profile in the *yz*-plane about the pore axis as if the capsule were axisymmetric and to deduce an approximate initial radius a_{app}, from the pseudo-axisymmetric volume. The model allows us to compute the error between a_{app} and the real value a. Indeed, the model yields a steady deformed profile for a capsule of known volume. If we rotate the deformed profile in the *yz*-plane about the channel axis and compute the volume of the axisymmetric shape thus obtained, we can infer the numerical value of a_{app} and compare it to a. This is done in figure 12(*c*) where we find that a_{app} always underestimates a. This is of course due to the propensity of the square capsule to occupy the tube corners for large aspect ratios: the capsule volume that expands in the corners is not taken into account during the rotation procedure described above.

4.4. *Comparison with experimental results*

Measurement of the flow of artificial capsules in cylindrical tubes and in square section microfluidic pores have been conducted by Lefebvre *et al.* (2008). The capsules are initially spherical and have a cross-linked ovalbumin membrane. They are suspended in a 100 % glycerin solution (viscosity $\mu = 1$ Pa) and flowed through microchannels with a cross-section comparable to the capsule, $a/\ell = O(1)$. The capsule deformed profile are recorded with a high-speed camera and their velocity is measured. Lefebvre *et al.* (2008) used a NH model to describe the membrane elasticity and found a shear modulus value $G_s = 0.07 \pm 0.01$ N m^{-1} from the cylindrical pore measurements.

We outline briefly how the results of §4.3 can be used to evaluate the mechanical properties of capsules. In figure 13, we show deformed capsules obtained in a microfluidic channel with a 50 μm × 50 μm cross-section under the same experimental conditions as Lefebvre *et al.* (2008). We first note the qualitative similarity between the profiles of figures 7(*a*) and 13(*a*) on the one hand, and of figures 9(*a*) and 13(*b*) on the other. For the small capsule, we find $a_{app}/\ell = 0.85$ or $a/\ell = 0.86 - 0.87$; $L/\ell = 1.7$. From figure 12(*a,d*), we find $Ca \approx 0.06$ and $v_O/V = 1.33$. It follows that

the membrane shear modulus is

$$G_s = \frac{6.6 \times 10^{-3}}{1.33 \times 0.06} = 0.08 \text{ N m}^{-1}. \tag{4.4}$$

The same reasoning for the large capsule yields $a_{app}/\ell = 1.05$ or $a/\ell = 1.1 - 1.09$; $L/\ell = 2.5$, $Ca \approx 0.04$ and $v_O/V = 1.19$, leading to

$$G_s = \frac{4.5 \times 10^{-3}}{1.19 \times 0.04} = 0.09 \text{ N m}^{-1}. \tag{4.5}$$

These values are in good agreement with those of Lefebvre *et al.* (2008), which is very encouraging. A full analysis of the precision and discriminating power of the method is left for a future study.

5. Conclusion

We have shown in this paper how 3D effects affect the flow of capsules in pores with cross-dimensions comparable with the capsule diameter. The confinement effect due to the channel walls compresses the capsule in the direction perpendicular to the pore axis. This leads to compression of the membrane and a tendency towards buckling that has been observed experimentally. The flow of a capsule in a small pore is thus a 3D process even when the pore and the capsule share the same revolution axis.

These 3D effects have been specifically studied and we have shown that in a cylindrical tube with a circular cross-section, the 3D capsule deformation is well approximated by an axisymmetric simple model. This is an interesting and important result as it is much easier and faster to use an axisymmetric numerical model rather than a full 3D model.

In the case of microfluidic pores with square cross-section the 3D aspect of the problem cannot be simplified. We have thus conducted a novel study of the flow of spherical capsules in pores as a function of capillary number and aspect ratio. A comparison between the numerical model and some experimental measurements of capsules flowing in square section microfluidic pores shows that it is possible to evaluate the capsule membrane elastic modulus. This is a very interesting result as it opens the way to the design of on-line microfluidic measuring systems that can evaluate the mechanical properties of capsules.

One of the drawbacks of this study is the lack of bending resistance of the capsule membrane leading to non-physical numerical folds in the regions where the membrane is undergoing compression. Accounting properly for the bending and post-buckling behaviour of the capsule membrane is a formidable problem of shell mechanics. The reason being that the capsule is subjected to large deformation, large membrane forces and that the bending effect becomes preponderant only on parts of the wall. It is clear that a very fine mesh of the capsule wall would be necessary if we were to reproduce the folds with any precision. This would increase very significantly the computer time. The interesting question which arises at this point is how necessary is it to account for bending forces? If the capsule wall has a highly anisotropic structure (e.g. the red blood cell wall which consists of a lipid bilayer lined by a protein network), it is clear that bending forces can be fairly large as compared to membrane shear forces and must be accounted for. For artificial capsules with a wall which consists of a thin layer of a 3D isotropic material (e.g. a gelled membrane reinforced by a polymer network), the bending resistance is directly related to the ratio of the membrane thickness to

the capsule radius. For thickness ratios less than 10 %, it is generally admitted that bending effects will be very small compared with the membrane forces. It is thus quite possible that ignoring bending forces and adding a small uncontrolled numerical resistance (due to discretization) leads to a fairly good approximate model that can be used to analyse the motion of real artificial capsules.

Acknowledgements

REFERENCES

BARTHÈS-BIESEL, D. 2011 Modelling the motion of capsules in flow. *Curr. Opin. Colloid Interface Sci.* **16**, 3–12.

BARTHÈS-BIESEL, D., DIAZ, A. & DHENIN, E. 2002 Effect of constitutive laws for two dimensional membranes on flow-induced capsule deformation. *J. Fluid Mech.* **460**, 211–222.

CARIN, M., BARTHÈS-BIESEL, D., EDWARDS-LÉVY, F., POSTEL, C. & ANDREI, D. 2003 Compression of biocompatible liquid-filled HSA-alginate capsules: determination of the membrane mechanical properties. *Biotechnol. Bioengng* **82**, 207–212.

CERDA, E. & MAHADEVAN, L. 2003 Geometry and physics of wrinkling. *Phys. Rev. Lett.* **90** (7), 074302.

CHU, T. X., SALSAC, A.-V., LECLERC, E., BARTHÈS-BIESEL, D., WURTZ, H. & EDWARDS-LÉVY, F. 2010 Comparison between measurements of elasticity and free amino group content of ovalbumin microcapsule membranes: discrimination of the cross-linking degree. *J. Colloid Interface Sci.* **355**, 81–88.

COLE, E. T., CAD, D. & BENAMEUR, H. 2008 Challenges and opportunities in the encapsulation of liquid and semi-solid formulations into capsules for oral administration. *Adv. Drug Deliv. Rev.* **60**, 747–756.

DIAZ, A. & BARTHÈS-BIESEL, D. 2002 Entrance of a bioartificial capsule in a pore. *Comput. Model. Engng Sci.* **3** (3), 321–337.

DODDI, S. K. & BAGCHI, P. 2008 Lateral migration of a capsule in a plane Poiseuille flow in a channel. *Intl J. Multiphase Flow* **34** (10), 966–986.

FERY, A. & WEINKAMER, R. 2007 Mechanical properties of micro- and nanocapsules: single capsule measurements. *Polymer* **48**, 7221–7235.

FINKEN, R. & SEIFERT, U. 2006 Wrinkling of microcapsules in shear flow. *J. Phys.: Condens. Matter* **18** (15), L185–L191.

GIBBS, B. F., KERMASHA, S., ALLI, I. & MULLIGAN, C. N. 1999 Encapsulation in the food industry: a review. *Intl J. Food Sci. Nutr.* **50**, 213–224.

HELMY, A. & BARTHÈS-BIESEL, D. 1982 Migration of a spherical capsule freely suspended in an unbounded parabolic flow. *J. Méc. Théor. Appl.* **1** (5), 859–880.

HUANG, K. S., LIU, M. K., WU, C. H., YEN, Y. T. & LIN, Y. C. 2007 Calcium alginate microcapsule generation on a microfluidic system fabricated using the optical disk process. *J. Micromech. Microengng* **17**, 1428–1434.

KURIAKOSE, S. & DIMITRAKOPOULOS, P. 2011 Motion of an elastic capsule in a square microfluidic channel. *Phys. Rev.* E **84**, 011906.

LEFEBVRE, Y. & BARTHÈS-BIESEL, D. 2007 Motion of a capsule in a cylindrical tube: effect of membrane pre-stress. *J. Fluid Mech.* **589**, 157–181.

LEFEBVRE, Y., LECLERC, E., BARTHÈS-BIESEL, D., WALTER, J. & EDWARDS-LEVY, F. 2008 Flow of artificial microcapsules in microfluidic channels: a method for determining the elastic properties of the membrane. *Phys. Fluids* **20** (12), 123102.

LUO, H. & POZRIKIDIS, C. 2007 Buckling of a pre-compressed or pre-stretched membrane. *Intl J. Solids Struct.* **44**, 8074–8085.

MIYAZAWA, K., YAJIMA, I., KANEDA, I. & YANAKI, T. 2000 Preparation of a new soft capsule for cosmetics. *J. Cosmet. Sci.* **51**, 239–252.

PEDLEY, T. J. 2010 Instability of uniform micro-organism suspensions revisited. *J. Fluid Mech.* **647**, 335–359.

PEDLEY, T. J. & KESSLER, J. O. 1992 Hydrodynamic phenomena in suspensions of swimming microorganisms. *Annu. Rev. Fluid Mech.* **24**, 313–358.

POZRIKIDIS, C. 1992 *Boundary Integral and Singularity Methods for Linearized Viscous Flow*. Cambridge University Press.

POZRIKIDIS, C. 1997 *Introduction to Theoretical and Computational Fluid Dynamics*. Oxford University Press.

POZRIKIDIS, C. 2005 Numerical simulation of cell motion in tube flow. *Ann. Biomed. Engng* **33**, 165–178.

QUÉGUINER, C. & BARTHÈS-BIESEL, D. 1997 Axisymmetric motion of capsules through cylindrical channels. *J. Fluid Mech.* **348**, 349–376.

RABANEL, J. M., BANQUY, X., ZOUAOUI, H., MOKHTAR, M. & HILDGEN, P. 2009 Progress technology in microencapsulation methods for cell therapy. *Biotechnol. Prog.* **25**, 946–963.

RAMANUJAN, S. & POZRIKIDIS, C. 1998 Deformation of liquid capsules enclosed by elastic membranes in simple shear flow: large deformations and the effect of capsule viscosity. *J. Fluid Mech.* **361**, 117–143.

RISSO, F. & CARIN, M. 2004 Compression of a capsule: mechanical laws of membranes with negligible bending stiffness. *Phys. Rev.* E **69**, 061601–061608.

RISSO, F., COLLÉ-PAILLOT, F. & ZAGZOULE, M. 2006 Experimental investigation of a bioartificial capsule flowing in a narrow tube. *J. Fluid Mech.* **547**, 149–173.

WALTER, J., SALSAC, A.-V., BARTHÈS-BIESEL, D. & LE TALLEC, P. 2010 Coupling of finite element and boundary integral methods for a capsule in a Stokes flow. *Intl J. Numer. Meth. Engng* **83**, 829–850.

YEH, C. H., ZHAO, Q., LEE, S. J. & LIN, Y. C. 2009 Using a *t*-junction microfluidic chip for monodisperse calcium alginate microparticles and encapsulation of nanoparticles. *Sensors Actuators* **151**, 231–236.

ZHANG, H., TUMARKIN, E., PEERANI, R., NIE, Z., SULLAN, R. M. A., WALKER, G. C. & KUMACHEVA, E. 2006 Microfluidic production of biopolymer microcapsules with controlled morphology. *J. Am. Chem. Soc.* **128**, 12205–12210.

3.2   Capsule flow in a channel with square or rectangular cross-section

In this section, we consider an initially spherical capsule flowing in a channel with square or rectangular cross-section. For the rectangular one, the width and height of the section are $W = 4\ell$ and $h = 2\ell$ respectively, while the side width for square channel is 2ℓ, as shown in Fig. 3.1. The capsule is centred on the channel axis, and the surfaces of the channel and capsule are discretized as presented in section 2.2.1. All the following results are obtained by 3D computations. We first study the capsule flow in a rectangular channel, which is compared with the results in a square channel. Finally the global effect of the channel geometry on the capsule flow is presented.
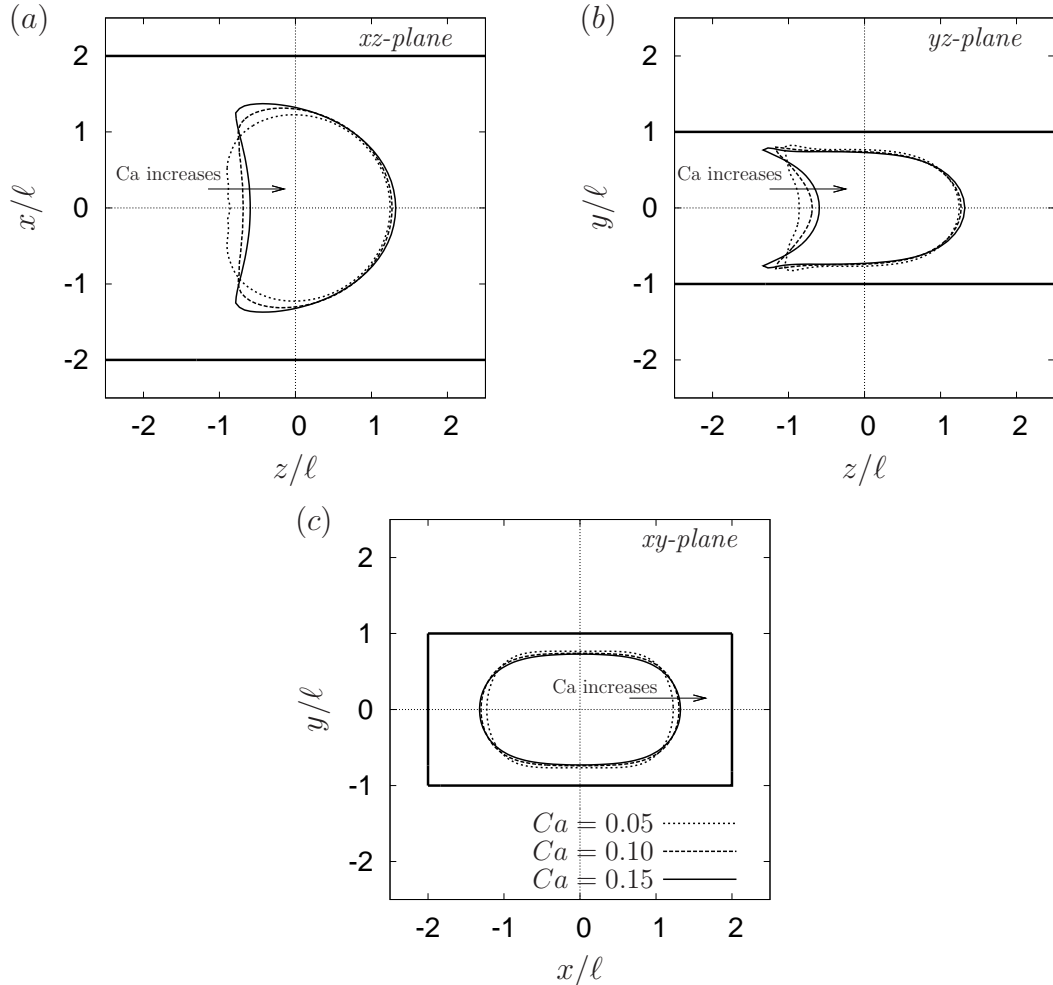
Figure 3.2: The effect of Ca on the profiles of a capsule flowing in a channel with rectangular cross-section. Ca increases from 0.05, 0.10 to 0.15. $a/\ell = 1.1$, NH membrane.

As shown in Fig. 3.2, the capsule with $a/\ell = 1.1$ and a NH membrane flows inside a channel with rectangular cross-section. The flow strength Ca varies from 0.05, 0.10 to 0.15. We determine the deformed capsule profiles in the xy-, xz- and yz- planes for $z_o = 0$. Since the channel width is twice the height, the centred capsule is less confined in the x- direction and it expands in this direction as Ca increases, as shown in Fig. 3.2(a) and (c). In the y- direction, the boundary walls confine the capsule and the parachute depth becomes larger with the increase of Ca.
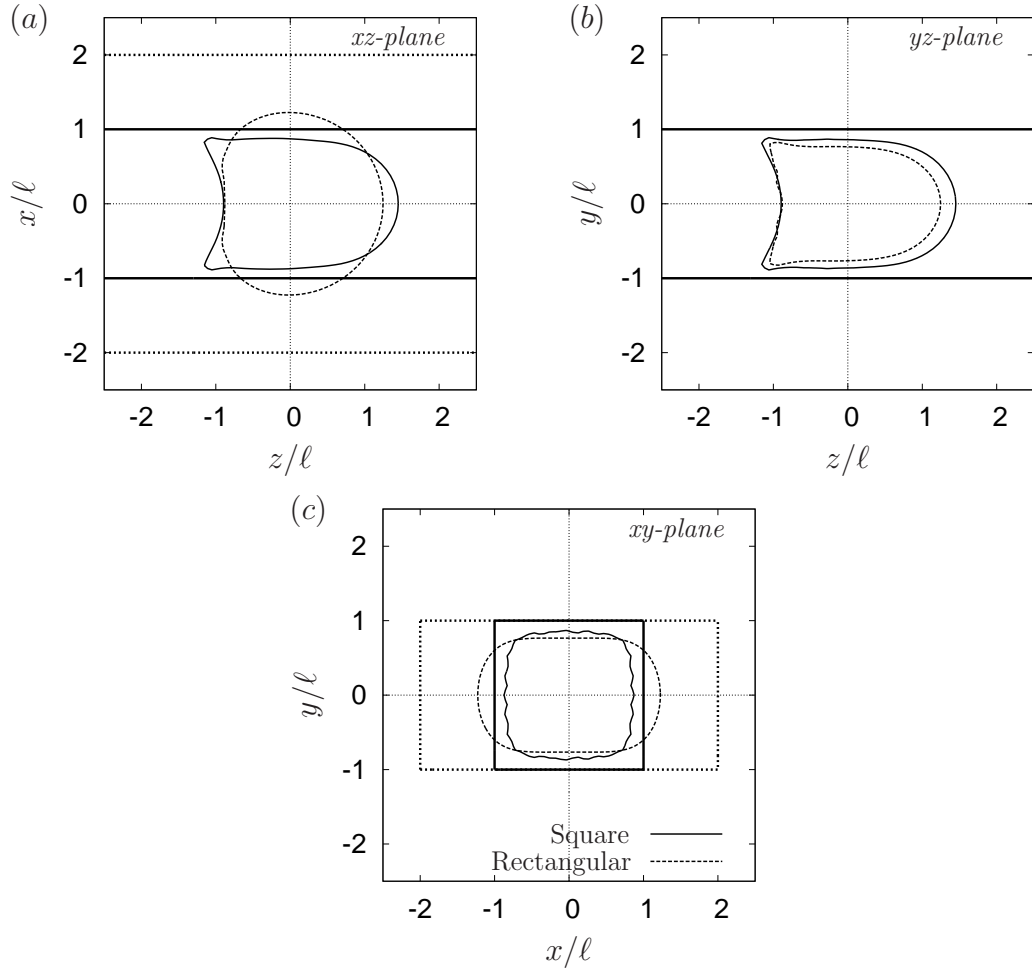
Figure 3.3: Comparisons of the deformed profiles of a capsule flowing in square and rectangular channels. $Ca = 0.05$, $a/\ell = 1.1$, NH membrane. The solid line is for the square sectional channel, and the dashed line for the rectangular one.

The flow of a capsule with $a/\ell = 1.1$ and a NH membrane inside a square or a rectangular channel at $Ca = 0.05$ is shown in Fig. 3.3. Since the rectangular channel is twice as wide as the square one, the capsule profile in a rectangular channel is wider in the x- direction but shorter in the z- direction. Since less boundary confinement is

imposed on the capsule in the rectangular than in the square channel, the capsule in a square channel presents more wrinkles than that in a rectangular one.
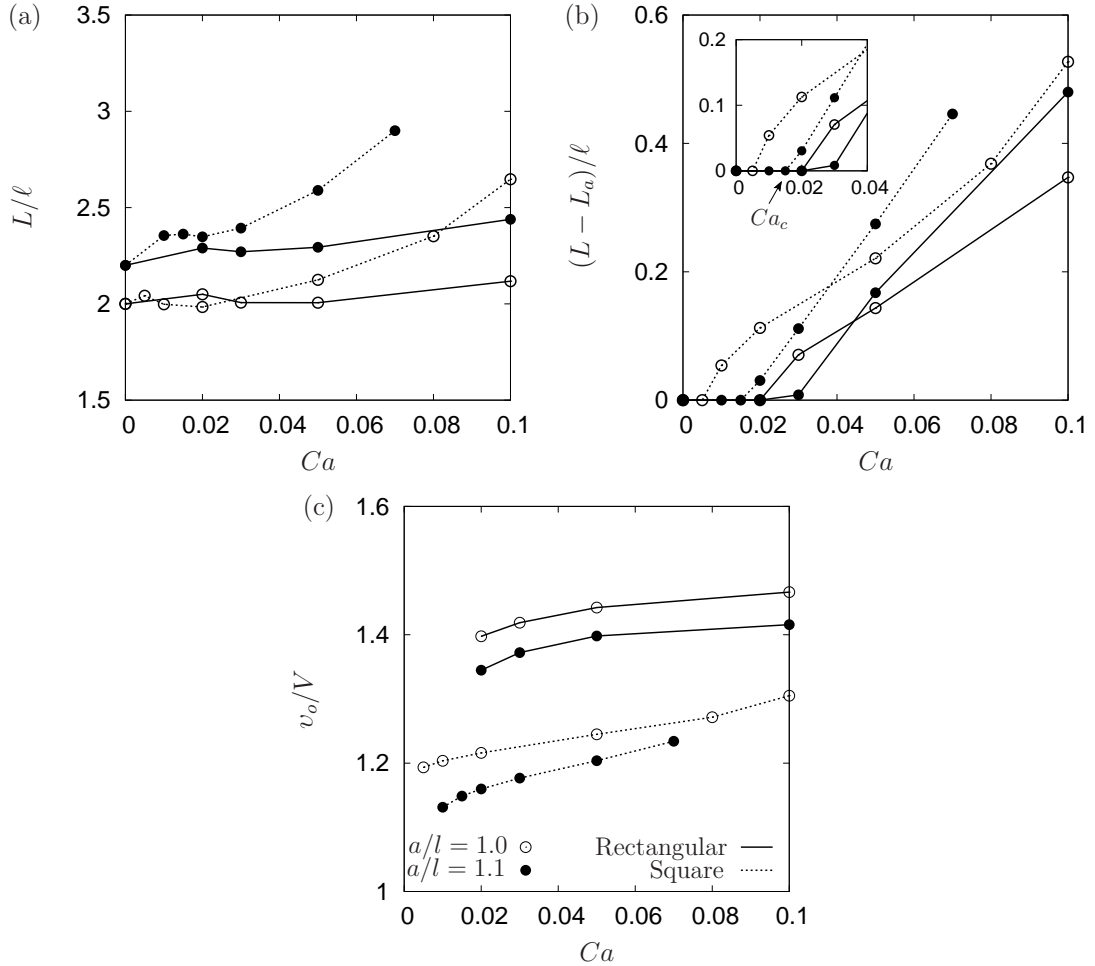
Figure 3.4: Effect of Ca, a/ℓ and channel cross-sectional geometry on the capsule total length L/ℓ, parachute shape $(L - L_a)/\ell$ and center of mass velocity υ_o/V.

The maximum length L/ℓ and the parachute depth $(L - L_a)/\ell$ in the *yz-plane* are shown in Fig. 3.4. The parachute forms when the capillary number exceeds the critical capillary number Ca_c. The value of Ca_c is less for a capsule in a square channel than for one in a rectangular channel. When $Ca > Ca_c$, both L/ℓ and $(L - L_a)/\ell$ increase faster with Ca for the capsule flowing in a square channel than for the one in a rectangular channel. This is due to the larger cross-sectional space of the rectangular channel, which allows the capsule to expand more in the x- direction than in a square channel. The overall effect of the size ratio is to increase the deformation for a given flow strength. It is of interest to notice that the capsule in a rectangular channel has a higher relative velocity than in a square channel. This is due again to the larger

sectional space of rectangular channel, which allows the capsule to stay in the central area of the channel where the velocity is higher than in the area near the boundary.

Chapter 4

Comparison with experiments

In this section, we propose to use the numerical results in a channel with square cross-section to characterize the membrane mechanical properties of a population of artificial microcapsules with a cross-linked ovalbumin membrane. Since the rational choice of membrane constitutive laws is important for a successful measurement, the effect of membrane constitutive laws is also discussed. This is included in our paper submitted to *Physical Review E* recently, which is presented in section 4.1. The additional results including the tensions on profiles of capsule flowing in square channel and the effect of pre-stress are presented in section 4.2.

4.1 Characterization of membrane properties of capsules flowing in a square-section microfluidic channel: effects of the membrane constitutive law

Characterization of membrane properties of capsules flowing in a square-section microfluidic channel: effects of the membrane constitutive law

X.-Q. Hu,[1] B. Sévénié,[1] A.-V. Salsac,[1, a)] E. Leclerc,[1] and D. Barthès-Biesel[1]

Laboratoire de Biomécanique et Bioingénierie (UMR CNRS 7338),

Université de Technologie de Compiègne, BP 20529, 60205 Compiègne,

France

(Dated: 19 April 2013)

A microfluidic method is presented to measure the elastic membrane properties of a population of microcapsules with diameter of order 60 μm. The technique consists of flowing a suspension of capsules enclosed by a polymerized ovalbumin membrane through a square-section microfluidic channel with cross dimension comparable with the capsule mean diameter. The deformed profile and the velocity of a given capsule are recorded. A full mechanical model of the motion and deformation of an initially spherical capsule flowing inside a square-section channel is designed for different flow strengths, confinement ratios and membrane constitutive laws. The experimental deformed profiles are analyzed with the numerical model. This allows us to find the ratio between the viscous and elastic forces, and thus the shear elastic modulus of the membrane. We show that the ovalbumin membrane tends to have a strain-softening behavior under the conditions studied here.

---

a)Electronic mail: a.salsac@utc.fr

I. INTRODUCTION

Capsules, which are liquid droplets enclosed by a thin elastic membrane, are widely found in nature (red blood cells, eggs) and in cosmetic, food or pharmaceutical industry[1]. The deformable membrane that separates the internal and external liquids prevents the diffusion and degradation of the internal substance and controls its release. The motion and deformation of flowing capsules depend on the mechanical properties of membrane. The characterization of these properties is thus essential for the design of artificial capsules, but it is a challenging task when the capsules have a small size of order a few tens of micrometers. Artificial capsules are usually obtained through interfacial polymerization of a liquid droplet and are thus spherical. In the following, we consider only initially spherical artificial capsules with radius a.

A method that is widely used for relatively large millimeter-size capsules is to compress them between two rigid parallel plates and measure simultaneously the plate separation and compression force. Using an appropriate mechanical model of the set-up, the membrane constitutive law can be deduced[2]. Subjecting capsules to simple shear flow[3] or to centrifugal flow fields[4] are two other possible ways to measure the membrane properties. However, it is difficult to reach large mechanical stresses in such devices.

For micrometer-size capsules, poking the membrane with an atomic force microscope[5] or sucking part of it in a micropipette[6,7] are classical techniques to measure the membrane mechanical properties. Both require skillful micro-manipulations and are not suitable for screening large populations of microcapsules quickly. Recently, a new method has been proposed to measure the membrane properties of a capsule population. It consists of flowing a capsule suspension into a cylindrical glass capillary tube with radius comparable to that of the capsules[8,9]. Hydrodynamic forces and boundary confinement lead to a large deformation of the capsules, which can take either a parachute or a slug shape. The membrane mechanical properties are then determined by analyzing the experimental results with a numerical model of the set-up. This method, applied to 50 μm diameter capsules with a cross-linked ovalbumin membrane, allows to correlate the membrane mechanical properties to the cross-linking degree and to the physicochemical conditions of the capsule fabrication[9]. It is, however, not easy to connect the syringe pump to the 50 μm diameter capillary tube, where the measurement is performed. A double tube was designed, but it leads to fairly

large pressure drops.

The rapidly growing microfluidic technologies allow to design simpler devices, where the capillary tubes are easily connected to the feeding system. Owing to fabrication constraints, the tubes usually have a square or rectangular cross-section. We thus investigate the feasibility of using a microfluidic channel with a square cross-section to measure the membrane properties of a population of capsules suspended in a viscous fluid. The channel has a side length 2ℓ of the same order of magnitude as the capsule mean diameter $2a$. We will see that the initially spherical capsule can be subjected to significant deformations depending on the flow velocity and size ratio a/ℓ between the capsule and the channel. This means that it will be possible to discriminate which type of constitutive law the membrane follows.

The analysis of the experiments requires a specific numerical model of the flow of a capsule in a square pore. Kuriakose & Dimitrakopoulos[10] recently designed such a model, based on the use of spectral elements, for capsules enclosed in a shear-hardening membrane described by a Skalak et al. law[11]. However, the capsules had to be pre-inflated and thus pre-stressed in order to prevent buckling instabilities. If the pre-stress has a negligible influence when the capsule is highly deformed, it changes the results significantly at small and moderate deformation[12]. We use instead the three-dimensional fluid-structure interaction scheme initially proposed for capsules freely suspended in unbounded flows[13] and recently adapted for capsules flowing in circular and square-section channels[14]. This numerical technique consists of coupling the boundary integral method for the fluid flows with a finite element method for the membrane deformation. The advantages of this model are two-fold: the capsules do not need to be pre-stressed and large confinement ratios can be considered. In Hu et al.[14], we have studied in detail the case of capsules with a strain-softening neo-Hookean membrane. We now extend the results to the case of capsules with a strain-hardening law in order to analyze the experimental results with either law.

We first present the experimental method used to measure the deformation of artificial capsules flowing in a square-section capillary tube. We then explain briefly the mechanical model which represents the experiments and give global results on the capsule deformation and kinematics as functions of the suspending flow strength and confinement. Finally we show how the method can be used to estimate the shear elastic modulus of the membrane of a capsule population and discuss the limits of the method.

II. MATERIALS AND METHODS

A. Capsule fabrication

Microcapsules are prepared using an interfacial cross-linking method[15]. Briefly, a 10% (w/v) ovalbumin (Sigma) solution is prepared using a phosphate buffer with $pH = 5$. The solution is emulsified in cyclohexane (SDF) containing 2% (w/v) sorbitan trioleate (Sigma) at a stirring speed of 1550 rpm. A 2.5% (w/v) solution of terephthaloyl chloride (Acros) in chloroform:cyclohexane (1:4 v/v) is then added to the emulsion and the cross-linking reaction is allowed to develop for 5 min. The reaction is stopped by diluting the reaction medium with cyclohexane. The microcapsules are separated from the organic phase by centrifugation and washed successively with cyclohexane, with water containing 2% (w/v) polysorbate (Sigma) and finally washed three times with pure water in which the samples are kept. The resulting capsules have a mean diameter of 62 ± 14 μm.

B. Microfluidic system fabrication

Straight 5 mm long square-section channels are fabricated by molding liquid poly-dimethylsiloxane (PDMS) onto a silicon master, baking and peeling it off[16,17]. The channels are then closed bonding them onto a glass lamella by air plasma (Plasma cleaner, Harrick). The width of the channel is estimated to be $W = 57.5 \pm 1.5$ μm using a line graduated rule to estimate the pixel to μm conversion factor. The depth of the channel, measured on the silicon mold, is $h = 52 \pm 1$ μm. As the channel cross-section is not perfectly square, we define the length 2ℓ as the side of the ideal square cross-section channel having the same cross-area

$$\ell = \frac{\sqrt{W \times h}}{2} = 27.4 \pm 0.5 \, \mu m. \tag{1}$$

C. Capsule suspension preparation

A volume of 40 μL of ovalbumin microcapsule sediment is suspended in 1.8 mL of glycerin (100%, VWR BDH Prolabo), which leads to a 2.2% (w/v) capsule suspension. After mixing by successive pumping in-and-out of a syringe, the suspension is left to rest for 10 min at the room temperature of 23°C to allow the inner water to be replaced by the outer glycerin

4

by osmotic exchange. This process does not seem to damage the capsules, which recover a spherical shape within minutes. As a consequence, we consider that there is no osmotic difference between the internal and external liquids and that the membrane is thus not pre-stressed. The viscosity μ of the suspending fluid strongly depends on temperature and water content[18]. Former measurements of the suspension[9] provided a viscosity of $\mu = 0.7$ Pa.s at 23°C . We assume this value to be the viscosity of the fluid carrier and thus neglect the influence of the small amount of capsules present in the suspension.

D.   Experimental setup

We fill a 1 mL glass syringe (Fortuna Optima) with the suspension and take care that no air bubble remains in either the syringe or the silicon connection tube to minimize throughput variations. The suspension is injected into the microfluidic system by means of a syringe pump (KDS100, KD Scientific) at different flow rates. The deformation and velocity of a capsule is observed with a ×40 magnification transmission microscope (Leica DM IL LED), which is connected to a high resolution high-speed camera (FASTCAM SA3 Photron) through a ×1 C-mount (Leica). The microscope is focused on the channel center plane. The capsule profile is observed along the channel axis and width W. The images are recorded at 1000 frames per second, with an exposure time of 0.2 ms and an observation field 1024×256 pixels. The calibration scale is 0.425 μm/pixel. The observation field is far enough from the entrance (about 3 mm i.e. 100ℓ) to consider that the capsule has reached a steady state. From two successive images, we measure the capsule velocity v_o, which varies between 1 and 10 mm/s, depending on the size of the capsule and the flow rate.

E.   Capsule profile extraction and experimental measurements

Fig. 1(a) shows an experimental image of a capsule flowing in a 2ℓ square channel. Because automatic image extraction is difficult with this low contrast level, we use ImageJ to detect manually the capsule contour. The channel and membrane contours are determined at the center of the dark line. We then calculate the surface S of the profile, its total length L and its axial length L_a as shown in Fig. 1(b). The parachute depth is given by $L_p = L - L_a$. The experimental error on the lengths 2ℓ, L, L_a is of order 1 μm. The wall corrugations,

5
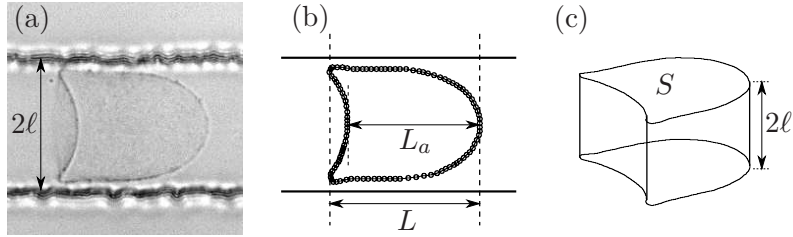
FIG. 1. Capsule profile extraction from an experimental image: (a) Initial image; (b) Contour extracted with ImageJ; (c) Approximate capsule volume based on the contour area and channel depth.

which appear in Fig. 1(a), are also of order 1 μm. They lead to small oscillations of the capsule profile, which are of the same order as the measurement error.

The initial capsule radius a cannot be inferred directly from the experimental images, which are only projections of the deformed profile. We thus estimate an approximate capsule volume as the volume of a cylinder with section S and height 2ℓ (Fig. 1(c)). This allows us to calculate an approximate capsule radius a_{app} given by

$$a_{app} = \left(\frac{3\ell S}{2\pi} \right)^{1/3}.$$ (2)

The relationship between a_{app} and the exact radius a is given by the numerical model of the capsule flow problem.

III. MODEL OF THE FLOW OF A CAPSULE IN A PORE

In order to analyze the experiments, a mechanical model of the set-up is needed. The flow of a capsule in circular[12,19] or square[10,14] cross-section channels has been studied. We briefly outline the numerical model and provide new results for the flow of capsules in square-section channels for a wide range of size ratios and flow strengths, and for strain-hardening or strain-softening capsule membranes. Details on the problem equations and their solution by means of the coupled boundary integral and finite element methods can be found in Hu et al.[14].
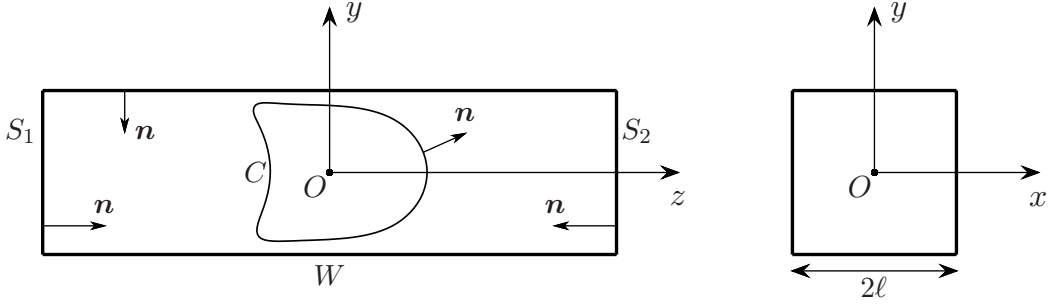
FIG. 2. Prismatic channel with axis Oz. The cross-section is square with side 2ℓ.

A. Problem statement

An initially spherical capsule (radius a) flows along the z-axis of a microfluidic channel with a square cross-section (side 2ℓ) in the perpendicular xy-plane. The interior and exterior of the capsule are incompressible Newtonian fluids with the same density ρ and viscosity μ. The thin membrane of the capsule is an impermeable hyperelastic isotropic material with surface shear modulus G_s and area dilatation modulus K_s. Apart from the capsule membrane mechanical properties, the two other main parameters of the problem are the size ratio a/ℓ between the capsule initial radius and the channel cross dimension, and the capillary number

$$Ca = \mu V/G_s, \tag{3}$$

which measures the ratio between viscous and elastic forces, where V is the mean external undisturbed flow velocity along the z-axis of the channel.

We denote $\boldsymbol{v}^{(\beta)}$, $\boldsymbol{\sigma}^{(\beta)}$ and $p^{(\beta)}$ the velocity, stress and pressure fields in the suspending ($\beta = 1$) and internal ($\beta = 2$) liquids. The flow Reynolds number is assumed to be very small, so that the internal and external liquid motions satisfy the Stokes equations:

$$\nabla p^{(\beta)} = \mu \nabla^2 \boldsymbol{v}^{(\beta)}, \quad \nabla \cdot \boldsymbol{v}^{(\beta)} = 0, \quad \beta = 1, 2. \tag{4}$$

They are solved in a domain bounded by the cross-sections S_1 at the tube entrance and S_2 at the exit, both located far from the capsule center of mass (Fig. 2). The other domain boundaries are the channel wall W and the capsule surface C. The unit normal vector $\boldsymbol{n}$ to all the boundaries points towards the suspending liquid. The problem boundary conditions are:

7

- no flow disturbance on S_1 and S_2 as they are far from the capsule:

$$\boldsymbol{v}^{(1)}(\boldsymbol{x}, t) \to \boldsymbol{v}^\infty(\boldsymbol{x}), \quad \boldsymbol{x} \in S_1 \cup S_2, \tag{5}$$

where $\boldsymbol{v}^\infty$ is the parabolic flow velocity in a square channel in the absence of capsule.

- uniform pressure on S_1 and S_2:

$$p^{(1)}(\boldsymbol{x}, t) = 0 \quad \boldsymbol{x} \in S_1, \tag{6}$$

$$p^{(1)}(\boldsymbol{x}, t) = \Delta P(t) + \Delta P^\infty \quad \boldsymbol{x} \in S_2, \tag{7}$$

where ΔP^∞ is the undisturbed pressure drop between S_1 and S_2 in the absence of capsule and ΔP is the additional pressure drop due to the capsule.

- no slip on the channel wall W:

$$\boldsymbol{v}^{(1)}(\boldsymbol{x}, t) = \boldsymbol{0}, \quad \boldsymbol{x} \in W, \tag{8}$$

- no slip on the capsule deformed surface C:

$$\boldsymbol{v}^{(1)}(\boldsymbol{x}, t) = \boldsymbol{v}^{(2)}(\boldsymbol{x}, t) = \frac{\partial}{\partial t}\boldsymbol{x}(\boldsymbol{X}, t), \quad \boldsymbol{x} \in C, \tag{9}$$

where $\boldsymbol{X}$ denotes the initial position of a membrane material point located at position $\boldsymbol{x}$ at time t.

- the load per unit area $\boldsymbol{q}$ on the membrane is due to the viscous traction jump:

$$(\boldsymbol{\sigma}^{(1)} - \boldsymbol{\sigma}^{(2)}) \cdot \boldsymbol{n} = \boldsymbol{q}, \quad \boldsymbol{x} \in C. \tag{10}$$

B.   Membrane laws

As the membrane thickness is negligibly small compared to the capsule dimensions, the membrane can be treated as a hyperelastic surface devoid of bending stiffness. The in-plane deformation is then measured by the principal extension ratios λ_1 and λ_2. Owing to the

combined effects of hydrodynamic forces, boundary confinement and membrane deformability, the capsule can be highly deformed as shown in Fig. 1. Consequently the choice of the membrane constitutive law is important. We consider two simple laws with constant material coefficients. One such law (NH) is the widely used neo-Hookean law, which models the membrane as an infinitely thin sheet of a three-dimensional isotropic and incompressible material. The principal Cauchy in-plane tensions (forces per unit arc length of deformed surface curves) can be expressed as[20]

$$\tau_1 = \frac{G_s}{\lambda_1 \lambda_2} \left[\lambda_1^2 - \frac{1}{(\lambda_1 \lambda_2)^2} \right] \text{ (likewise for } \tau_2 \text{).} \tag{11}$$

The membrane dilatation modulus K_s is then given by $K_s = 3G_s$.

Another law was originally proposed by Skalak *et al.*[11] to describe the membrane deformations of red blood cells. The principal tensions are

$$\tau_1 = \frac{G_s}{\lambda_1 \lambda_2} \left[\lambda_1^2(\lambda_1^2 - 1) + C(\lambda_1^2 \lambda_2^2)(\lambda_1^2 \lambda_2^2 - 1) \right] \text{ (likewise for } \tau_2 \text{),} \tag{12}$$

where the dimensionless parameter C mainly measures the resistance to area-dilatation. The membrane dilatation modulus is then given by $K_s = (1 + 2C)G_s$. This law has strain-hardening properties which increase with C for $C \geq 0$[20]. When $C = 1$, the Skalak *et al.* law (SK) and the NH law lead to the same small deformation behavior with the same values of G_s and K_s. Contrary to the SK law, the NH law is strain-softening under large deformation[20]. We thus study the effect of the membrane strain-hardening or softening property on the capsule deformation by considering the flow of capsules enclosed by either a NH membrane or by a SK membrane.

To close the problem, we must relate the load on the membrane given by Eq. (10) to the elastic Cauchy tension tensor $\boldsymbol{\tau}$. In absence of inertia, the membrane equilibrium leads to

$$\boldsymbol{\nabla}_s \cdot \boldsymbol{\tau} + \boldsymbol{q} = \boldsymbol{0}. \tag{13}$$

C. Numerical procedure

The problem is solved coupling a boundary integral method to solve for the fluid flow and a finite element method to solve for the membrane mechanics[13,14]. The advantage of the procedure is that only the boundaries of the flow domain S_1, S_2, W, C are discretized.

The capsule mesh is generated by first inscribing an icosahedron (regular polyhedron with 20 triangular faces) in the sphere and subdividing the elements sequentially until the required number of elements is reached[13,14]. The capsule mesh is composed of 1280 P_2 elements and 2562 nodes. The mesh of the external tube walls (S_2 and W) is generated using P_1 elements with Modulef (INRIA Rocquencourt, France)[14] and is refined in the central portion of the channel, where the capsule is located. The boundary mesh has 1905 nodes and 3768 elements. All the results are obtained with a non-dimensional time step $\Delta t \times V/\ell = 5 \times 10^{-5}$.

The equations are solved in a reference frame moving with the capsule center of mass. Thus for each time step, we compute the velocity v_o of the capsule center of mass and move back the whole capsule by $v_o \Delta t/\ell$, so that the capsule remains centered in the tube domain.

The model inputs are the capillary number Ca, the size ratio a/ℓ and the membrane law. The model outputs are the capsule centroid velocity v_o and the steady deformed capsule shape. From the latter, it is possible to compute the evolution of the total length L, of the parachute depth L_p and of the apparent capsule radius a_{app} with size ratio a/ℓ and Ca. The model also yields the elastic tension distribution in the membrane. If a failure criterion is known for the membrane, it is then possible to infer whether there is a risk of breakup.

Since the bending modulus of the membrane has been neglected, the capsule wall buckles locally in the regions where the elastic tensions are compressive[14]. In order to study the post-buckling behavior of the capsule, bending moments and transverse shear forces should be added to Eq. (13) and a constitutive equation should be postulated to relate bending moments and local deformations. It follows that the bending behavior of a capsule is a complicated problem of shell mechanics that is not completely resolved yet. The simplified membrane model that we use here is appropriate to model capsules with a very low bending resistance. It detects zones where tensions are compressive and where the capsule wall may buckle. The use of triangular finite elements allows for some profile oscillations in compression areas without creating any numerical instability. Such numerical 'folds' have a wavelength which depends on the grid point spacing. Hence they do not model the physical post-buckling behavior of the capsule[14].
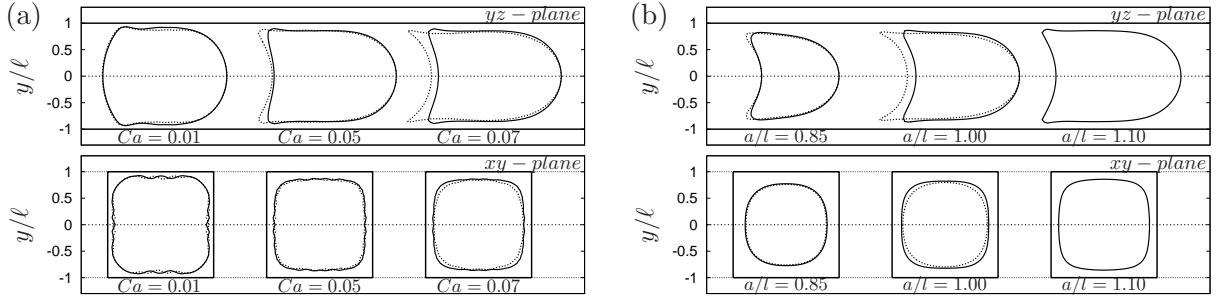
FIG. 3. Comparison of steady profiles (solid line: SK law, dashed line: NH law): (a) Effect of Ca for constant $a/\ell = 1.1$; (b) Effect of a/ℓ for constant $Ca = 0.1$.

D.   Effect of membrane law on capsule deformation

We consider the flow of capsules with a NH or a SK membrane in a microfluidic pore for different size ratios a/ℓ at various flow strengths Ca. It is assumed that the steady-state configuration is reached, when the area of the capsule varies by less than $5 \times 10^{-4} \times (4\pi a^2)$ over a non-dimensional time $Vt/\ell = 1$. All the following results pertain to this equilibrium state. At steady-state, the membrane and thus the internal fluid are motionless. This means that assuming the same value of viscosity for the internal and external liquids does not limit the validity of the results; the viscosity ratio only influences the time the capsule needs to reach a steady state (this time increases as the internal viscosity increases). Furthermore, as the pressure inside the capsule is uniform, the curvature at the capsule upstream tip must be larger than at the rear to account for the viscous pressure drop in the lubrication film around the capsule. This explains why parachute or slug shapes are obtained.

We first show the deformed profiles of a large capsule ($a/\ell = 1.1$) in Fig. 3(a) for increasing flow strengths $Ca = 0.01, 0.05, 0.07$. The axial profile in the zy-plane is what is observed experimentally. At low flow strength ($Ca = 0.01$), the profiles of the NH and SK capsules are almost superimposed, since the two membrane laws are equivalent at small deformations. For $Ca = 0.05$, a parachute shape is found for the NH capsule, while the SK capsule still has a slug shape. This indicates that the flow strength level Ca_c, for which the parachute shape appears, depends on the membrane constitutive law. The cross profiles in the xy-plane show that the capsule shape is not axisymmetric as the membrane tends to fill the corners of the channel.

Fig. 3(b) shows the capsule profile at a high flow strength $Ca = 0.1$ for various size ratios.

11
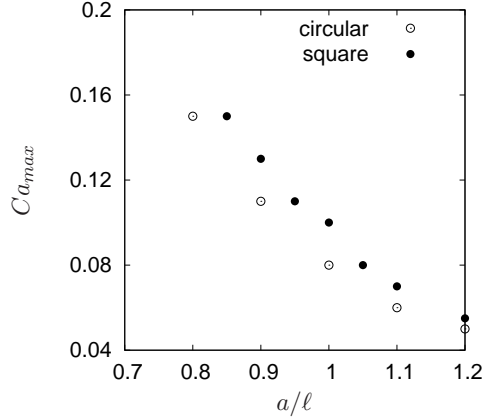
FIG. 4. Maximum values of Ca, for which a steady profile is obtained for a capsule enclosed by a NH membrane. The comparison between a square or circular pore with radius ℓ shows the effect of the corners.

The parachute shape appears for all the capsules. The NH capsule is more deformed than the SK one, even though the difference is quite small for small capsules ($a/\ell \leq 0.9$). For $a/\ell = 1.10$, we can get a steady-state solution for the SK membrane, only. Indeed, a strain-softening NH capsule undergoes continuous elongation, when a maximum flow strength Ca_{max} is exceeded. This phenomenon was already observed in a cylindrical tube where the situation is axisymmetric[9]. It is due to the fact that a strain-softening membrane has a deformation, which increases faster than linearly with the imposed load[1]. The values of Ca_{max} for a square-section tube are shown in Fig. 4, where they are compared with the values obtained for a cylindrical tube with radius ℓ. We note that Ca_{max} is slightly larger for a square than for a circular pore because, for the same flow rate, the viscous shear on the capsule is less in a square pore than in a circular one due to the presence of corners. This continuous elongation phenomenon does not occur with a SK membrane, at it is strain-hardening[1].

The overall capsule deformation is quantified by the maximum length L/ℓ and the parachute depth L_p/ℓ, as shown in Fig. 5. The parachute forms at the capsule rear, when the capillary number exceeds the critical value Ca_c. The value of Ca_c is less for a NH capsule than for a SK one. Below Ca_c, the capsule elongation is small and there is little influence of the membrane law. When $Ca > Ca_c$, both L/ℓ and L_p/ℓ increase much faster with Ca for a NH capsule than for a SK one. This is due again to the strain-softening property of the NH

12
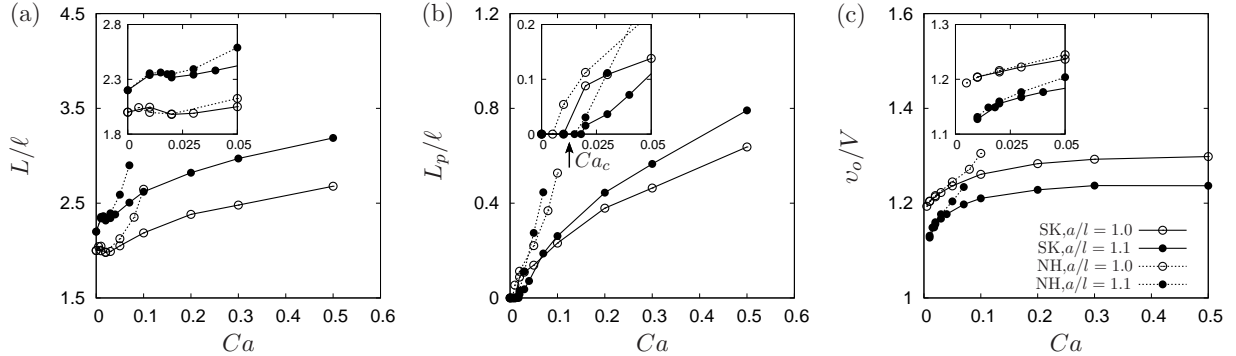
FIG. 5. Effect of Ca, a/ℓ and membrane law on the capsule total length L/ℓ, parachute depth L_p/ℓ and center of mass velocity υ_o/V.

membrane, which allows larger deformation for the same stress level than a strain-hardening SK membrane. The overall effect of the size ratio is to increase the deformation for a given flow strength. Finally, we note that the capsule velocity decreases, when the confinement increases or when the deformation decreases.

E.   Size, deformation and velocity charts for a capsule with NH or SK law

The results of the numerical model are gathered in charts, where the main output parameters, i.e. total length L/ℓ, parachute depth L_p/ℓ, approximate radius a_{app}/ℓ and centroid velocity υ_o/V, are plotted as functions of Ca and a/ℓ for capsules with a NH membrane (Fig. 6) or with a SK membrane with $C = 1$ (Fig. 7). For the NH capsules, the range of Ca is limited by the continuous elongation phenomenon. For the SK capsules, the range of Ca is a priori unlimited. However, we give results for Ca up to 0.5, because the variation of the different geometrical quantities is almost linear with Ca when $Ca \geq 0.2$, while the velocity is almost constant. For very large capsules ($a/\ell \geq 1.2$) and high flow strength ($Ca \geq 0.5$) the deformation at the rear and the concomitant curvature of the tip become too large to be modeled correctly by a membrane law where bending rigidity is neglected. This is why we do not give results for $Ca > 0.3$ when $a/\ell = 1.2$.

Note that a_{app}/ℓ does not vary much with Ca, except for very low values of Ca. This point will be important for the determination of the actual size ratio of a capsule from the measurement of a_{app}/ℓ. The relative difference between a_{app} and a is of order 17% for small capsules and decreases to less than 10% for the largest capsules. Finally, we have refrained

13
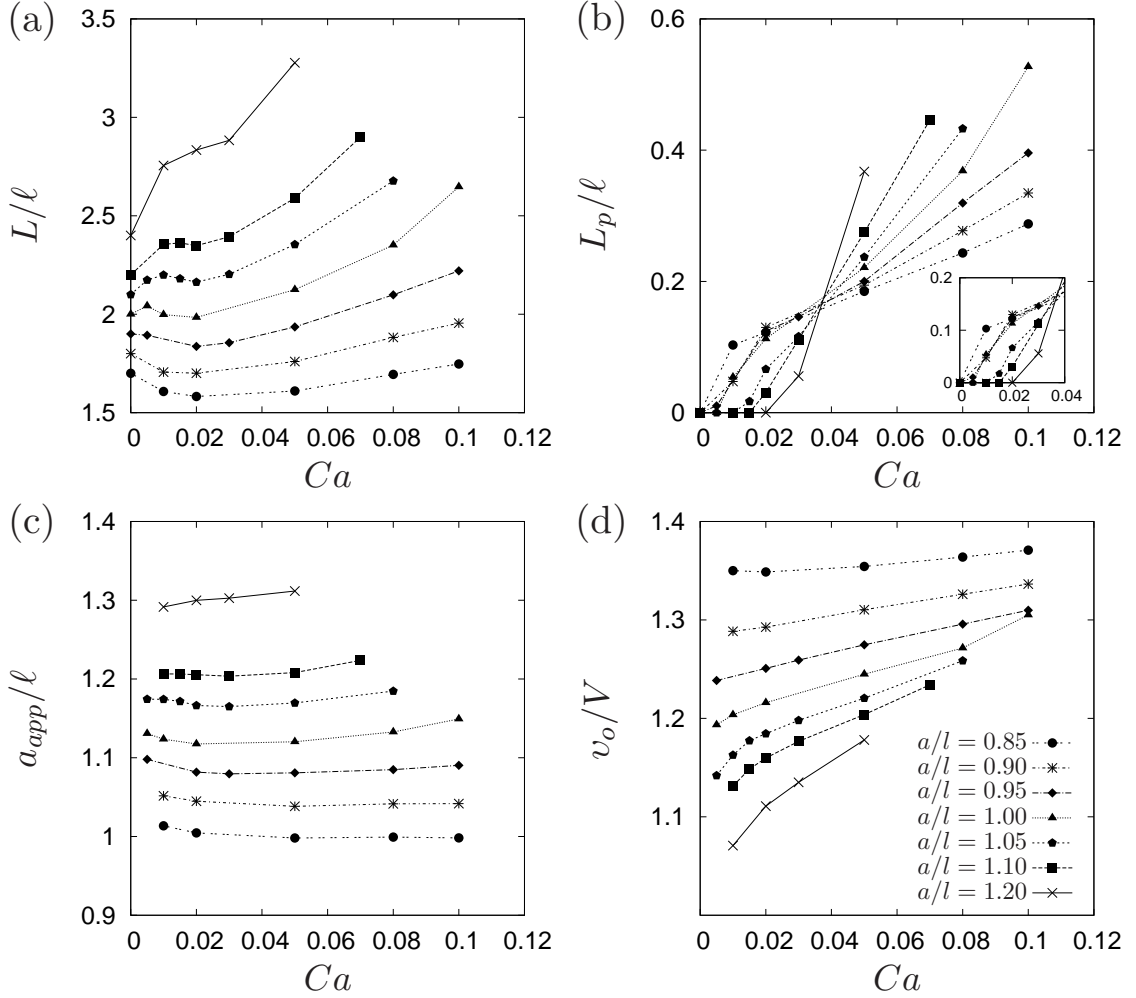
FIG. 6. Plots of the capsule total length L/ℓ, parachute depth L_p/ℓ, approximate radius a_{app}/ℓ and velocity of mass center v_o/V obtained with the NH law.

from giving results for small capsules with $a/\ell < 0.85$ because they require high values of Ca to be significantly deformed. Experimentally, such high values of Ca imply high values of the flow velocity V, for which it is difficult to obtain capsules images with good enough contrast and sharpness.

F.   Inverse analysis of the experimental results

We have developed a new MatLab program, inspired from the algorithm of Chu *et al.*[9], to automatically perform the inverse analysis of capsule profiles in square channels. The numerical data shown in Fig. 6 and 7 are linearly interpolated on a regular grid. A membrane

14
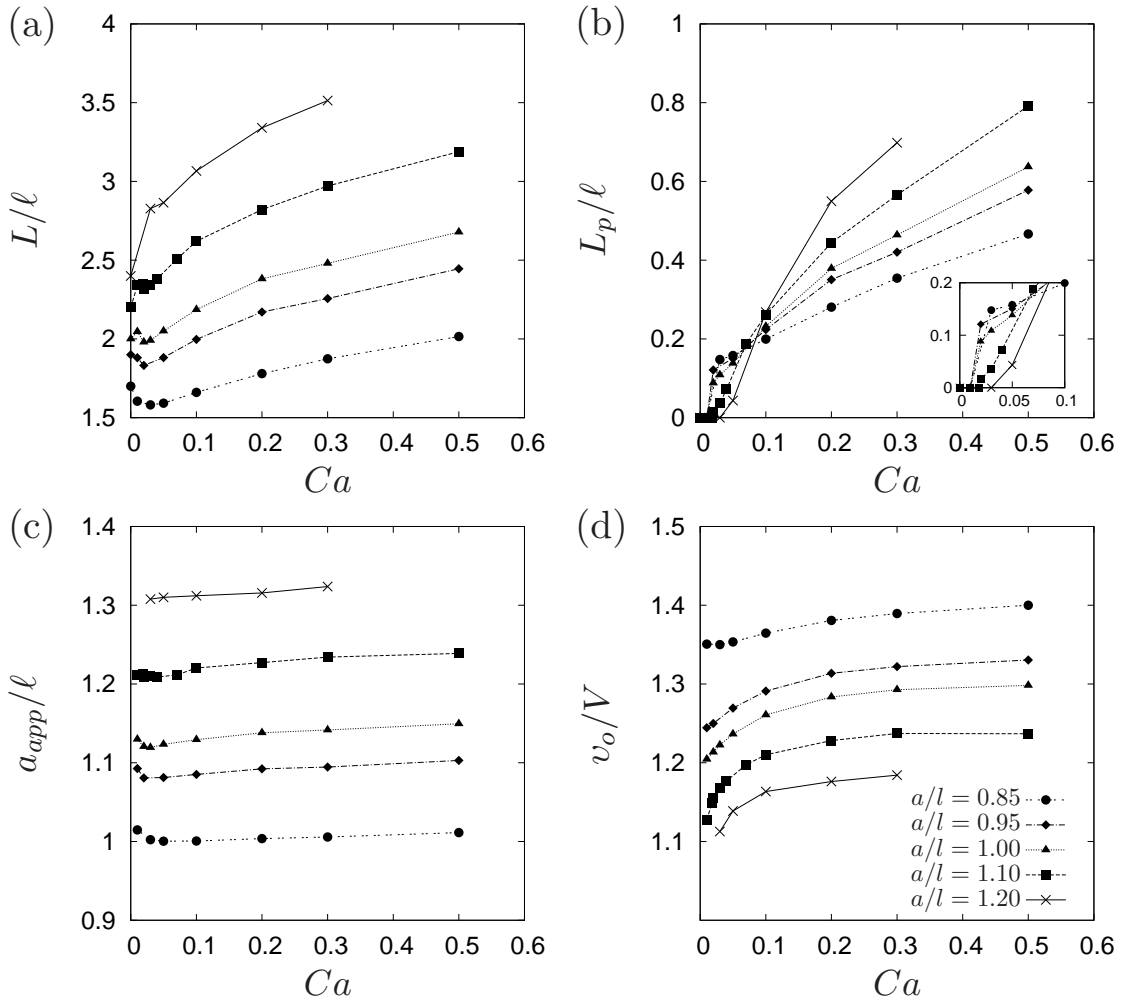
FIG. 7. Plots of the capsule total length L/ℓ, parachute depth L_p/ℓ, approximate radius a_{app}/ℓ and velocity of mass center v_o/V obtained with the SK law ($C = 1$).

law is first assumed and the algorithm then determines the size ratio a/ℓ and the capillary number Ca, for which the experimental and numerical values of L/ℓ and L_p/ℓ fit best.

Tolerances have been defined to account for the uncertainty on experimental measurements. Depending on the flow conditions, the membrane can appear more or less fuzzy. Considering an error of 2% on ℓ and L, we assume a tolerance of 4% on L/ℓ. The parachute depth is more difficult to measure with precision. For $L_p/\ell < 0.05$ we consider that there is no parachute and that we are close to the critical value Ca_c. For $0.05 < L_p/\ell < 0.1$, we take a tolerance of 50%. For $0.1 < L_p/\ell < 0.2$, we take a tolerance of 25% and for higher values the tolerance is 15%.

The size ratio is first calculated from a_{app}/ℓ, Ca and the corresponding database. For the

15
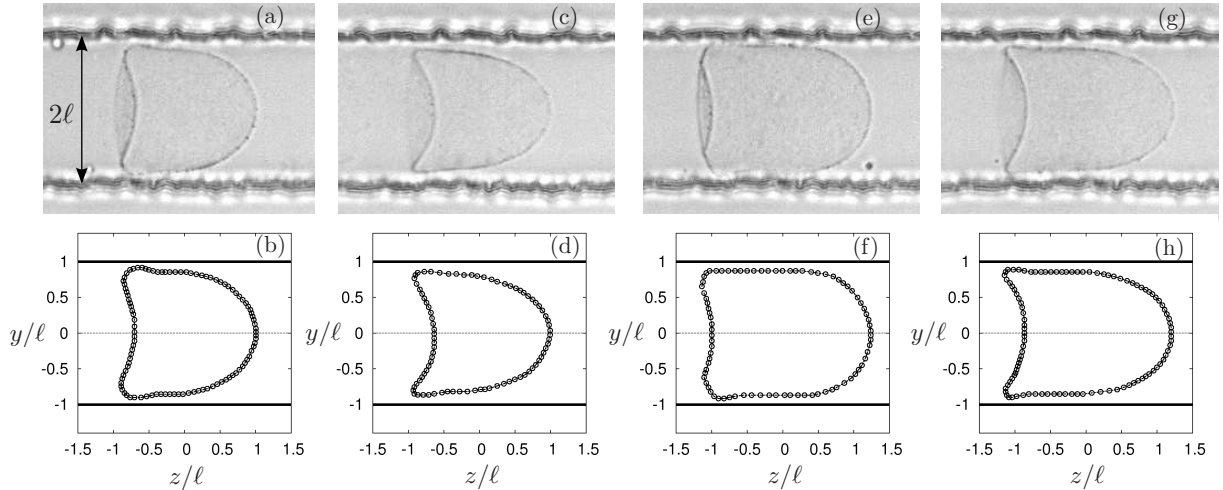
FIG. 8. Experimental images and corresponding extracted deformed profiles. The top row images are the original experimental images, while the bottom row figures are the corresponding extracted profiles. (a-b) $a_{app}/\ell = 1.08, v_o = 3.0$ mm/s; (c-d) $a_{app}/\ell = 1.05, v_o = 7.3$ mm/s; (e-f) $a_{app}/\ell = 1.2, v_o = 1.4$ mm/s; (g-h) $a_{app}/\ell = 1.16, v_o = 3.4$ mm/s.

first iteration, Ca is initialized with the mean value of the total range (which depends on the membrane constitutive law). The size ratio is then used to calculate two ranges of possible capillary numbers from the experimental values of L/ℓ and L_p/ℓ with their tolerances. If these two ranges intersect, we calculate and use the intersection mean value to process the next iteration of the algorithm until the mean value of Ca remains constant within 10^{-3} over two successive iterations. For each value of Ca in the intersection interval, we calculate the mean fluid velocity V from the capsule velocity v_o and the velocity ratio v_o/V of the database. Finally, we calculate the shear moduli that correspond to each Ca in the intersection interval by means of Eq. 3. This procedure is executed for 5 values of a_{app}/ℓ (a_{app}/ℓ, $a_{app}/\ell \pm 1\%$ and $a_{app}/\ell \pm 2\%$) to take into account a relative uncertainty of about 4%. Then, we calculate the mean value of the shear modulus and the standard deviation.

16
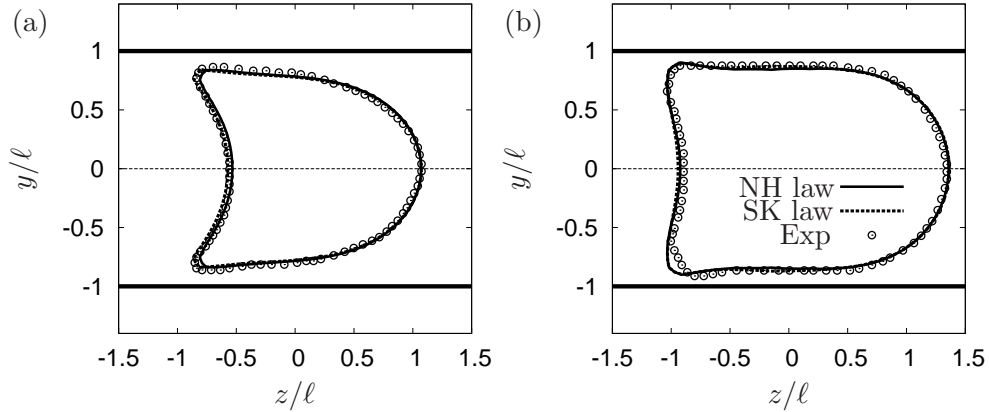
FIG. 9. Superposition of experimental and numerical capsule profiles in square-section microfluidic channel. The numerical profiles are obtained with the NH law or with the SK (C=1.0) law. (a) NH law ($Ca = 0.08$, $a/\ell = 0.90$) and SK law ($Ca = 0.17$, $a/\ell = 0.90$); (b) NH law ($Ca = 0.03$, $a/\ell = 1.10$) and SK law ($Ca = 0.05$, $a/\ell = 1.09$).

IV. RESULTS AND DISCUSSION

A. Capsule deformation in a square-section channel

Typical profiles of capsules mildly to highly deformed in a square-section channel are shown in Fig. 8. Capsules (a) and (c) have almost the same apparent size, which corresponds to an actual size ratio of order $a/\ell = 0.9$ (Fig. 6 or 7). However capsule (c) has a higher velocity than capsule (a). As a consequence capsule (c) is more deformed than capsule (a) and has a deeper parachute. The same phenomenon is observed for capsules (e) and (g), which have the same apparent size corresponding to an actual size ratio of order $a/\ell = 1.05 \sim$ 1.1. Being the fastest one, capsule (g) is the most deformed with the deepest parachute.

B. Determination of membrane properties

As an example, we first apply the inverse analysis algorithm with either the NH or the SK law, to a typical capsule which is smaller than the pore (profile (d) of Fig 8). We find $a/\ell = 0.9$ in both cases, $Ca = 0.08$ for the NH law capsule and $Ca = 0.17$ for the SK law one. We then compute exactly the equilibrium deformed profiles corresponding to these two cases and compare them with the experimental profiles in Fig. 9(a). We note that the

17

deformed profile of a small capsule can be well fitted with either the NH or the SK law. However, the capillary number for the SK capsule is about twice that for the NH capsule, due to the strain-hardening property of the SK membrane, which requires higher loads to reach the same deformation as the NH one. The process is repeated with a capsule, which is larger than the pore (profile (f) of Fig 8). We find two slightly different values of the initial radius $a/\ell = 1.1$ for the NH law and $a/\ell = 1.09$ for the SK law. The values of Ca are both small and of the same order, as should be expected, since for small deformation the two laws are equivalent. Computing the deformed profiles corresponding to the couples of values of a/ℓ and Ca with either the NH or the SK law, we can again fit them well to the experimental ones as shown in Fig. 9(b).

We then proceed to analyze a population of 18 capsules of different initial sizes, flowing through the square-section capillary tube at different flow rates. We use the inverse analysis algorithm to deduce, for each capsule, the mean value of the shear elastic modulus of the membrane G_s. We define the mean capsule elongation Λ

$$\Lambda = P/2\pi a \tag{14}$$

where P is the perimeter of the deformed capsule profile. It is then convenient to plot the values of G_s in terms of Λ rather than the size ratio. As shown in Fig. 10, when we assume a NH law for the membrane, we find a constant value of the shear modulus $G_s = 0.036 \pm 0.006$ N/m for a mean elongation ranging from 1 to 1.25 (which corresponds to a fairly large deformation!).

If we assume a SK law for the membrane, the value of G_s for small deformation ($\Lambda \leq 1.03$) is of the same order as the one obtained for the NH law. However, as the profile deformation increases, the corresponding values of G_s decrease by a factor three. This is a consequence of the strain-hardening property of the SK law. The fact that we cannot find a constant value for the shear modulus of the SK law for all deformation levels indicates that the membrane of ovalbumin capsules is not strain-hardening, but rather strain-softening as modeled by the NH law.

C. Discussion

The objective of this work was to determine plausible elastic properties for the membrane of capsules. We have chosen two simple constitutive laws with the *same* small deformation

18

behavior, but with either strain-softening or strain-hardening properties under large strain. The use of the neo-Hookean law as the strain-softening one means that we have arbitrarily fixed the area-dilation to shear modulus ratio to $K_s/G_s = 3$. For the strain-hardening law, we could have used values of C smaller than unity, which would have lowered the strain-hardening feature of the law (without eliminating it) and might have led to values of G_s less dependent on the deformation. However, using $C < 1$ would have made the comparison with NH law less meaningful as the small deformation parameters would have been different.

We note that there is some dispersion of the results in Fig 10. The dispersion is larger for the NH law than for the SK one. This is due to the fact that, when we use the NH law, the capillary number is small and the geometrical parameters L and L_p vary non-linearly with Ca. When we use the SK law, the values of Ca are larger and the variation of L and L_p with Ca is almost linear.

Another question is linked to the fact that the channel we used is not perfectly square (as is usually the case with PDMS channels). Of course, we could have run the model with the exact dimensions of the channel, but we decided instead to provide general charts for the flow in square channels and use them to analyze our results. As a check, we compare the value we find, $G_s = 0.036 \pm 0.006$ N/m, with the previous study of Chu et al.[9], who obtained $G_s = 0.042 \pm 0.016$ N/m for ovalbumin capsules prepared under the same conditions and flowing in a 50 μm glass capillary tube. The two mean values of G_s fall in the same range within experimental errors.

The reason why the ovalbumin membrane seems to be strain-softening is probably due to the conformation of the albumin molecule at the interface. For a small reticulation time of 5 min, the density of covalent links between the protein molecules is low and the protein chains are loosely linked. This may explain why the membrane is easily deformable, as described by a NH law. It has not been possible to obtain deformations larger than 25%, so that we do not know for what deformation the membrane breaks.

V. CONCLUSION

We show here that it is possible to infer plausible mechanical properties of an artificial capsule membrane from experiments, where the capsule has to deform to flow inside a small pore with cross dimensions of the same order as those of the capsule. The method is based on

19
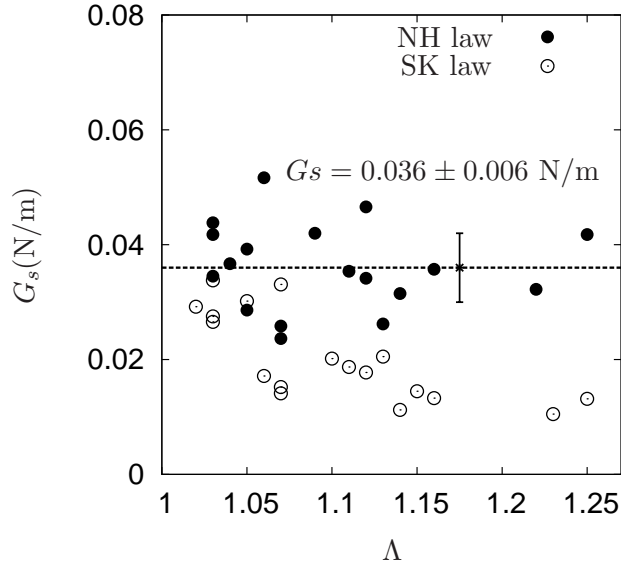
FIG. 10. Membrane shear modulus G_s as a function of capsule mean deformation Λ. Dashed line: average value of G_s determined with the NH law.

the coupling of experimental observations with a rigorous mechanical model of the system. It also implies a strong hypothesis on the value of the area dilation to shear modulus ration, which is assumed to be $K_s/G_s = 3$. The method works well, if the deformation of the capsule is large enough. Indeed for a small deformation, it is not possible to distinguish between different laws and there is some dispersion in the results. Thus, it is best to use a pore, such that the size ratio of the capsules is of order unity. Small capsules ($a/\ell \leq 0.8$) have to be flowed fast to be deformed with concomitant difficulties of observation leading to profile fuzziness. In order to reach large deformation, while keeping the capsule velocity moderate, a high viscosity suspending liquid is necessary. But the price to pay is that the high viscous pressure drop inside the microchannel may lead to the destruction of the connections. The advantage of using a square-section channels rather than a cylindrical one is linked to the easy fabrication of microfluidic tubes of any size and to the easy connection with the propulsion device. Furthermore, this system can be built in a microfluidic fabrication device to monitor the properties of the capsules in situ[21]. We note that it is even possible to infer the large deformation behavior of the membrane, at least decide whether it is strain-softening or hardening.

20

REFERENCES

[1] D. Barthès-Biesel, "Modeling the motion of capsules in flow," Current Opinion in Colloid and Interface Science, **16**, 3–12 (2011).

[2] M. Carin, D. Barthès-Biesel, F. Edwards-Lévy, C. Postel, and D. Andrei, "Compression of biocompatible liquid-filled HSA-alginate capsules: determination of the membrane mechanical properties," Biotechnol. Bioeng., **82**, 207–212 (2003).

[3] K. S. Chang and W. L. Olbricht, "Experimental studies of the deformation and breakup of a synthetic capsule in steady and unsteady simple shear flow," J. Fluid Mech., **250**, 609–633 (1993).

[4] M. Husmann, H. Rehage, E. Dhenin, and D. Barthès-Biesel, "Deformation and bursting of nonspherical polysiloxane microcapsules in a spinning-drop apparatus," Int. J. of Colloid Interface Sci., **282**, 109–119 (2005).

[5] C. A. Putman and K. O. Van der Werf, "Viscoelasticity of living cells allows high resolution imaging by tapping mode atomic force microscopy," Biophysical J., **67**, 1749–1753 (1994).

[6] A. Fery and R. Weinkamer, "Mechanical properties of micro- and nanocapsules: Single-capsule measurements," Polymer, **48**, 7221–7235 (2007).

[7] R. M. Hochmuth, "Micropipette aspiration of living cells," J. Biomechanics, **33**, 15–22 (2000).

[8] Y. Lefebvre, E. Leclerc, D. Barthès-Biesel, J. Walter, and F. Edwards-Lévy, "Flow of artificial microcapsules in microfluidic channels: A method for determining the elastic properties of the membrane," Phys. Fluids, **20**, 123102 (2008).

[9] T. X. Chu, A.-V. Salsac, E. Leclerc, D. Barthès-Biesel, H. Wurtz, and F. Edwards-Lévy, "Comparison between measurements of elasticity and free amino group content of ovalbumin microcapsule membranes: discrimination of the cross-linking degree," Int. J. of

Colloid Interface Sci., **355**, 81–88 (2011).

[10]S. Kuriakose and P. Dimitrakopoulos, "Motion of an elastic capsule in a square microfluidic channel," Phys. Rev. E, **84**, 1–22 (2011).

[11]R. Skalak, A. Tozeren, R. P. Zarda, and S. Chien, "Strain energy function of red blood cell membranes," Biophysical J., **13**, 245–64 (1973).

[12]Y. Lefebvre and D. Barthès-Biesel, "Motion of a capsule in a cylindrical tube: effect of membrane pre-stress," J. Fluid Mech., **589**, 157–181 (2007).

[13]J. Walter, A.-V. Salsac, D. Barthès-Biesel, and P. Le Tallec, "Coupling of finite element and boundary integral methods for a capsule in a stokes flow," Int. J. Numerical Methods Engineering, **83**, 829–850 (2010).

[14]X.-Q. Hu, A.-V. Salsac, and D. Barthès-Biesel, "Flow of a spherical capsule in a pore with circular or square cross-section," J. Fluid Mech., **705**, 176–194 (2012).

[15]F. Edwards-Lévy, M. C. Andry, and M. C. Lévy, "Determination of free amino group content of serum albumin microcapsules using trinitrobenzenesulfonic acid: effect of variations in polycondensation pH," Int. J. Pharmaceutics, **96**, 85–90 (1993).

[16]J. C. McDonald and G. M. Whitesides, "Poly(dimethylsiloxane) as a material for fabricating microfluidic devices," Acc. Chem. Res., **35**, 491–499 (2002).

[17]G. S. Fiorini and D. T. Chiu, "Disposable microfluidic devices: fabrication, function, and application," BioTechniques, **38**, 429–446 (2005).

[18]J. B. Segur and H. E. Oberstar, "Viscosity of glycerol and its aqueous solutions," Ind. Eng. Chem., **43**, 5–8 (1951).

[19]C. Pozrikidis, "Numerical simulation of cell motion in tube flow," Annals Biomedical Eng., **33**, 165–178 (2005).

[20]D. Barthès-Biesel, A. Diaz, and E. Dhenin, "Effect of constitutive laws for two-dimensional membranes on flow-induced capsule deformation," J. Fluid Mech., **460**, 211–222 (2002).

[21]T. X. Chu, A.-V. Salsac, D. Barthès-Biesel, G. L., F. Edwards-Lévy, and E. Leclerc, "Fabrication and in situ characterization of microcapsule in a microfluidic system," Microfluidics Nanofluidics, **14**, 309–317 (2013).

22

4.2 Additional results

4.2.1 Tensions on profiles
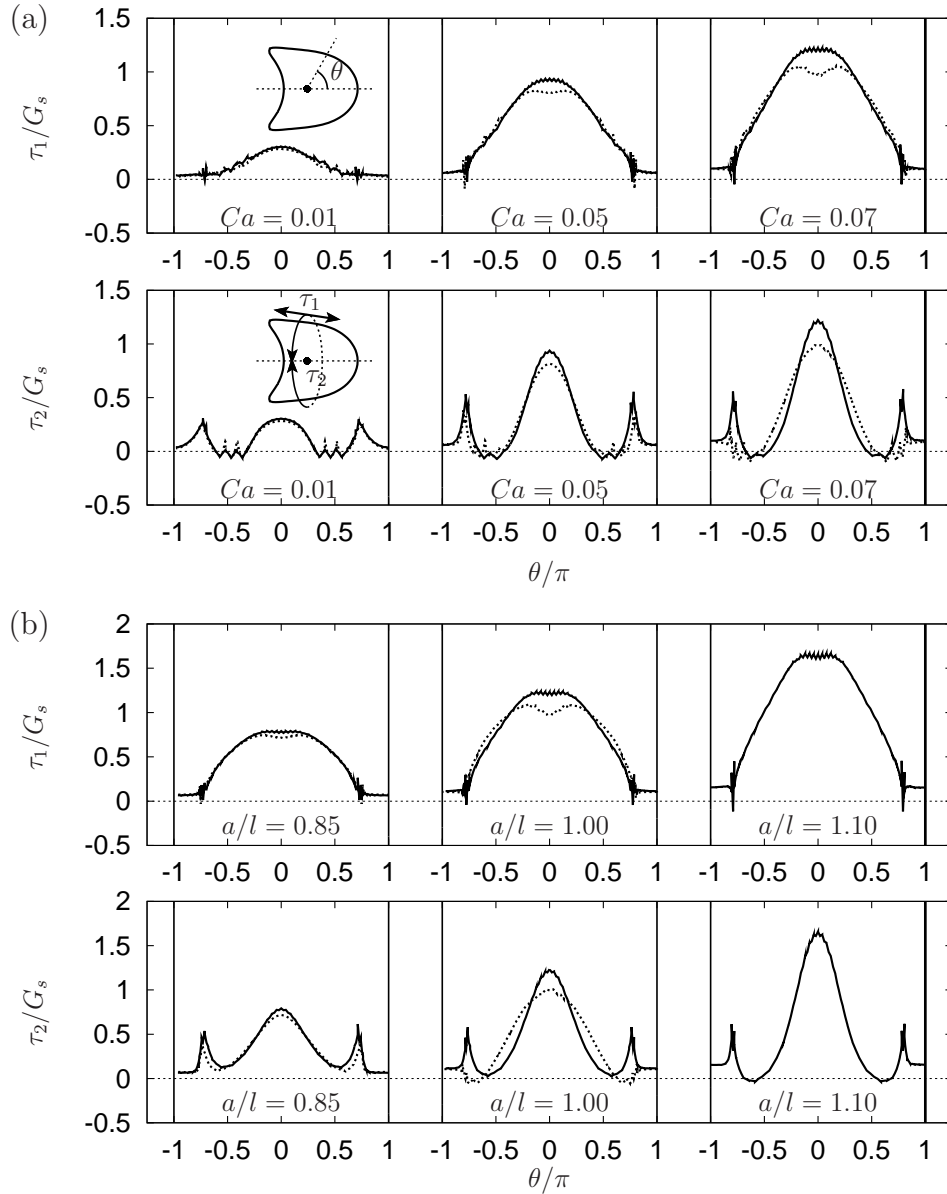
Figure 4.1: Comparison of principal tensions in the *yz-plane* along steady profiles (Solid line: Skalak law with $C = 1$, Dashed line: neo-Hookean law). The principal tensions are plotted as a function of position θ/π on the profile, e.g. $\theta/\pi = 0$ denotes the front point that lies on the channel axis. Tension τ_1 is along the capsule profile, while τ_2 is on the hoop direction which is perpendicular to the plane. (a) Effect of Ca for constant $a/\ell = 1.1$. (b) Effect of a/ℓ for constant $Ca = 0.1$.

The meridional and azimuthal principal tensions (τ_1 and τ_2) along the longitudinal

profiles on *yz-plane* are plotted as functions of the polar angle θ/π made by the position vector with the *z*- axis, as shown in Fig. 4.1.

For small capsule deformations, the tensions are also relatively small, as shown for $Ca = 0.01$ in Fig. 4.1(a) or $a/\ell = 0.85$ in Fig. 4.1(b). The tension distributions of NH and SK ($C = 1$) membranes are almost superimposed as should be expected since the two laws are equivalent for small deformation.

For higher flow strength ($Ca = 0.05$, 0.07) or stronger boundary confinement ($a/\ell = 0.85$, 1.10), the effect of the membrane law becomes significant. The tensions on the NH membrane are notably smaller than those on the SK ($C = 1$) one. It is of interest to note that the NH capsule undergoes larger deformations at smaller membrane tensions than the SK ($C = 1$) capsule. This is due to the fact that the NH law is strain-softening while the SK law ($C = 1$) is strain-hardening for large membrane deformations.

Chapter 5

Conclusions and perspectives

5.1   Conclusions

An initially spherical capsule flowing inside microchannels with constant cross-sections is considered in this dissertation. This fluid-structure problem in confined flows is solved by an adapted 3D model coupling the Boundary Integral (BI) method for the fluid problem and the Finite Element (FE) method for the solid problem [108, 44]. It has been shown that this 3D BI+FE model can provide excellent results even if the flowing capsule undergoes large deformations and negative tensions.

We have shown in this dissertation how three-dimensional effects affect the flow of capsules in channels with cross-dimensions comparable with the capsule diameter. The confinement effect due to the channel walls compresses the capsule in the direction perpendicular to the channel axis. This leads to compression of the membrane and a tendency towards buckling that has been observed experimentally. The flow of a capsule in a small channel is thus a three-dimensional process even when the channel and the capsule share the same revolution axis.

These three-dimensional effects have been specifically studied and we have shown that in a cylindrical channel with a circular cross-section, the 3D capsule deformation is well approximated by an axisymmetric simple model. This is an interesting and important result as it is much easier and faster to use an axisymmetric numerical model rather than a full three-dimensional one.

The three-dimensional aspect of the problem cannot be simplified in the case of microfluidic channels with square cross-section. The capsule flowing in a square channel can expand in the corners of the channel, the deformed capsule profile is therefore not axisymmetric. Compared with the case of a capsule in cylindrical channel, the square capsule is less deformed for the same given capillary number and aspect ratio. Larger flow rates must be used in a square channel than in the cylindrical one to

get the same capsule deformation. It is of interest to notice as the capsule will move faster and its detection in experiments will be more difficult. We have also shown that the capsule flowing in a rectangular channel for which the width is twice the height is less confined than that in a square channel. Its larger cross-sectional space allows the capsule to expand more in the x- direction to deform non-axisymmetrically.

Based on the numerical results, we have shown that it is possible to infer the mechanical properties of an artificial capsule membrane from experiments, where the capsule has to deform to flow inside a small channel with cross dimensions of the same order as those of the capsule. This novel method is based on the coupling of experimental observations with a rigorous mechanical model of the system. The applications of this method on a population of microcapsules with a cross-linked ovalbumin membrane have shown to be successful, if the deformation of the capsule is large enough. Indeed for a small deformation, it is not possible to distinguish between different membrane constitutive laws and there is some dispersion in the results. Thus, it is best to use a channel, such that the size ratio of the capsules is of order unity. Indeed, it is shown that small capsules ($a/\ell \leq 0.8$) have to be flowed fast to be deformed with concomitant difficulties of observation leading to profile fuzziness. In order to reach large deformation, while keeping the capsule velocity moderate, a high viscosity suspending liquid is necessary. But the price to pay is that the high viscous pressure drop inside the microchannel may lead to the destruction of the tube connections.

The advantage of using a square section channel rather than a cylindrical one is linked to the easy fabrication of microfluidic tubes of any size and to the easy connection with the propulsion device. Furthermore, this system could well be built in a microfluidic fabrication device to monitor the properties of the capsules in situ. We note that it is even possible to infer the large deformation behavior of the membrane, at least decide whether it is strain-softening or hardening.

5.2 Perspectives

Nowadays, the increasing number of demands in microcapsule applications contribute to the fast development of numerical and experimental studies on confined capsule flows. Based on some general assumptions, we have specifically studied an initially spherical capsule flowing along the axis of straight microfluidic channels in this dissertation. For future study, it will be interesting to continue the present research in the following aspects:
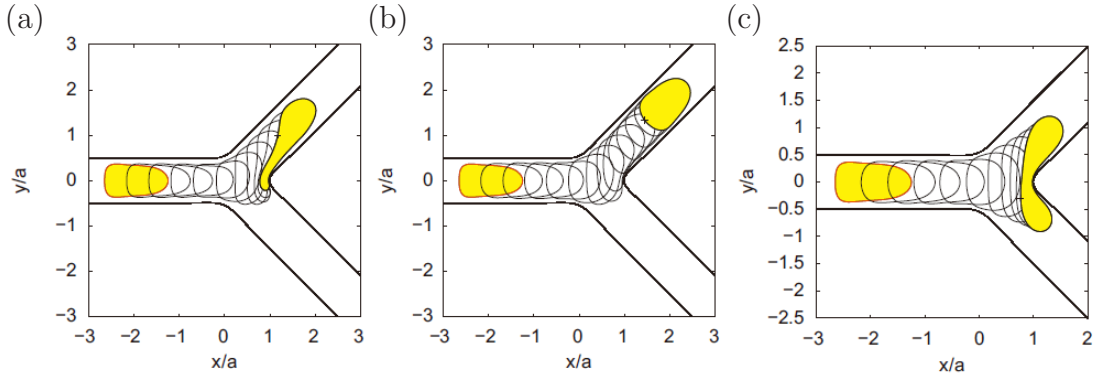
Figure 5.1: Motions of a droplet inside a bifurcating channel. Image from [78].

Capsule flowing in bifurcating channels When a capsule is flowing inside a bifurcating channel, as shown in Fig. 5.1, the downstream flows are generally unequal and complicated to be determined. This "phase separation" problem exists widely in natural blood microcirculation and in microfluidic applications. It has been shown that the motions of droplets and capsules through a bifurcating channel exhibits rich dynamics [78]. A theoretical model for red blood cell motion in bifurcating microvessels was proposed by EI-Kareh and Secomb, which was limited to rigid spherical particles [26]. Recently, Pozrikidis [78] proposed a numerical model to consider the flow of a droplet inside two-dimensional bifurcating channels using the boundary-element method. The ability of the droplet to remain intact as it passes through the bifurcation was discussed . However, the capsule flows in bifurcating channels has not been well studied till now. It will be meaningful to enrich the present study to consider capsule flows in bifurcating channels.

Capsule migrations In bounded parabolic flows, the red blood cell (RBC) is assumed to adopt an axisymmetric parachute shape, but in fact a non-axisymmetric slipper-like shape has been frequently observed both in *in vitro* and *in vivo* experiments, as presented in section 1.4.1. A number of studies have been done to explain this issue. Noguchi and Gompper [69] have studied the shape transitions of RBC model from a non-axisymmetric discoyte to an axisymmetric parachute shape focusing on the membrane properties and corresponding critical velocities for transitions. Kaoui et al. [47] have numerically analyzed the dynamics of vesicles which are comparatively small with flow dimension in 2D unbounded Poiseuille flow. The slipper-like shapes were found to result from the loss of stability of the symmetric state and to improve the flow efficiency. Although
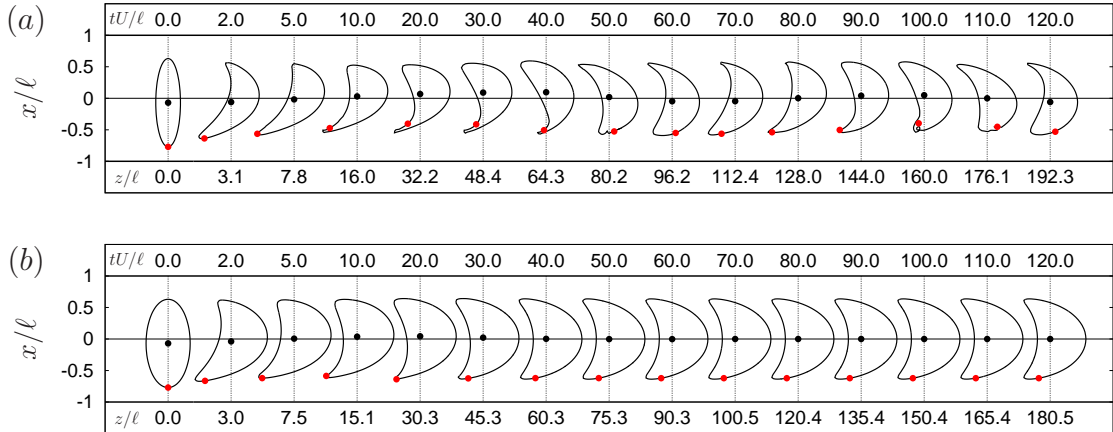
Figure 5.2: Profiles on *yz-plane* of capsules in migration. Initial eccentric distance $\Delta x_0 = -0.07$, capillary number $Ca = 0.5$, SK ($C = 1$) membrane. (a) "Thin" oblate with $a/b = 0.28$, (b) "Thck" oblate with $a/b = 0.50$.

some progresses have been made, the uncertainty of slipper-like shapes in 3D confined Poiseuille flow has not been fully discussed and then it becomes a good perspective of the present study.

Some preliminary results have been obtained. An oblate capsule is assumed to flow inside a 3D cylindrical channel, for which the long axes are $b = 0.7\ell$ and the short-to-long axis ratios a/b varies from 0.28 to 0.50. We introduce the initial eccentric distance $\Delta x_0 = -0.07$ of the mass center. The profiles of capsules in migration are shown on the *yz-plane* in Fig. 5.2. We find that the initially eccentric "thin" capsule with $a/b = 0.28$ oscillates near the channel axis, while the "thick" capsule with $a/b = 0.50$ returns rapidly to the channel axis. It implies that the "thin" oblate capsule with $a/b = 0.28$, which is usually employed as models for RBCs, requires a much longer distance (time) to return back from a non-axisymmetric disturbance. It seems that its travelling distance is very long, even longer than the length of microvessels or capillary tubes in experiments. That is why the non-axisymmetric shapes are often observed. However, more studies are still needed to confirm this conclusion.

Membrane bending stiffness In this dissertation, we specifically study artificial capsules with a membrane which consists of a thin layer of a 3D isotropic material (e.g. a gelled membrane reinforced by a polymer network). The bending resistance is directly related to the ratio of the membrane thickness to the capsule radius. For thickness ratios less than 10%, it is generally admitted that

bending effects will be very small compared to the membrane forces. It is thus quite reasonable to ignore bending forces.

However, one of the drawbacks of the present study is the lack of bending resistance of the capsule membrane leading to non-physical folds in the regions where the membrane is undergoing compression. Accounting properly for bending and the post buckling behaviour of the capsule membrane is a formidable problem of shell mechanics. The reason being that the capsule is subjected to large deformation, large membrane forces and that the bending effect becomes preponderant only on parts of the wall. It is clear that a very fine mesh of the capsule wall would be necessary if we were to reproduce the folds with any precision. This would increase very significantly the computer time. The interesting question which arises at this point is how necessary is it to account for bending forces? If the capsule wall has a highly anisotropic structure (e.g. the red blood cell wall which consists of a lipid bi-layer lined by a protein network), it is clear that bending forces can be fairly large as compared to membrane shear forces and must be accounted for.

Appendix A

Numerical results: capsule deformation and velocity in a square channel

Membrane law	Ca	a/ℓ	L/ℓ	L_y/ℓ[1]	L_a/ℓ	$(L-L_a)/\ell$	v_o/V
NH	0.000	0.85	1.7000	1.7000	1.7000	0.0000	
NH	0.010	0.85	1.6076	1.7027	1.5045	0.1031	1.3500
NH	0.020	0.85	1.5824	1.6956	1.4600	0.1224	1.3487
NH	0.050	0.85	1.6104	1.6700	1.4255	0.1848	1.3543
NH	0.080	0.85	1.6945	1.6466	1.4512	0.2433	1.3638
NH	0.100	0.85	1.7470	1.6296	1.4592	0.2877	1.3709
NH	0.000	0.90	1.8000	1.8000	1.8000	0.0000	
NH	0.010	0.90	1.7060	1.7741	1.6585	0.0475	1.2884
NH	0.020	0.90	1.7007	1.7557	1.5707	0.1300	1.2927
NH	0.050	0.90	1.7601	1.7085	1.5657	0.1944	1.3104
NH	0.080	0.90	1.8820	1.6778	1.6046	0.2774	1.3261
NH	0.100	0.90	1.9551	1.6570	1.6204	0.3347	1.3365
NH	0.000	0.95	1.9000	1.9000	1.9000	0.0000	
NH	0.005	0.95	1.8936	1.8240	1.8832	0.0104	1.2385
NH	0.020	0.95	1.8367	1.7802	1.7122	0.1244	1.2508
NH	0.030	0.95	1.8551	1.7608	1.7090	0.1461	1.2592
NH	0.050	0.95	1.9354	1.7297	1.7353	0.2001	1.2747
NH	0.080	0.95	2.0986	1.7064	1.7791	0.3195	1.2957
NH	0.100	0.95	2.2201	1.6874	1.8243	0.3958	1.3099
NH	0.000	1.00	2.0000	2.0000	2.0000	0.0000	
NH	0.005	1.00	2.0420	1.8568	2.0420	0.0000	1.1934

[1]L_y/ℓ: the height of capsule profile

NH	0.010	1.00	1.9982	1.8138	1.9442	0.0541	1.2037
NH	0.020	1.00	1.9836	1.7935	1.8710	0.1126	1.2159
NH	0.050	1.00	2.1249	1.7352	1.9040	0.2209	1.2449
NH	0.080	1.00	2.3512	1.7136	1.9828	0.3684	1.2715
NH	0.100	1.00	2.6471	1.6729	2.1198	0.5273	1.3051
NH	0.000	1.05	2.1000	2.1000	2.1000	0.0000	
NH	0.005	1.05	2.1737	1.8814	2.1737	0.0000	1.1419
NH	0.010	1.05	2.1997	1.8525	2.1997	0.0000	1.1628
NH	0.015	1.05	2.1807	1.8241	2.1634	0.0172	1.1774
NH	0.020	1.05	2.1628	1.8040	2.0965	0.0663	1.1845
NH	0.030	1.05	2.2030	1.7870	2.0870	0.1160	1.1980
NH	0.050	1.05	2.3545	1.7604	2.1175	0.2370	1.2205
NH	0.080	1.05	2.6770	1.7146	2.2442	0.4328	1.2586
NH	0.000	1.10	2.2000	2.2000	2.2000	0.0000	
NH	0.010	1.10	2.3547	1.8574	2.3547	0.0000	1.1313
NH	0.015	1.10	2.3625	1.8381	2.3625	0.0000	1.1486
NH	0.020	1.10	2.3484	1.8220	2.3178	0.0306	1.1597
NH	0.030	1.10	2.3932	1.8005	2.2817	0.1115	1.1767
NH	0.050	1.10	2.5893	1.7750	2.3147	0.2745	1.2038
NH	0.070	1.10	2.8995	1.7226	2.4537	0.4458	1.2340
NH	0.000	1.20	2.4000	2.4000	2.4000	0.0000	
NH	0.010	1.20	2.7554	1.8923	2.7554	0.0000	1.0708
NH	0.020	1.20	2.8338	1.8687	2.8338	0.0000	1.1108
NH	0.030	1.20	2.8831	1.8311	2.8274	0.0558	1.1350
NH	0.050	1.20	3.2771	1.7970	2.9097	0.3675	1.1781
SK (C=1)	0.000	0.85	1.7000	1.7000	1.7000	0.0000	
SK (C=1)	0.010	0.85	1.6049	1.7011	1.6049	0.0000	1.3506
SK (C=1)	0.030	0.85	1.5813	1.6895	1.4336	0.1477	1.3500
SK (C=1)	0.050	0.85	1.5920	1.6759	1.4341	0.1579	1.3534
SK (C=1)	0.100	0.85	1.6604	1.6497	1.4609	0.1995	1.3646
SK (C=1)	0.200	0.85	1.7795	1.6180	1.4989	0.2807	1.3807
SK (C=1)	0.300	0.85	1.8739	1.6006	1.5195	0.3543	1.3895
SK (C=1)	0.500	0.85	2.0152	1.5979	1.5487	0.4664	1.4000
SK (C=1)	0.000	0.95	1.9000	1.9000	1.9000	0.0000	
SK (C=1)	0.010	0.95	1.8807	1.8055	1.8807	0.0000	1.2444
SK (C=1)	0.020	0.95	1.8318	1.7855	1.7107	0.1210	1.2498
SK (C=1)	0.050	0.95	1.8813	1.7454	1.7308	0.1505	1.2694
SK (C=1)	0.100	0.95	1.9965	1.7153	1.7728	0.2237	1.2909
SK (C=1)	0.200	0.95	2.1709	1.6988	1.8205	0.3504	1.3136
SK (C=1)	0.300	0.95	2.2561	1.6881	1.8357	0.4203	1.3220

SK (C=1)	0.500	0.95	2.4457	1.6828	1.8679	0.5778	1.3305
SK (C=1)	0.000	1.00	2.0000	2.0000	2.0000	0.0000	
SK (C=1)	0.010	1.00	2.0457	1.8195	2.0457	0.0000	1.2044
SK (C=1)	0.020	1.00	1.9799	1.8003	1.8919	0.0880	1.2134
SK (C=1)	0.030	1.00	1.9905	1.7852	1.8819	0.1086	1.2224
SK (C=1)	0.050	1.00	2.0499	1.7622	1.9118	0.1381	1.2365
SK (C=1)	0.100	1.00	2.1861	1.7278	1.9545	0.2316	1.2608
SK (C=1)	0.200	1.00	2.3816	1.7132	2.0026	0.3790	1.2834
SK (C=1)	0.300	1.00	2.4798	1.7342	2.0158	0.4640	1.2927
SK (C=1)	0.500	1.00	2.6784	1.7195	2.0413	0.6371	1.2983
SK (C=1)	0.000	1.10	2.2000	2.2000	2.2000	0.0000	
SK (C=1)	0.010	1.10	2.3392	1.8666	2.3392	0.0000	1.1274
SK (C=1)	0.018	1.10	2.3472	1.8384	2.3472	0.0000	1.1489
SK (C=1)	0.020	1.10	2.3171	1.8301	2.3015	0.0156	1.1558
SK (C=1)	0.030	1.10	2.3422	1.8138	2.3057	0.0365	1.1674
SK (C=1)	0.040	1.10	2.3809	1.8018	2.3092	0.0717	1.1768
SK (C=1)	0.070	1.10	2.5058	1.7861	2.3181	0.1877	1.1974
SK (C=1)	0.100	1.10	2.6201	1.7712	2.3588	0.2613	1.2101
SK (C=1)	0.200	1.10	2.8209	1.7525	2.3764	0.4444	1.2282
SK (C=1)	0.300	1.10	2.9709	1.7774	2.4053	0.5656	1.2372
SK (C=1)	0.500	1.10	3.1883	1.7986	2.3969	0.7914	1.2369
SK (C=1)	0.000	1.20	2.4000	2.4000	2.4000	0.0000	
SK (C=1)	0.030	1.20	2.8276	1.8688	2.8276	0.0000	1.1127
SK (C=1)	0.050	1.20	2.8647	1.8315	2.8213	0.0433	1.1387
SK (C=1)	0.100	1.20	3.0667	1.8050	2.7986	0.2681	1.1634
SK (C=1)	0.200	1.20	3.3400	1.8144	2.7903	0.5497	1.1761
SK (C=1)	0.300	1.20	3.5133	1.8163	2.8150	0.6983	1.1843

Bibliography

[1] B. Abismaïl, J. P. Canselier, A. M. Wilhelm, H. Delmas, and C. Gourdon. Emulsification by ultrasound: drop size distribution and stability. *Ultrasonics Sonochemistry*, 6:75–83, 1999.

[2] B. Abismaïl, J. P. Canselier, A. M. Wilhelm, H. Delmas, and C. Gourdon. Emulsification processes: on-line study by multiple light scattering measurements. *Ultrasonics Sonochemistry*, 7:187–92, 2000.

[3] C. Anchisi, M. C. Meloni, and A. M. Maccioni. Chitosan beads loaded with essential oils in cosmetic formulations. *Journal of Cosmetic Science*, 57:205–214, 2006.

[4] P. Bagchi. Mesoscale simulation of blood flow in small vessels. *Biophysical Journal*, 92:1858–1877, 2007.

[5] D. Barthès-Biesel. Motion of a spherical microcapsule freely suspended in a linear shear flow. *Journal of Fluid Mechanics*, 100:831–853, 1980.

[6] D. Barthès-Biesel, A. Diaz, and E. Dhenin. Effect of constitutive laws for two-dimensional membranes on flow-induced capsule deformation. *Journal of Fluid Mechanics*, 460:211–222, 2002.

[7] D. Barthès-Biesel and J.M. Rallison. The time-dependent deformation of a capsule freely suspended in a linear shear flow. *Journal of Fluid Mechanics*, 113:251–267, 1981.

[8] D. Barthès-Biesel and H. Sgaier. Role of membrane viscosity in the orientation and deformation of a spherical capsule suspended in shear flow. *Journal of Fluid Mechanics*, 160:119–135, 1985.

[9] D. Barthès-Biesel, J. Walter, and A.-V. Salsac. *Computational Hydrodynamics of Capsules and Biological Cells, Chapter 2. Flow-Induced Deformation of Artificial Capsules*. CRC Press, 1st edition, 2010.

[10] K. Bouchemal, S. Briançon, E. Perrier, H. Fessi, I. Bonnet, and N. Zydow-
icz. Synthesis and characterization of polyurethane and poly(ether urethane)
nanocapsules using a new technique of interfacial polycondensation combined
to spontaneous emulsification. *International Journal of Pharmaceutics*, 269:89–
100, 2004.

[11] H.-J. Butt. Measuring electrostatic, Van der Waals, and hydration forces in
electrolyte solutions with an atomic force microscope. *Biophysical Journal*,
60:1438–1444, 1991.

[12] M. Carin, D. Barthès-Biesel, F. Edwards-Lévy, C. Postel, and D. C. Andrei.
Compression of biocompatible liquid-filled HSA-alginate capsules: determina-
tion of the membrane mechanical properties. *Biotechnology and Bioengineering*,
82:207–212, 2003.

[13] F. Caruso, D. Trau, H. Möhwald, and R. Renneberg. Enzyme encapsulation in
layer-by-layer engineered polymer multilayer capsules. *Langmuir*, 16:1485–1488,
2000.

[14] E. Cerda and L. Mahadevan. Geometry and physics of wrinkling. *Physical
Review Letters*, 90:1–5, 2003.

[15] K. S. Chang and W. L. Olbricht. Experimental studies of the deformation
and breakup of a synthetic capsule in steady and unsteady simple shear flow.
Journal of Fluid Mechanics, 250:609–633, 1993.

[16] T. X. Chu. *Fabrication et caractérisation de populations de microcapsules avec
une technique microfluidique*. PhD thesis, Université de Technologie de Com-
piègne, 2011.

[17] T. X. Chu, A.-V. Salsac, E. Leclerc, D. Barthès-Biesel, H. Wurtz, and
F. Edwards-Lévy. Comparison between measurements of elasticity and free
amino group content of ovalbumin microcapsule membranes: discrimination of
the cross-linking degree. *Journal of Colloid and Interface Science*, 355:81–88,
2011.

[18] P. de Vos, M. M. Faas, M. Spasojevic, and J. Sikkema. Encapsulation for
preservation of functionality and targeted delivery of bioactive food components.
International Dairy Journal, 20:292–302, 2010.

[19] A. Diaz and D. Barthès-Biesel. Entrance of a bioartificial capsule in a pore. *Computer Modeling in Engineering & Sciences*, 3:321–338, 2002.

[20] A. Diaz, N. Pelekasis, and D. Barthès-Biesel. Transient response of a capsule subjected to varying flow conditions: Effect of internal fluid viscosity and membrane elasticity. *Physics of Fluids*, 12:948–957, 2000.

[21] S. K. Doddi and P. Bagchi. Three-dimensional computational modeling of multiple deformable cells flowing in microvessels. *Physical Review E*, 79:046318, 2009.

[22] Sai K. Doddi and P. Bagchi. Lateral migration of a capsule in a plane Poiseuille flow in a channel. *International Journal of Multiphase Flow*, 34:966–986, 2008.

[23] F. Dubreuil, N. Elsner, and A. Fery. Elastic properties of polyelectrolyte capsules studied by atomic-force microscopy and RICM. *The European Physical Journal. E, Soft matter*, 12:215–221, 2003.

[24] W. A. Ducker, T. J. Senden, and R. M. Pashley. Direct measurement of colloidal forces using an atomic force microscope. *Nature*, 353:239–241, 1991.

[25] F. Edwards-Lévy, M.-C. Andry, and M.-C. Lévy. Determination of free amino group content of serum albumin microcapsules. II: Effect of variations in reaction time and in terephthaloyl chloride concentration. *International Journal of Pharmaceutics*, 103:253–257, 1993.

[26] A. W. El-Kareh and T. W. Secomb. A model for red blood cell motion in bifurcating microvessels. *International Journal of Multiphase Flow*, 26:1545–1564, 2000.

[27] E. Evans and W. Rawicz. Entropy-driven tension and bending elasticity in condensed-fluid membranes. *Physical Review Letters*, 64:2094–2097, 1990.

[28] Z. Fang and B. Bhandari. Encapsulation of polyphenols - a review. *Trends in Food Science & Technology*, 21:510–523, 2010.

[29] A. Fery, F. Dubreuil, and H. Möhwald. Mechanics of artificial microcapsules. *New Journal of Physics*, 6:1–13, 2004.

[30] A. Fery and R. Weinkamer. Mechanical properties of micro- and nanocapsules: Single-capsule measurements. *Polymer*, 48:7221–7235, 2007.

[31] R. Finken and U. Seifert. Wrinkling of microcapsules in shear flow. *Journal of Physics: Condensed Matter*, 18:L185–L191, 2006.

[32] P. Gaehtgens. Mechanisms of dynamic flow adaptation of mammalian erythrocytes. *Naturwissenschaften*, 69:294–296, 1982.

[33] P. Ghirardi, G. Catenazzo, O. Mantero, G. C. Merotti, and A. Marzo. Bioavailability of digoxin in a new soluble pharmaceutical formulation in capsules. *Journal of Pharmaceutical Sciences*, 66:267–269, 1977.

[34] A. E. Green and J. E. Adkins. *Large Elastic Deformations*. Oxford University Press, Oxford, 2nd edition, 1970.

[35] A. J. Griggs, A. Z. Zinchenko, and R. H. Davis. Low-Reynolds-number motion of a deformable drop between two parallel plane walls. *International Journal of Multiphase Flow*, 33:182–206, 2007.

[36] S. Guido and G. Tomaiuolo. Microconfined flow behavior of red blood cells in vitro. *Comptes Rendus de Physique*, 10:751–763, 2009.

[37] P. C. Hammer, O. J. Marlowe, and A. H. Stroud. Numerical integration over simplexes and cones. *Mathematics of Computation*, 10:130–137, 1956.

[38] K. L. Harrison. Fetal erythrocyte lifespan. *Journal of Paediatrics and Child Health*, 15:96–97, 1979.

[39] A. Hatefi and B. Amsden. Biodegradable injectable in situ forming drug delivery systems. *Journal of Controlled Release*, 80:9–28, 2002.

[40] V. Heinrich and W. Rawicz. Automated, high-resolution micropipet aspiration reveals new insight into the physical properties of fluid membranes. *Langmuir*, 21:1962–1971, 2005.

[41] A. Helmy and D. Barthès-Biesel. Migration of a spherical capsule freely suspended in an unbounded parabolic flow. *J. Méc. Theor. Appl.*, 1:859–880, 1982.

[42] R. M. Hochmuth. Micropipette aspiration of living cells. *Journal of Biomechanics*, 33:15–22, 2000.

[43] R. Hsu and T. W. Secomb. Motion of nonaxisymmetric red blood cells in cylindrical capillaries. *Journal of Biomechanical Engineering*, 111:147–151, 1989.

[44] X.-Q. Hu, A.-V. Salsac, and D. Barthès-Biesel. Flow of a spherical capsule in a pore with circular or square cross-section. *Journal of Fluid Mechanics*, 705:176–194, 2012.

[45] R. Hurteaux, F. Edwards-Lévy, D. Laurent-Maquin, and M.-C. Lévy. Coating alginate microspheres with a serum albumin-alginate membrane: application to the encapsulation of a peptide. *European Journal of Pharmaceutical Sciences*, 24:187–197, 2005.

[46] L.J.J.M. Janssen and K. Te Nijenhuis. Encapsulation by interfacial polycondensation. I. the capsule production and a model for wall growth. *Journal of Membrane Science*, 65:59–68, 1992.

[47] B. Kaoui, G. Biros, and C. Misbah. Why do red blood cells have asymmetric shapes even in a symmetric flow? *Physical Review Letters*, 103:1–4, 2009.

[48] B. Kaoui, J. Harting, and C. Misbah. Two-dimensional vesicle dynamics under shear flow: Effect of confinement. *Physical Review E*, 83:066319, 2011.

[49] S. R. Keller and R. Skalak. Motion of a tank-treading ellipsoidal particle in a shear flow. *Journal of Fluid Mechanics*, 120:27–47, 1982.

[50] Z. Knezevic, S. Bobic, A. Milutinovic, B. Obradovic, L. Mojovic, and B. Bugarski. Alginate-immobilized lipase by electrostatic extrusion for the purpose of palm oil hydrolysis in lecithin/isooctane system. *Process Biochemistry*, 38:313–318, 2002.

[51] W. M. Kühtreiber, R. P. Lanza, and W. L. Chick. *Cell Encapsulation Technology and Therapeutics*. Birkhäuser Basel, 1998.

[52] S. Kuriakose and P. Dimitrakopoulos. Motion of an elastic capsule in a square microfluidic channel. *Physical Review E*, 84:1–22, 2011.

[53] R. Kwok and E. Evans. Thermoelasticity of large lecithin bilayer vesicles. *Biophysical Journal*, 35:637–652, 1981.

[54] E. Lac and D. Barthès-Biesel. Deformation of a capsule in simple shear flow: Effect of membrane prestress. *Physics of Fluids*, 17:072105, 2005.

[55] E. Lac, D. Barthès-Biesel, N. A. Pelekasis, and J. Tsamopoulos. Spherical capsules in three-dimensional unbounded stokes flows: effect of the membrane constitutive law and onset of buckling. *Journal of Fluid Mechanics*, 516:303–334, 2004.

[56] H. Ladjal, J.-L. Hanus, A. Pillarisetti, C. Keefer, A. Ferreira, and J. P. Desai. Atomic force microscopy-based single-cell indentation: Experimentation and finite element simulation. *2009 IEEE/RSJ International Conference on Intelligent Robots and Systems*, pages 1326–1332, 2009.

[57] O. A. Ladyzhenskaya. *The mathematical theory of viscous incompressible flow.* Second English edition, revised and enlarged. Translated from the Russian by Richard A. Silverman and John Chu. Mathematics and its Applications, Vol. 2. Gordon and Breach Science Publishers, New York, 2nd edition, 1969.

[58] Y. Lefebvre and D. Barthès-Biesel. Motion of a capsule in a cylindrical tube: effect of membrane pre-stress. *Journal of Fluid Mechanics*, 589:157–181, 2007.

[59] Y. Lefebvre, E. Leclerc, D. Barthès-Biesel, J. Walter, and F. Edwards-Lévy. Flow of artificial microcapsules in microfluidic channels: A method for determining the elastic properties of the membrane. *Physics of Fluids*, 20:123102, 2008.

[60] D. Lensen, D. M. Vriezema, and J. C. M. van Hest. Polymeric microcapsules for synthetic applications. *Macromolecular Bioscience*, 8:991–1005, 2008.

[61] A. Leyrat-Maurin and D. Barthès-Biesel. Motion of a deformable capsule through a hyperbolic constriction. *Journal of Fluid Mechanics*, 279:135–163, 1994.

[62] X. Z. Li, D. Barthès-Biesel, and A. Helmy. Large deformations and burst of a capsule freely suspended in an elongational flow. *Journal of Fluid Mechanics*, 187:179–196, 1988.

[63] H. Luo and C. Pozrikidis. Buckling of a pre-compressed or pre-stretched membrane in shear flow. *International Journal of Solids and Structures*, 44:8074–8085, 2007.

[64] R. R. Maccarini, A. Saetta, and R. Vitaliani. A non-linear finite element formulation for shells of arbitrary geometry. *Computer Methods in Applied Mechanics and Engineeing*, 190:4967–4986, 2001.

[65] J. Milanovic, V. Manojlovic, S. Levic, N. Rajic, V. Nedovic, and B. Bugarski. Microencapsulation of flavors in carnauba wax. *Sensors (Basel, Switzerland)*, 10:901–912, 2010.

[66] K. Miyazawa and I. Yajima. Preparation of a new soft capsule for cosmetics. *Journal of Cosmetic Science*, 252:239–252, 2000.

[67] S. Nakai, M. Akiyoshi, and M. Okubo. Preparation of micrometer-sized, multifunctional capsule particles for cosmetic by microsuspension polymerization utilizing the self-assembling of phase separated polymer method. *Journal of Applied Polymer Science*, 127:2407–2413, 2013.

[68] V. Nedovic, A. Kalusevic, V. Manojlovic, S. Levic, and B. Bugarski. An overview of encapsulation technologies for food applications. *Procedia Food Science*, 1:1806–1815, 2011.

[69] H. Noguchi and G. Gompper. Shape transitions of fluid vesicles and red blood cells in capillary flows. *Proceedings of the National Academy of Sciences of the United States of America*, 102:14159–14164, 2005.

[70] A. K. Pannier and L. D. Shea. Controlled release systems for DNA delivery. *Molecular Therapy : the Journal of the American Society of Gene Therapy*, 10:19–26, 2004.

[71] N. Pariot, F. Edwards-Lévy, M.-C. Andry, and M.-C. Lévy. Cross-linked beta-cyclodextrin microcapsules. II. retarding effect on drug release through semipermeable membranes. *International Journal of Pharmaceutics*, 232:175–81, 2002.

[72] G. Pieper, H. Rehage, and D. Barthès-Biesel. Deformation of a capsule in a spinning drop apparatus. *Journal of Colloid and Interface Science*, 202:293–300, 1998.

[73] D. Poncelet and R. J. Neufeld. Fundamentals of dispersion in encapsulation technology. *Progress in Biotechnology*, 11:47–54, 1996.

[74] C. Pozrikidis. The axisymmetric deformation of a red blood cell in uniaxial straining stokes flow. *Journal of Fluid Mechanics*, 216:231–254, 1990.

[75] C. Pozrikidis. *Boundary Integral and Singularity Methods for Linearized Viscous Flow.* Cambridge University Press, Cambridge, 1992.

[76] C. Pozrikidis. *Introduction to theoretical and computational fluid dynamics.* Oxford University Press, 1997.

[77] C. Pozrikidis. Numerical simulation of cell motion in tube flow. *Annals of Biomedical Engineering*, 33:165–178, 2005.

[78] C. Pozrikidis. Passage of a liquid drop through a bifurcation. *Engineering Analysis with Boundary Elements*, 36:93–103, 2012.

[79] H. M. Princen, I. Y. Z. Zia, and S. G. Mason. Measurement of interfacial tension from the shape of a rotating drop. *Journal of Colloid and Interface Science*, 23:99–107, 1967.

[80] C. Quéguiner and D. Barthès-Biesel. Axisymmetric motion of capsules through cylindrical channels. *Journal of Fluid Mechanics*, 348:349–376, 1997.

[81] M. Rachik, D. Barthès-Biesel, M. Carin, and F. Edwards-Lévy. Identification of the elastic properties of an artificial capsule membrane with the compression test: effect of thickness. *Journal of Colloid and Interface Science*, 301:217–26, 2006.

[82] M. Radmacher. Measuring the elastic properties of biological samples with the AFM. *Engineering in Medicine and Biology Magazine, IEEE*, 16:47–57, 1997.

[83] S. Ramanujan and C. Pozrikidis. Deformation of liquid capsules enclosed by elastic membranes in simple shear flow: large deformations and the effect of fluid viscosities. *Journal of Fluid Mechanics*, 361:117–143, 1998.

[84] F. Risso and M. Carin. Compression of a capsule: Mechanical laws of membranes with negligible bending stiffness. *Physical Review E*, 69:1–7, 2004.

[85] F. Risso, F. Collé-Paillot, and M. Zagzoule. Experimental investigation of a bioartificial capsule flowing in a narrow tube. *Journal of Fluid Mechanics*, 547:149–173, 2006.

[86] A.M. Rosenthal and T.M.S. Chang. The incorporation of lipid and Na$^+$-K$^+$-ATPase into the membranes of semipermeable microcapsules. *Journal of Membrane Science*, 6:329–338, 1980.

[87] D. Rugar and P. Hansma. Atomic force microscopy. *Physics Today*, 43:23–30, 1990.

[88] O. Schenk and K. Gärtner. Solving unsymmetric sparse systems of linear equations with PARDISO. *Future Generation Computer Systems*, 20:475–487, 2004.

[89] O. Schenk and K. Gärtner. On fast factorization pivoting methods for sparse symmetric indefinite systems. *Electronic Transactions on Numerical Analysis*, 23:158–179, 2006.

[90] T. W. Secomb and R. Skalak. A two-dimensional model for capillary flow of an asymmetric cell. *Microvascular Research*, 24:194–203, 1982.

[91] T. W. Secomb, R. Skalak, N. Özkaya, and J. F. Gross. Flow of axisymmetric red blood cells in narrow capillaries. *Journal of Fluid Mechanics*, 163:405–423, 1986.

[92] T. W. Secomb, B. Styp-Rekowska, and A. R. Pries. Two-dimensional simulation of red blood cell deformation and lateral migration in microvessels. *Annals of Biomedical Engineering*, 35:755–765, 2007.

[93] D. Shalaka. Vitamin E loaded pectin alginate microspheres for cosmetic application. *Journal of Pharmacy Research*, 2:1098–1102, 2009.

[94] J. D. Sherwood, F. Risso, F. Collé-Paillot, F. Edwards-Lévy, and M.-C. Lévy. Rates of transport through a capsule membrane to attain Donnan equilibrium. *Journal of Colloid and Interface Science*, 263:202–212, 2003.

[95] T. Y. Sheu and R. T. Marshall. Microentrapment of lactobacilli in calcium alginate gels. *Journal of Food Science*, 58:557–561, 1993.

[96] R. Skalak and P.-I. Branemark. Deformation of red blood cells in capillaries. *Science*, 164:717–719, 1969.

[97] R. Skalak, A. Tozeren, R. P. Zarda, and S. Chien. Strain energy function of red blood cell membranes. *Biophysical Journal*, 13:245–264, 1973.

[98] A. E. Smith, Z. Zhang, C. R. Thomas, K. E. Moxham, and A. P. Middelberg. The mechanical properties of saccharomyces cerevisiae. *Proceedings of the National Academy of Sciences of the United States of America*, 97:9871–9874, 2000.

[99] M. Sugihara-Seki, T. W. Secomb, and R. Skalak. Two-dimensional analysis of two-file flow of red cells along capillaries. *Microvascular Research*, 40:379–393, 1990.

[100] K. Sultana, G. Godward, N. Reynolds, R. Arumugaswamy, P. Peiris, and K. Kailasapathy. Encapsulation of probiotic bacteria with alginate-starch and evaluation of survival in simulated gastrointestinal conditions and in yoghurt. *International Journal of Food Microbiology*, 62:47–55, 2000.

[101] S. Svetina, D. Kuzman, R. E. Waugh, P. Ziherl, and B. Žekš. The cooperative role of membrane skeleton and bilayer in the mechanical behaviour of red blood cells. *Bioelectrochemistry*, 62:107–113, 2004.

[102] F. Theron. *Conception et mise en œuvre d'un procédé intensifié continu de microencapsulation par polycondensation interfaciale.* PhD thesis, l'Institut National Polytechnique de Toulouse, 2009.

[103] G. Tomaiuolo and S. Guido. Start-up shape dynamics of red blood cells in microcapillary flow. *Microvascular Research*, 82:35–41, 2011.

[104] G. Tomaiuolo, M. Simeone, V. Martinelli, B. Rotoli, and S. Guido. Red blood cell deformation in microconfined flow. *Soft Matter*, 5:3736, 2009.

[105] P. M. Vlahovska, T. Podgorski, and C. Misbah. Vesicles and red blood cells in flow: From individual dynamics to rheology. *Comptes Rendus de Physique*, 10:775–789, 2009.

[106] A. Walter, H. Rehage, and H. Leonhard. Shear induced deformation of microcapsules: shape oscillations and membrane folding. *Colloids and Surfaces A: Physicochemical and Engineering Aspects*, 183-185:123–132, 2001.

[107] J. Walter. *Couplage intégrales de frontières - éléments finis : application aux capsules sphériques et ellipsoïdales en écoulement.* PhD thesis, Université de Technologie de Compiègne, 2009.

[108] J. Walter, A.-V. Salsac, D. Barthès-Biesel, and P. Le Tallec. Coupling of finite element and boundary integral methods for a capsule in a stokes flow. *International Journal for Numerical Methods in Engineering*, 83:829–850, 2010.

[109] B. Wang, Y. Zhang, Z. Mao, and C. Gao. Cellular uptake of covalent poly(allylamine hydrochloride) microcapsules and its influences on cell functions. *Macromolecular Bioscience*, 12:1534–1545, 2012.

[110] H. N. Yow and A. F. Routh. Formation of liquid core-polymer shell microcapsules. *Soft Matter*, 2:940–949, 2006.

[111] C. Y. Zhao and G. H. Zhang. Review on microencapsulated phase change materials (MEPCMs): Fabrication, characterization and applications. *Renewable and Sustainable Energy Reviews*, 15:3813–3832, 2011.